SUPERLENS IMAGING AND LIGHT CONCENTRATION IN MESOSCALE PHOTONICS: DESIGN AND IMPLEMENTATION

by

Boya Jin

A dissertation submitted to the faculty of
The University of North Carolina at Charlotte
in partial fulfillment of the requirements
for the degree of Doctor of Philosophy in
Optical Science and Engineering

Charlotte

2022

Approved by:

_____
Dr. Vasily N. Astratov

_____
Dr. Glenn D. Boreman

_____
Dr. Michael A. Fiddy

_____
Dr. Mikhail V. Klibanov

ABSTRACT

BOYA JIN.: Superlens imaging and light concentration in mesoscale photonics: design and implementation. (Under the direction of DR. VASILY N. ASTRATOV)

Progress in nanofabrication made possible development of metamaterials and nanoplamonics two decades ago. The area of mesoscale photonics where the characteristic dimensions of spherical, pyramidal or other building blocks are on the order of several wavelengths remained relatively less studied. However, the optical properties of such structures are extremely interesting due to their ability to create tightly focused beams, so-called “photonic nanojets”, and to resonantly trap light inside their building blocks. In this dissertation, we focus on two main applications of such structures. It is proposed to use dielectric microcones for concentrating light on photodetector focal plane arrays (FPAs) and it is proposed to use contact high-index dielectric microspheres (also termed ball lenses) for improving resolution in cellphone-based microscopy.

We proposed and developed three designs of silicon (Si) microconical arrays which can be used as light concentrators for integration with FPAs operating in mid-infrared (MWIR) region. Such structures can be fabricated by anisotropic wet etching of Si. The spectral and angular dependencies of power enhancement factors (PEFs) provided by such high-index (n~3.5) Si microcones are calculated using finite-difference time-domain modeling. In addition, we observed and studied resonant trapping of photons inside such microcones which can lead to their applications in multispectral imaging devices with a large angle-of-view (AoV).

It is shown that similar microconical light concentrators can be formed by low-index materials (n = 1.6) which can be fabricated by Nanoscirbe or by plastic injection

molding. It is demonstrated that PEFs ~100 times can be achieved in such structures with optimized geometry. It was demonstrated a good agreement of our numerical modeling results with the experiments performed previously on structures with a suboptimal geometry.

We proposed a novel label-free cellphone microscopy assisted by high index contact ball lenses. Resolution of the cellphones is limited by the pixilation of the images. Previous microoptics-based imaging solutions provided insufficient magnification and suffered from spherical aberrations and pincushion distortion. In our work, it is shown that use of ball lenses with n~2 specially designed to provide maximal magnification values (up to ×50 times) allows to reduce the role of pixilation and reach diffraction limited resolution values of ~600 nm based on rigorous resolution quantification criteria. It is demonstrated that dispersion properties of the ball lens material significantly influence the magnification in such cellphone imaging. It is shown a semi-quantitative agreement of observed magnification with a simplified geometrical optics model. We demonstrated imaging of various biomedical samples by using proposed cellphone microscopy. It is shown that it can be used as a compact and inexpensive replacement of conventional microscopes to diagnose diseases such as melanoma *in vivo* without invasive biopsy.

To extend FoV, we assembled centimeter-scale arrays of ball lenses using either micromanipulation or air suction through microhole arrays obtained by laser burning or micromachining. It was found this technology allows obtaining ordered arrays for sufficiently large (>300 μm) ball lenses but assembling smaller microspheres can in principle be also achieved in future work. It was demonstrated that such microspherical arrays can be used as: a) superresolution coverslips with wide FoV (after embedding in

plastic), and b) retroreflectors with ultranarrow reflection cone and highly dispersive properties.

DEDICATION

I dedicate this dissertation to my...

...parents for their unconditional love, guidance, and support.

...boyfriend for his understanding, encouragement, and patient.

ACKNOWLEDGMENTS

Foremost, I wish my deepest gratitude to my advisor, Dr. Vasily N. Astratov. Over the course of the past 4 years, he has patiently and continuously guided me into the world of science and research with his extensive knowledge and the serious attitude of study. During this time period, he not only advised me on my doctoral dissertation, having insightful discussion on every single question I brought up, providing inspiring suggestions to my research directions, but also help me improved and grow as a researcher by preparing all of my scientific reports and presentations attentively, passing all the experience and wisdom of his own in all aspects of being a researcher. He even shows great concern of my life considering my situation of studying abroad. I made up my mind on developing my future career in academic research during this precious period under his advising, and he did set a role model for me of being a scientist, a researcher, and even an advisor in the future.

I would love to thank my committee members, Dr. Glenn D. Boreman, Dr. Michael A. Fiddy, and Dr. Mikhail V. Klibanov for accepting to serve on my committee, and I appreciate the time they investigate and the comments they made on my dissertation very much. I would love to thank Dr. Glenn D. Boreman for providing me suggestions and support regarding the choices I have to make for academic path. I am grateful to Dr. Angela Allen and Dr. Donald Jacobs for their invaluable advice and support through my master and doctoral years.

My research benefited from multiple collaborations of the Mesophotonics Laboratory. I am very thankful for Dr. Nicholaos I. Limberopoulos, Dr. Igor Anisimov, Dr. Augustine M. Urbas, Dr. Joshua M. Duran, and Dr. Gamini Ariyawansa from Air Force

Research Laboratory, Dr. Sarath D. Gunapala from NASA Jet Propulsion Laboratory, and Dr. Kennth W. Allen from Georgia Tech Research Institute for their continuous support and precious suggestions for multiple projects during my doctoral reseacrh.

I am very grateful to Dr. Alexey V. Maslov from University of Nizhny Novgorod for his insightful theory and simulations which support and give depth to my experimental work.

I am very thankful for Dr. Lou Deguzman for patiently help me with all the fabrication work in the clean room. Without his diligent teaching, guiding and discussing the problems in developing the fabrication, the experimental work presented in the dissertation would not have been accomplished.

During my graduate studies I enjoyed so much working with the members of Mesophotonics Laboratory. My doctoral studies could not be successful without the corporation, support, suggestion and productive discussions from Dr. Aaron Brettin, Dr. Farzaneh Abolmaali, Grant W. Bidney, and Amstrong Jean.

I was supported by the GASP award throughout my graduate studies. I am thankful for the Department of Physics and Optical Sciences for supporting me with teaching assistantships. My graduate research assistantships in Dr. Vasily Astratov's Mesophotonics Laboratory were supported through his grants from the National Science Foundation, Air Force Research Laboratory, Jet Propulsion Laboratory, North Carolina Biomedical Center, and Georgia Tech Research Institute.

Lastly, my deepest gratitude to my family for the love, support, understanding and patience which make the dissertation possible.

TABLE OF CONTENTS

LIST OF FIGURES xii

LIST OF TABLES xxi

LIST OF ABBREVIATIONS xxii

CHAPTER 1: INTRODUCTION 1

1.1: Outline and Overview of the Dissertation 1

1.1.1: Studies of photonics in mesoscale structures 7

1.1.2: Extremely tightly focusing light into photonics nanojets 8

1.1.3: Super-resolution imaging in microsphere-assisted microscopy 11

1.1.4: Building up WGM by total internal reflection 14

1.2: Microconical Si light concentrators for integration with FPAs 18

1.2.1: Introduction of focal plane arrays (FPAs) 18

1.2.2: Illumination and temperature regimes 25

1.2.3: Anisotropic wet etching of Si 29

1.3: Microconical low-index (n ~ 1.6) light concentrators 30

1.4: Super-resolution Microscopy 32

1.4.1: Definition and diffraction limitation of light 32

1.4.2: Development of techniques of super-resolution microscopy 35

1.4.3: Methodology of resolution quantification 41

1.5: Assembling monolayer of microspheres 44

1.5.1: Techniques of assembling monolayer of microspheres 44

1.5.2: Retroreflectors 47

1.6: Summary 49

CHAPTER 2: MICROCONICAL SILICON MWIR CONCENTRATORS ASSOCIATED WITH FPAS 54

2.1: Introduction of light concentrators integrated with FPAs 54

2.2: Three numerical designs of microcones integrated with FPAs 61

2.2.1: Inverted microcones heterogeneously integrated with front-illuminated FPAs 64

2.2.2: Inverted microcones monolithically integrated with PtSi Schottky Barrier diodes 68

2.2.3: Regular microcones monolithically integrated with the near-surface detectors 73

2.3: Conclusions 76

CHAPTER 3: MICROCONICAL LOW INDEX PHOTORESIST MWIR CONCENTRATORS ASSOCIATED WITH FPAS 79

3.1: Introduction of designs of MWIR light concentrators 79

3.2: Numerical designs of low-index (n = 1.6) microcones 84

3.3: Conclusions 96

CHAPTER 4: LABEL-FREE CELLPHONE MICROSCOPY ASSISTED BY HIGH-INDEX CONTACT BALL LENS WITH DIFFRACTION-LIMITED RESOLUTION 99

4.1: Introduction of cellphone microscopy 99

4.2: Fabrication of metallic double-stripe array as objects 104

4.3: Magnification quantification of LASFN35 ball lens 108

4.4: Resolution quantification of cellphone microscopy 114

4.5: Application of diagnostics of melanoma *in vivo* without biopsy 123

4.6: Conclusions 129

CHAPTER 5: MANUFACTURING AND APPLICATIONS OF ARRAYS OF MICROSPHERES 133

5.1: Introduction 133

5.2: Assembling monolayer of microspheres by air suction 137

5.3: Imaging through monolayer of microspheres to enlarge the FoV 148

5.4: High-index microsphere arrays as retroreflectors 152

5.5: Conclusions 156

CHAPTER 6: CONCLUSIONS AND FUTURE DIRECTIONS 160

REFERENCES 167

APPENDIX A: PUBLICATIONS SO FAR 190

LIST OF FIGURES

FIGURE 1.1: Evolution of a photonic nanojet as the variation of the diameter *d* of a plane-wave-illuminated circular dielectric cylinder and the refractive index of the cylinder n_1 and surrounding material n_2 at illuminating wavelength λ. (a) $d = 5$ μm, $n_1 = 3.5$, $n_2 = 1.0$, $\lambda =$ 500nm (b) $d = 5$ μm, $n_1 = 1.7$, $n_2 = 1.0$, $\lambda = 500$nm (c) $d = 5$ μm, $n_1 = 3.5$, $n_2 = 2.0$, $\lambda =$ 250nm (d) $d = 6$ μm, $n_1 = 2.3275$, $n_2 = 1.33$, $\lambda = 300$nm. [11].....8

FIGURE 1.2: Theoretical model: (a) EM amplitude map calculated at λ=530.0 nm using incident plane waves. (b) Geometrical optics model of periodically coupled lenses with the focus distance $F=D/2$. [25] 10

FIGURE 1.3: (a) Schematic of microsphere-assisted microscopy. (b) Schematic of imaging of fluorescent objects imaged by the microsphere. [40] 13

FIGURE 1.4: (a) Acoustic whispering gallery (b) Optical whispering gallery mode built up inside a microspherical cavity in mesoscale due to TIR (c) EM field map of whispering gallery mode inside microcavity. 15

FIGURE 1.5: WGM by coupling microcavity with tapered waveguide. [78] 15

FIGURE 1.6: (a) Sketch illustrating the process of fiber etching in the meniscus above the vessel with hydrofluoric acid. (b) Positioning of a 16 μm sphere on the fiber with a piece of a sharpened optical fiber. (c) A photograph of the microfluidic cell with a tapered fiber and micropump tubing. [105] 16

FIGURE 1.7: Fiber transmission spectra, measured in air (a) and in water (b) with the spheres attached at the thinnest place on the fiber (d~1.2 μm), as labeled on the graph. For clarity, the spectra are shifted vertically with respect to each other. The index and diameter of spheres is indicated. [105] 17

FIGURE 1.8: Schematic representation of an imaging system showing important sub-systems. [144] 19

FIGURE 1.9: Schematic of the HDVIP® HgCdTe APD, left: side view; right; top view (Conceptual drawing only, the layer thickness and the via size not to scale). [146] 20

FIGURE 1.10: (a) Schematic of the heterojunction phototransistors design and structure. (b) Schematic energy-band diagram of the SWIR heterojunction phototransistors. [152] 21

FIGURE 1.11: (a) Conduction band profile of $Al_{0.35}Ga_{0.65}N$/GaN (20nm/2nm) multiple-QWs and the triangular barrier (orange dashed line). (b) Conduction band profile of $Al_{0.5}Ga_{0.5}N$/GaN/$Al_{0.25}Ga_{0.75}N$ (1.8nm/1.8nm/16nm) step-QWs designed for B-to-QC ISBT and the spacer barrier (orange dashed line). (c) Schematic image of the designed sample structure. [157] 22

FIGURE 1.12: Schematic cross-section of n-i-n quantum dot infrared photodetectors (QDIP). [155] 23

FIGURE 1.13: Monolithic Si focal plane arrays of CCD. [143] 24

FIGURE 1.14: Band diagrams of metal and semiconductors when they are not in contact (up) and when they are in intimate contact. 24

FIGURE 1.15: Typical construction and operation of PtSi Schottky-barrier IR FPA designed with interline transfer CCD readout architecture. (a) and (b) show the potential diagrams in the integration and readout operations, respectively. [168] 25

FIGURE 1.16: Schematic of back-side and front-side illuminations. 26

FIGURE 1.17: The operating temperature and wavelength regions spanned by a variety of available IR detector technologies. [143] 27

FIGURE 1.18: The schematic of collection of radiation over a large area by photodetector array with large pixel size (left), and by light concentrator array which concentrate and focus light into small areas of photodetectors (right). 28

FIGURE 1.19: Schematic representation of the etched profile using (1,0,0) silicon wafers. [176] 29

FIGURE 1.20: (a) Absorption spectrum of a thin homogeneous film of made of the developed photoresin IP-Dip. The thickness of the layer is 10 μm. [209] (b): FTIR spectra of PET (a) Virgin and implanted at 50 keV to (b) $1x10^{15}$, (c) $1x10^{16}$ and (d) $5x10^{16}$ B^{+} cm^{-2}. [179] 30

FIGURE 1.21: (a) Naoscribe nanoscale 3-D printing machine (b) Capability of fabricating accuracy. 31

FIGURE 1.22: (a) Schematic of injection molding process of plastic (b) Capability of fabricating accuracy, the “posts” on the top have a dimension of 3μm ×3μm. 32

FIGURE 1.23: Illustration of numerical aperture (NA) of an imaging system of lens. 34

FIGURE 1.24: Illustration of spatial resolution defined by overlapping of diffracted patten as Airy disks of two-point sources. 34

FIGURE 1.25: Schematic representation of a surface wave (surface plasmon polariton) propagating along a metal-dielectric interface. 36

FIGURE 1.26: Schematic of near-field scanning optical microscope (NSOM). The probe has a diameter of the aperture and the distance to the specimen much less than the illuminating wavelength. 36

FIGURE 1.27: Schematics of the PSIM system. [198] 38

FIGURE 1.28: (a) Optical microscope image of plano-spherical lenses on a CHQ nanotube crystal, showing the magnification by the lens. (b) The sub-diffraction-limit patterns cannot be resolved in conventional optical microscopy, but the magnifying effect through the lens allows the stripe patterns of 250/220 nm spacing to be resolved. [37] 38

FIGURE 1.29: (a) Schematic of the transmission mode microsphere superlens integrated with a classical optical microscope. (b) Objects of stripes with 360 nm width and 130 nm spacing are clearly resolved, and a gold-coated circular array with 50 nm in diameter and 50 nm gap are clearly resolved. [38] 39

FIGURE 1.30: (a) Schematic of the setup; (b) Virtual image formation by a liquid-immersed sphere; (c) SEM image of an array of gold dimers formed by 120 nm nanoparticles with 150 nm separations; (d) BTG sphere with n=1.9 immersed in IPA; (e) Virtual imaging of the array shown in (c) through the microsphere at a different depth compared to (d) by 100× (NA = 0.9) objective; (f) SEM image of a Blu-ray disk with 200 nm width stripes separated by 100 nm width grooves; (g) BTG microspheres with diameters in the range 5–20 μm fully immersed in IPA; and (h) Virtual imaging of the Blu-ray disk through the microspheres at a different depth compared to (g) by 20× (NA = 0.4) objective. [39] 40

FIGURE 1.31: (a) Schematic of h-SIL and s-SIL. (b) Middle inset is the SEM image of the 4-cylinder structure with 50-60 nm gaps between 100 nm cylinders. (c) SEM image of a Blu-ray Disk and schematic of the SIL setup. [42] 41

FIGURE 1.32: Micrographs of the 25 nm AAO template by (a) SEM, (b) standard SLCM, (c) 5 μm diameter FS mSLCM, (d) 2.5 μm diameter FS mSLCM, (e) 7.5 μm diameter FS mSLCM, and (f) 5 μm diameter PS mSLCM, where the insets are the corresponding pseudo color images. [204] 43

FIGURE 1.33: (a) Image of an Au dimer obtained through BTG microsphere after 10 minutes of the IPA evaporation. (b) Comparison of the measured (red background) and calculated (dashed blue curves) irradiance profiles through the cross-sectionof the Au dimers (x-axis). (c,d) Same as (a,b), respectively, but after drying for 72 hours. [6] 44

FIGURE 1.34: (a) Vertical convective self-assembly diagram. (b) and (c) SEM images of assembled monolayer of microspheres. [209] 46

FIGURE 1.35: (a) Schematic for an imaging fiber-based optical tweezer array system. (b) Region of optical tweezer array system shown in more detail. (c) Consecutive images of trapped 4.5mm silica microspheres. [215] 47

FIGURE 1.36: Retroreflector: common shapes. a) Corner-cube retroreflector b) Spherical retroreflector (cat's eye). The sphere is from material with higher refractivity index. [216] 48

FIGURE 1.37: Comparison of beam reflection by (a) a conventional mirror and (b) a nonlinear phase conjugate mirror. [220] 49

FIGURE 2.1: (a) Conventional FPAs with large individual photodetector mesa size and compact arrangement. (b) and (c) Illustration of reducing the individual photodetector mesa size and leave blank spaces for electrical circularity connections. 55

FIGURE 2.2: (a) Schematic of metalens as light concentratos optically coupled with FPAs with small photodetector mesa size. (b) Power distribution map of the focused beam after passing through metalens. [242] 56

FIGURE 2.3: (a) Microsphere with high index of n = 1.8 optically coupled with photodetector mesa with 10 μm size. (b) Simulation showing an AoV larger than 20° that still half of the power for normal incidence can be collected by the detector. [223] 57

FIGURE 2.4: (a) Top-view (1,0,0) silicon substrate patterned with square shape photoresist array (blue squares). Microcones are fabricated by anisotropic wet etching of silicon along (1,1,1) planes (white dashed lines) around each photoresist square. (b) Side-view microcones with (1,1,1) oriented sidewalls, the angle formed by the sidewalls with the surface of the wafer is 54.7°. (c) (d) (e) Top and side SEM pictures of silicon microcone array fabricated by anisotropic wet etching performed by Grant Bidney. [253-255] 62

FIGURE 2.5: Fabrication procedure of silicon microcone using anisotropic wet etching we developed in the cleanroom of UNC Charlotte. 63

FIGURE 2.6: (a) Inverted Si microcone array heterogeneously integrated with the front-illuminated FPA exemplified by strained-layer type II superlattice. (b) Simplified theoretical model of individual inverted microcone heterogeneously aligned with one photodetector mesa. [221] 64

FIGURE 2.7: (a) EM field distribution calculated at normal incidence for inverted Si microcone with the circular cross-section and with the large base D_l = 14 μm, small base D_s = 4 μm, and height h=7.07 μm. (b) The PEF spectra calculated using a square monitor with the 4 μm side placed 100 nm below the surface of Si substrate (shown as a "Detector" in (a)). [221] 65

FIGURE 2.8: (a) Inverted Si microcones monolithically integrated with the metal-Si Schottky photodetectors and (b) Corresponding theoretical model. 68

FIGURE 2.9: (a) EM field distribution calculated at normal incidence on the microcone with a 1 μm thick Pt mirror at the bottom base. Slight absorption effects in the depleted

layer of Schottky barrier were modeled by introducing 1% absorption at the 1 μm propagation length in the lowest 1 μm thick section of microcone. (b) Direct comparison of the PEF spectra calculated with (red) and without (blue) Pt mirror using a 4 μm monitor placed 0.1 μm above the bottom base. [221] 70

FIGURE 2.10: The PEF spectra calculated for broad range of angles of incidence in two polarizations (TE and TM) of incident plane waves for a Si microcone containing a metallic mirror at its bottom base. [221] 72

FIGURE 2.11: (a) Regular Si microcones monolithically integrated with the near-surface detectors. (b) Corresponding theoretical model. [221] 73

FIGURE 2.12: (a-d) Photonic nanojets produced by the regular (not inverted) microcones with the bottom base 11 μm and different sizes of the top base: 4.9, 4.7, 4.4, and 4.1 μm, respectively. [221] 74

FIGURE 2.13: Photonic nanojets for microcones with D_l =15 μm calculated for plane waves incident (a) at normal incidence and (b) at 40°. (c) Power enhancement factors calculated for 1.0 and 1.5 μm detectors as a function of angle of incidence for microcones with the same D_l =15 μm and a range of parameters D_s indicated in the legend. [221] 75

FIGURE 3.1: (a-d) Fabrication procedure of inverted microcone array in photoresist by Nanoscribe. (e-h) Fabrication procedure of inverted microcone array in plastic by injection molding. 83

FIGURE 3.2: The schematic of inverted microcone structure integrated with photodetector mesa of FPAs and the definition of power enhancement factor.[222] 86

FIGURE 3.3: (a) Paraxial ray tracing propagating through the microcone. (b) Off-axis ray tracing propagating through the microcone. [222] 87

FIGURE 3.4: (a) $PEF_{3\text{-}D}$ spectra calculated for 3-D model at $\alpha = 0°$. (b) Spectra of $(PEF_{2\text{-}D})^2$ values calculated for corresponding 2-D model. (c) $PEF_{2\text{-}D}$ spectra calculated in a broad range of parameters D_b, θ, and h for 2-D model illustrating that in each case the spectral variations are relatively small in a broad spectral range. Insert illustrates the definition of $PEF_{2\text{-}D}$. [222] 88

FIGURE 3.5: (a-c) EM field distributions calculated at normal incidence on the top base of the microcones with index $n = 1.6$, sidewall angle $\theta = 10°$, and height $h = 100$ μm placed on top of a high-index ($n = 3.43$) substrate at a wavelength $\lambda = 4$ μm for different sizes of the microcone's bottom base, $D_b = 2, 4, 8$ μm, respectively. (d-f) $PEF_{2\text{-}D}$ spectra calculated as a function of the microcone height, $0 \leq h \leq 150$ μm, for a range of microcone angles, $0° \leq \theta \leq 30°$, with $D_b = 2, 4, 8$ μm, respectively. [222] 89

FIGURE 3.6: (a-c) EM field distributions calculated for microcone with D_b = 8 μm and h = 50 μm at different angles of incidence, $\alpha = 0°$, 10°, and 20°, respectively. (d-f) $PEF_{2\text{-}D}$

values calculated as a function of α in two polarizations (TE and TM) of incident light for microcones with different heights and $\theta = 10°$ and with $D_b = 2$, 4, and 8 μm, respectively. [222] 92

FIGURE 3.7: Microscope images showing results of the (a) high-speed and (b) Low-speed nanoscribe fabrication of the microconical arrays. (c) Photocurrent spectra from 10×10 arrays in the following cases: (i) full fill-factor detectors with 58 μm aperture without the microcones (black), (ii) detectors with 22 μm aperture without the microcones (blue), and (iii) detectors with 22 μm aperture with microcones (red). (d) $PEF_{2\text{-}D}$ values calculated at TE polarization show relatively small variations for each angle of incidence (α) in a broad spectral range $1 \leq \lambda \leq 5$ μm. Similar results were obtained at TM polarization. [222] 95

FIGURE 4.1: Photograph and schematic diagram of the worm imager. Nematodes in a 500 μm high microchamber are illuminated with an LED and cast a shadow onto a CMOS video camera chip attached at the bottom of the chamber. [266] 100

FIGURE 4.2: Experimental arrangement for biological applications of DIHM. [268] 101

FIGURE 4.3: (a) Mobile phone microscopy optical layout for fluorescence imaging. (b) A current prototype, with filters and LED installed, capable of fluorescence imaging. [270] 102

FIGURE 4.4: (a) Schematic illustration of cellphone-based fluorescence microscope. (b) Ray-tracing diagram of the cellphone microscope where excitation and scattered beams are indicated with solid blue rays, while the fluorescent emission is highlighted with solid green rays. [238] 103

FIGURE 4.5: Schematic of Au double-stripe array deposited on transparent sapphire substrate. Each unit contains two stripes with 1.0μm width and a gap with variable sizes between 0.4μm to 0.7μm between them. 105

FIGURE 4.6: Fabrication procedure of Au double-stripe array deposited on sapphire substrate by electron beam lithography. 106

FIGURE 4.7: SEM images of Au double-stripe arrays with different dimensions by using E-beam lithography. The actual width of the stripes is approximately 1.1μm, while the fabricated gaps have averaged values of 469nm, 537nm, 644nm, and 707nm. 107

FIGURE 4.8: SEM image of Siemen's Star. 107

FIGURE 4.9: Schemtaic of label-free cellphone microscopy assisted by contact ball lens with high refractive index $n = 2.049$ at $\lambda = 480$nm. 109

FIGURE 4.10: Imaging modalities of virtual imaging and real imaging through ball lens in cellphone microscopy. [36] 110

FIGURE 4.11: Magnification (*M*) varying with refractive index contrast *n'* for contact ball lens when $g = 0$. Insert: dispersion curve of LASFN35 glass in visible spectral range. ...111

FIGURE 4.12: (a) The SEM images of the objects of Siemen's Star and metallic double stripes, and the images through the imaging system of cellphone camera plus LASFN35 ball lens at five different illumination wavelength. (b) Image magnification through conatct ball lens limited by geometrical optics for different diameters of ball lens at diferent illumination wavelength. (c) Experimetal iamge magnification captured by cellphone camera thorugh contact ball lens. 114

FIGURE 4.13: (a) Formation of images through imaging system by convolution. (b) Fitting of the experimental and convolutional intensity profiles of the images of double-stripe array. 115

FIGURE 4.14: (a) and (b): Experimental and convolutional images of double-stripe unit at illuminating wavelength $\lambda = 589$nm. (c) Determining the I_{min} value for experimental image to fit the convlution result the best (d) Best fitting results of normalized intensity profiles of experimental and convolutional images indicating a resolution of 663nm of cellphone microscopy. 116

FIGURE 4.15: The resolution quantification results for different diameters of the ball lens at differetn illumination wavelength. 118

FIGURE 4.16: (a) Image of Siemen's Star by cellphone microscopy with $\lambda = 480$nm inserted, (b) Intensity profile of object passing through imaging system, (c) I_{peak} / I_{dip} ratio for different I_{min} value, (4) Fitting of experimental and convolutional results for Gaussian function with FWHM = 913nm. 119

FIGURE 4.17: (a) The FoV region (red dashed circle) of the images for different diameters of the ball lens at $\lambda = 480$nm and $\lambda = 589$nm (b) The FoV values for trhee different diameters of the ball lens at five different illumination wavelength. 121

FIGURE 4.18: Schematic of enlarging the FoV by fast-scanning over the sample by attaching microprobes to the ball lens. 123

FIGURE 4.19: Images of Melanoma sample taken by (a) 10x standard microscope objective and (b) ordinary cellphone camera, (c) and (d) taken by cellphone camera through $D = 2.0$mm LASFN35 ball lens, (e) and (f) taken by cellphone camera through $D = 1.5$mm LASFN9 ball lens, (g) and (h) taken by cellphone camera through $D = 1.25$mm LAF22 ball lens. 125

FIGURE 4.20: (a) and (b) Image magnification through ball lens changing with the refractive index contrast between ball lens and enviroment with diameter $D = 1.0$mm and $D = 2.0$mm and gap g varys from 0 to 0.25mm limited by geometrical optics, the dashed lines are indicating the positions of *n'*. 127

FIGURE 4.21: Images of four biomedical samples by 10x standard microscope objective (first column), by ordinary cellphone camera (second column), and by cellphone camer through D = 2.0mm LASFN35 ball lens placed at three different locations on the sample in transmission illuminating mode (third and forth column) and in reflection illumintating mode (fifth and sixth column). The scale bars are the same for each column. 129

FIGURE 5.1: (a) Applying suction through a micro-hole array as a force to assemble the microspheres in the holes. (b) Blowing away interstitial spheres by an additional flux of air parallel to the substrate, and (c) Perfectly ordered single monolayer of spheres sitting in microholes. [13] 136

FIGURE 5.2: Design of 2-D hexagonal arrays microholes for assembling microsphere arrays. 137

FIGURE 5.3: (a) and (b) Back-side and front-side of laser burning microhole array with D = 50μm, respectively. (c), (d) and (e) Back-side of laser burning microhole array with D = 250μm, 300μm, and 900μm, respectively. (f) Machinal drilling microhole array with D = 900μm. 139

FIGURE 5.4: (a) Images of microhole arrays with different dimensions by laser burning. (b) Image of microhole array by mechanical drilling. 140

FIGURE 5.5: (a) Assembling microspheres on top pf microhole arrays by air suction from vacuum. (b) removing additional multi-layers of microspheres by air blowing in horizontal direction. 142

FIGURE 5.6: Assembled monolayer of microspheres on microhole arrays with different dimensions, D refers to the diameter of the microspheres. 144

FIGURE 5.7: (a)-(c) Procedure of embedding the microsphere array into plastic coverslip by applying heat and pressure. (d) Illustration of perfectly ordered microsphere array embedded in coverslip with same extension height. (e) The hot plate which can provide heat and pressure. 145

FIGURE 5.8: (a) Using hot gun to adhere coverslip to microspheres to avoid losing microspheres by static electricity. (b) Microspheres with variable sizes embedded in coverslip with different depth and have same extension to be in contact with the object at same time. 146

FIGURE 5.9: Embedded microsphere arrays with different diameter and refractive index. 147

FIGURE 5.10: Images of frog blood through embedded microsphere array by different materials and diameters. The measured additional magnifications are labeled. 151

FIGURE 5.11: (a) Numerical modeling of focusing position of plane wave at λ = 532nm by spherical lens with a diameter of 20μm with a varying refracitve index. (b) The best refracitve index for spherical lenses with different diameteres to focus plane wave excatly on the back surface of the lens. 152

FIGURE 5.12: (a) and (b) Illustration of single ball lens and array of ball lenses half coated with 100nm Au layer, respectively. (c) Schematic of the setup of retroreflectors. The laser is incident on the ball lens array retroreflector with an incident angle α, the retroreflecting pattern in the same direction with the incident light is capture by a screen attached to the laser. 153

FIGURE 5.13: Retroreflecting patterns for LASFN9 and sapphire half-coated ball lens arrays for incident lasers with different wavelength at 10° incident angle. The corresponding refractive index at different wavelengths due to dispersion are labeled on the images. 154

FIGURE 5.14: (a) Illustration of the half angle of the cross-section triangle of the retroreflection cone. (b) and (c) The diameter of the concentric circles and the corresponding half angle of the cross-section area for retroreflectors by sapphire and LASFN9 ball lens arrays at different incident wavelengths. 156

LIST OF TABLES

TABLE 5.1: List of microhole arrays with different dimensions obtained from Micron Laser Technology, Potomic Photonics Inc, and Mechanical Department at UNC Charlotte. 138

TABLE 5.2: List of purchased microspheres with materials, refractive index, manufacturer, and the corresponding dimensions of microhole arrays to fabricate monolayer of them. (BTG is the abbreviation of Barium Titanate Glass) 141

LIST OF ABBREVIATIONS

1-D	one-dimensional
2-D	two-dimensional
2DPN	two-dimensional plasmonic nanoscope
3-D	three-dimensional
AFM	atomic force microscope
AFRL	air force research laboratory
AoV	angle-of-view
BOE	buffered oxide etch
BTG	barium titanate glass
CCD	charge-coupled devices
DIHM	digital in-line holographic microscopy
E-beam	electron beam
EM	electromagnetic
FDTD	finite different time domain
FFSL	far-field superlens
FFTR	far-field time reversal
FIR	far infrared
FL	fluorescent
FoV	field-of-view
FPA	focal plane array
FWHM	full width at half maximum
HI	heterogenous integration

HOT	high operating temperature
hSIL	hemispherical solid-immersion lens
IC	integrated circuits
IPA	isopropyl alcohol
IR	infrared
KOH	potassium hydroxide solution
LWIR	long-infrared
MEMS	microelectromechanical systems
MRF	minimally resolved feature sizes
MSI	microspherical superlens imaging
MWIR	mid-infrared
NA	numerical aperture
NEP	noise-equivalent power
nSIL	nano solid-immersion lens
NSOM	near-field scanning optical microscope
OFM	optofluidic microscopy
PEF	power enhancement factor
PET	polyethylene terephthalate
PMMA	polymethyl methacrylate
PSF	point-spread function
PSIM	plasmonic structured illumination microscope
Pt	platinum
Q	quality

QD	quantum dots
QDIP	quantum dots infrared photodetectors
QE	quantum efficiency
QW	quantum well
QWIP	quantum well infrared photodetectors
ROIC	readout integrated circuits
SEM	scanning electron microscope
Si	silicon
SIL	solid-immersion lens
SL	superlattice
SLCM	scanning laser confocal microscope
SNR	signal-to-noise ratio
SPP	surface plasmon polariton
SQ	Shockley-Queisser
sSIL	superspherical solid-immersion lens
SWIR	short infrared
T	transmission
T2SL	type-II superlattice
TIL	infiltrating lymphocytes
TIR	total internal reflection
TMAH	tetramethylammonium hydroxide
UV	ultraviolet
WGM	whispering gallery mode

CHAPTER 1: INTRODUCTION

1.1 Outline and Overview of the dissertation

In this dissertation, we investigated the applications of the unique optical properties of microconical and microspherical structures in mesoscales. The structures interacting with light show different optical properties when their sizes vary at different spatial scales. The properties of structures with the millimeter-scale dimensions follow the laws of geometrical optics and they have been well studied in the optical science and engineering. Due to developing novel fabrication techniques, since the beginning of 2000-s the interest of photonics community switched to structures with nanoscale dimensions [1-10].

Mesoscale refers to the structures such as microspheres, microcones or other shape of structures with the characteristic dimensions on a scale of several wavelengths. Structures with such dimensions have different properties compared to both millimeter-scale and nanoscale optical components:

(i) They are capable of producing extremely tightly focused beams also termed photonic nanojets [11,12]

(ii) Mesoscale structures formed by dielectric microspheres can be used for super-resolution imaging applications [37-42]

(iii) Mesoscale structures with the circular symmetry such as microspheres and microcylinders are capable to resonantly trap light inside them due to total

internal reflection leading to formation of so-called whispering gallery modes (WGMs) with very high quality (*Q*) factors [74-77]

A combination of these properties leads to a broad range of applications of mesoscale structures and devices. In this dissertation, we are interested in the optical properties and applications of microconical structures and microspherical lenses with mesoscale dimensions. The operation of microconical structures can be compared to adiabatically tapered fibers. Due to strong reflections provided by the sidewalls, they can be used as light-concentrating structures. These properties are usually referred to as non-imaging light concentration properties to distinguish them from the focusing effects introduced by the lenses. Similar structures with the conical symmetry can be used for concentrating light in solar cells and other applications. Such light-concentration capability usually has non-resonant nature. However, such structures can also resonantly trap photons in circulating orbits similar to WGMs in microspheres or to Fabry-Perot microresonators in planar geometry. The terminology of "photonic nanojets" was originally introduced to represent the ultimate focusing capability of dielectric microspheres when it was demonstrated that under certain conditions, they can create light beams with subdiffractional dimensions. More recently, this terminology was applied to various mesoscale photonics structures including conical, cubic and other shapes. One particular application of such structures is related to concentration light beams directly on pixels of photodetector focal plane arrays (FPAs) used in imaging devices, especially in infrared (IR) cameras [221-231]. The studies of microspherical lenses revealed that their superfocusing capability is related to near-field optics effects which take place in close proximity to the surface of such objects. It can be assumed that the similar near-field optical properties can

be responsible for their super-resolution imaging capability [38,39,42]. It should be always remembered, however, that direct analogy between the focusing and imaging is usually not applicable to such structures. The fundamental basis for such analogy is given by the reciprocity principle in optics. However, the reciprocity principle can be applied only to the same optical modes. If different optical modes are responsible for focusing and imaging properties, the reciprocity principle is not applicable. This shows that the optical properties of mesoscale photonic structures can be rather complicated and divers. Usually, their study requires solution of Maxwell equations by numerical methods.

Chapter 1 is dedicated to the review of literatures. The outline of this introduction chapter is designed in an order corresponding to the following chapters in the dissertation. The paragraph 1.1 introduces the optical properties of mesoscale structures and devices. The paragraph 1.2 is devoted to different types of photodetectors in FPAs and to the problem of thermal noise in the uncooled FPAs. We also consider the designs and fabrication of silicon (Si) mesoscale light concentrators integrated with FPAs. In the paragraph 1.3 we discussed the fabrication methods for light concentrators built by low-index (n = 1.6) materials such as photoresist and plastics. In the paragraph 1.4, we introduce the development of super-resolution imaging technologies and resolution quantification procedures. In the paragraph 1.5, we discuss the technology and applications of assembling monolayer of microspheres.

In Chapter 2, we propose a high index (n ~ 3.5) Si microconical array for concentrating light on pixels of FPAs [221]. It can help to solve the problem of large thermal noise level of FPAs operating in mid-infrared (MWIR) and long-infrared (LWIR) wavelength range which affect the performance of such uncooled thermal imaging devices.

The thermal noise level can be reduced by decreasing the size of individual photodetector mesa of FPAs [172]. Therefore, light concentrators with the ability to collect incident light over a wide area and deliver and concentrate it into small areas of photodetector mesas are favorable for reducing the thermal noise level of photodetectors with small mesa sizes operating at room temperature. In the meantime, they can maintain a high efficiency of photon absorption, which potentially increase the sensitivity, signal-to-noise-ratios (SNRs) and the imaging qualities of uncooled thermal imaging devices. It should be noted that the simplest light-concentrating structure (imaging) is represented by a microlens, and the microlens arrays are available commercially. However, due to their long focal distances, they have rather limited angle-of-views (AoVs) that limits their applications. In this sense, different novel structures such as high-index microspheres placed in contact with the photodetectors, metalenses or microconical arrays have significantly shorter focal distances and, correspondingly, better AoV characteristics. [223-225,230,231]. Based on the well-established fabrication technology of Si microcone array by anisotropic wet etching of Si [176-178], we proposed three different designs of such structures operating in MWIR spectral range of $3\mu m < \lambda < 5\mu m$. We performed 3-dimensional (3-D) numerical solution of Maxwell's equations by finite different time domain (FDTD) using the software of Lumerical. We showed a power enhancement factor (PEF) up to 20 with a large AoV>20°. We also studied photon resonant trapping effects in such structures.

In Chapter 3, we studied similar optical properties in structures with much lower index of refraction such as $n = 1.6$. These structures can be fabricated by well-established technologies and tools such as Nanoscribe in the case of using photoresists or such as injection molding in the case of using plastics [222]. We performed 2-dimensional (2-D)

numerical analysis by FDTD and such low-index (n = 1.6) microcone array showed non-resonance performance similar to adiabatically tapered waveguide. The performance of the microconical structures was optimized by varying the geometrical dimensions of microcones. A theoretical 3-D power enhancement factor ~100 was predicted with a modest AoV ~15°. Such photoresist microconical arrays heterogeneously integrated with FPAs by Nanoscribe were previously fabricated by our collaborators in Air Force Research Laboratory (AFRL) [232-234]. The PEF values experimentally observed in such structures were found to be significantly reduced compared to maximally possible theoretical values. In our modeling work we show that this is explained by the suboptimal designs used in the previous experimental studies along with the structural imperfections in the fabricated devices.

In Chapter 4, we developed a novel label-free cellphone microscopy assisted by contact ball lens made by special glass LASFN35 with high refractive index of n = 2.02. It should be noted that it was a significant interest in improving the resolution of cellphone microscopy by various methods including microoptics solutions, but the best obtainable resolutions have been limited at approximately 1.5μm level [238, 271-273]. In our work we show that contact ball lenses with specially designed refractive index can overperform other approaches and reach almost diffraction-limited resolution values. Such proposed cellphone microscopy can be a perfect lightweight and inexpensive replacement of bulky and expensive conventional microscopes to achieve diagnostics of diseases such as melanoma *in vivo* without invasive biopsy. Our work builds upon recent advances in microsphere-based nanoscopy where smaller microspheres with diameters on the order of several wavelengths are used in combination with microscopes equipped with high-quality

objectives. In this work, it was shown that the resolution beyond standard diffraction limit in air (~λ/2) or even beyond so-called solid-immersion lens (SIL) limit becomes possible in such structures [38,39,42]. The mechanisms of super-resolution imaging by microspheres are debated in the literature. In our work, we used cellphone imaging by significantly larger ball lenses with the millimeter-scale dimensions using cellphone objectives with significantly lower effective numerical apertures (NAs) compared to the best microscope objectives. As a result, our resolution values are lower than standard diffraction limit, but they significantly exceed previous results obtained using cellphone-based microoptics solutions. In this chapter, we built a prototype of cellphone microscopy and illuminate the objects with white light to achieve label-free imaging. We studied the dispersion effect of the material of LASFN35 glass and quantified the additional magnification introduced by the contact ball lens at different illuminating wavelengths. A huge magnification up to 50× was achieved. We also demonstrated a sub-micron resolution of ~600nm which is two times better than previously published resolution values for cellphone-based microscopy [238]. A trade-off between large magnification and field-of-view (FoV) leads to inevitable reduction of FoV. One of the solutions of this problem is introduced in Chapter 5 due to parallel imaging through multiple ball lenses assembled as a regular array over sufficiently large millimeter-scale area.

In Chapter 5, we developed a technology to assemble a single layer of microspheres in highly ordered array using microhole arrays with diameters of the holes slightly smaller than the diameter of the microspheres. The microhole arrays can be fabricated by laser burning or mechanical drilling with great accuracy. An air suction can be provided through the microhole array forcing the microspheres to fill the microholes. The microspheres can

be either directly sitting in microholes or they can be embedded in plastic coverslips dependent on the applications. We proposed two applications for such microsphere arrays. The first is parallel imaging through multiple microspheres to extend FoV. The second is based on using individual ball lenses with high index of $n \sim 1.9$ or their arrays as "cat's eye" retroreflectors [216,217].

1.1.1 Studies of photonics in mesoscale structures

Two decades ago, the study of photonics moved into the area of nanoscale structures. These materials also termed metamaterials are artificially structured with a period which is much smaller than one illumination wavelength of the light. The structures can be fabricated in purely dielectric or metallic materials. Metallic structures support near-surface electron oscillations termed surface plasmons. In nanostructured metals there exist localized surface plasmon resonances. This leads to a great variety of electromagnetic (EM) resonant properties which can be studied in composite metallic-dielectric metamaterials [1]. These lead to many possibilities of manipulating EM waves in metamaterials which cannot be achieved by natural materials (where "meta" means "beyond" in Greek) [2-4]. A huge attention was brought to such nanoscale area and a wide range of applications such as biosensors for live virus [5], achieving super-resolution [6-8], thin film sensors [9], and superlenses [10] were developed.

Structures with the intermediate range of dimensions on the order of several wavelengths have received somewhat less attention. Whispering gallery modes have been studied in the mesoscale dielectric microspheres. Such microspheres have been also studied in a context of super-resolution imaging applications. However, properties of mesoscale

photonic structures depend on their shapes. Properties of mesoscale cubes, cones, pyramids and other shapes received somewhat less attention. Such structures in mesoscale can be very attractive in principle from the point of view of developing applications, since they showed three following unique optical properties which could not be realized by either smaller nanoscale structures or larger structures under geometrical limitations.

1.1.2 Extremely tightly focusing light into photonic nanojets

In 2004, the terminology of "photonic jets" was introduced to represent sub-diffraction dimensions of beams generated at the shadow-side surfaces of micron-scale, circular dielectric cylinders [11]. Based on conventional far-field wave optics, light passing through an optical element can be focused into a compact spot and the size of the spot is limited by the diffraction of light, which equals to $\lambda/2NA$, where NA is the numerical aperture on object space. Obtaining focused beams with sub diffraction-limited width is not a simple task. However, it is possible for mesoscale cylinders or spheres under special conditions.

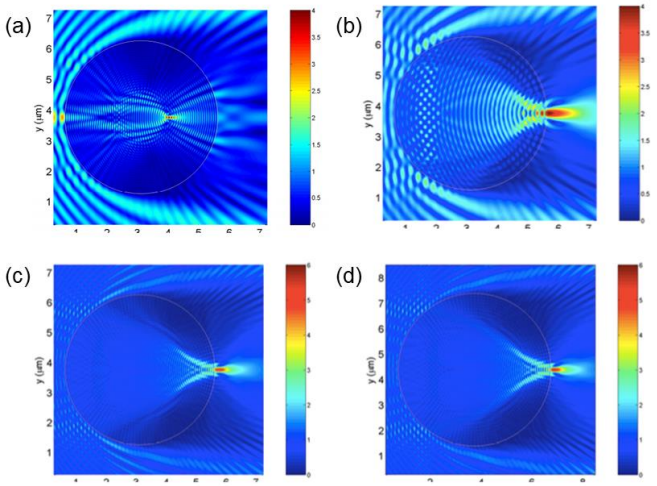

Figure 1.1: Evolution of a photonic nanojet as the variation of the diameter *d* of a plane-wave-illuminated circular dielectric cylinder and the refractive

index of the cylinder n_1 and surrounding material n_2 at illuminating wavelength λ. (a) d = 5 μm, n_1 = 3.5, n_2 = 1.0, λ = 500nm (b) d = 5 μm, n_1 = 1.7, n_2 = 1.0, λ = 500nm (c) d = 5 μm, n_1 = 3.5, n_2 = 2.0, λ = 250nm (d) d = 6 μm, n_1 = 2.3275, n_2 = 1.33, λ = 300nm. [11]

Using high-resolution FDTD numerical solutions of Maxwell's equations, the EM field distribution map showed how plane wave generated from the front surface and propagated through dielectric microcylinder was focused into a small compact nanojet-like beam on the back-surface of the cylinder. Fig. 1.1(a) and 1.1(b) showed that for microcylinder with a cross-section diameter of d = 5 μm in an environment with refractive index of n_2 = 1.0 illuminated by plane waves with wavelength λ = 500nm, there is a nano-jet shaped electric-field peak moved from inside the cylinder to the back surface of it when the refractive index of the cylinder n_1 is decreasing from 3.5 to 1.7. It has a waist of about 200nm, which is smaller than $\lambda/2$. The most surprising feature of this photonic nanojet is that it is neither evanescent nor diffracting. It can propagate along axial direction for about 900nm, which is slightly less than 2λ. The waist of the nanojet can be further narrowed if the refractive index of the environment is increased to n_2 = 2.0 and equivalently, decrease the wavelength to λ = 250nm. Fig. 1.1(c) shows a photonic nanojet with a waist of 120nm and a length of about 400nm. It is also shown that a similar geometry of photonic nanojet can be obtained if the value of n_1/ n_2 and d/ λ remain the same. Fig. 1(d) showed a similar waist of 130nm and length of 500nm of photonic nanojet under equivalent conditions. Since the size of the microcylinder is about 10 to 20 times larger than the illuminating wavelength, such case can be considered as mesoscale structures.

The diffraction limit is a far-field effect, and the formation of such narrow photonic nanojets beyond diffraction limit can be explained by the potential contribution of near-

field and evanescent-field since the focusing takes place very close to the surface of objects [12]. It is obvious that such photonic nanojets with striking properties of extremely narrow waists which beats the diffraction limit, and a long axial propagation will have a huge potential on developing different kinds of applications. Since the first evidence of photonic nanojets, this area has been actively developing leading to applications such as improving the performance of IR photodetectors [13,14], optical scalpels [15], laser surgery [16-22] and photolithography [23]. These applications become possible due to special properties of photonic nanojets such as an ability to focus high power into an extremely compact area and propagate for a long distance as well as to provide long-range low-loss optical transport through chains of optically coupled microspheres [24-35].In the latter case, the photonic nanojet formed on the back-surface of one microsphere becomes the incident beam for the next microsphere forming another photonic nanojet on its back-surface. As a result, the light propagates through such chain-shaped waveguide due to periodical focusing effects, as shown in Fig. 1.2. Another important application of photonic nanojet is its potential role in achieving super-resolution in microsphere-assisted microscopy. This application will be discussed in the following section.

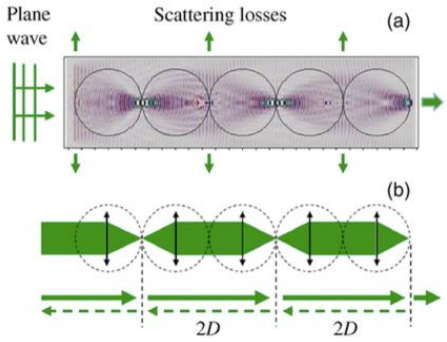

Figure 1.2: Theoretical model: (a) EM amplitude map calculated at λ=530.0 nm using incident plane waves, (b) Geometrical optics model of periodically coupled lenses with the focus distance $F=D/2$. [25]

1.1.3 Super-resolution imaging in microsphere-assisted microscopy

Since a sharply focused photonic nanojet with extremely narrow waist beyond the diffraction limit can be formed on the shadow-surface of microsphere in mesoscale, it seems attractive to view the imaging process as a time-reverse process where the object is replaced with a time-reversal mirror. This process would allow to apply a reciprocity principle according to which one can change the direction of propagation of light in the case if we trace the *same optical mode* in the backward direction. The words "same optical mode" is very important in this description since in a more general case when the modal composition of emitter does not coincide with the modal structure of focused beam (represented by photonic nanojet), the reciprocity principle is not applicable. Many groups working in the area of microsphere-based imaging considered only formation of photonic nanojets and associated the waist of photonic nanojet with the optical resolution of the system. However, this approach ignores the fact that the spatial emission properties of the source (object) are different from the spatial properties (such as directionality) of the nanojet. For this reason, the calculations of photonic nanojets, rigorously speaking, cannot be used for analyzing the resolution analysis in microsphere-based imaging. As it was pointed out in Ref. [36], the correct approach to the resolution analysis can only be based on solution of Maxwell equation considering the emission properties of the source. As an example, the source can be represented by a classical dipole emission which includes near-field contributions in close proximity to such emitter. Depending on the parameters, the microsphere can create a magnified real image of the source or its virtual image. In the latter case, the virtual image can be performed by reversing the direction of propagation of

the wave fronts to mimic the observation scheme in the optical microscope. Thus, this approach is free from the assumptions about the optical reciprocity, and it allows calculating the image directly. After dividing by the magnification of the system, the size of the image of a point dipole represents the resolution of the optical system. Analysis performed in Ref. [36] showed that the resolution of the microsphere-based imaging is different from the estimations based on calculations of the width of photonic nanojets. The resolution can reach approximately $\lambda/3$ for sources very close to the surface of microspheres with index 1.4 in the air environment. This means that for high-index microspheres (n~2) immersed in liquids or embedded in elastomeric slabs, with n~1.4, the resolution values can reach about $\lambda/5$ [36].

The imaging through dielectric microspheres was introduced in 2009 [37] paper based on analogy with the solid immersion lens (SIL). The true super-resolution well in excess of SIL resolution limit was first observed in 2011 [38]. It was a pioneering result which attracted a significant attention of photonics community to this area. The next important result was introducing imaging through high-index (n~2) liquid-immersed microspheres which made possible biomedical imaging applications of this technology [39].

Using microsphere in conventional microscope to obtain super-resolution has become one of the popular methods in microscopy. The standard schematic of such design is shown in Fig. 1.3. A microsphere made by barium titanate glass (BTG) with high refractive index of 2.1 is immersed in a coverslip with an index of 1.48 place on top of an Au cylinder nanoplasmonic array. The fluorescent (FL) nanospheres as the objects were distributed over the nanoplasmonic array. The whole sample was placed on a FL

microscope with 100× oil-immersion objective. The nanoparticles were optically excited, and their magnified virtual images were captured through BTG microspheres by microscope with a resolution of ~λ/7 [40,41]. Such experimentally determined resolution values turned out to be higher compared to the theoretical estimations (~λ/5) [36] that can be explained by additional factors such as formation of plasmonic "hot spots" in the nanoplasmonic array which are not included in the theoretical model of Ref. [36]. The diameter of microsphere they used here is about 45 μm, which is slightly larger than the conventional region of mesoscale structures, but this is because a larger microsphere which provides larger FoV is easier for an accurate quantification of resolution. The role of diameter of microspheres in achieving super-resolution is not well-established, but some results [42] indicate that achieving highest resolution values about λ/7 require use of smaller microspheres with the mesoscale diameters.

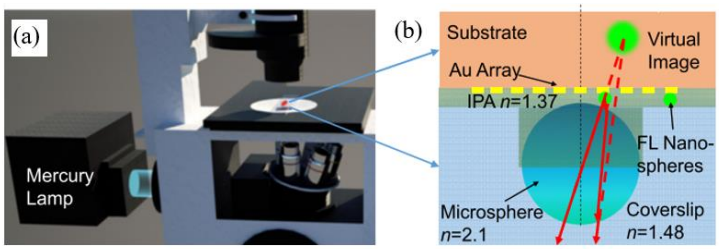

Figure 1.3: (a) Schematic of microsphere-assisted microscopy. (b) Schematic of imaging of fluorescent objects imaged by the microsphere. [40]

Another factor which facilitates increased resolution is represented by the use of nanoplasmonic structures as objects for imaging or as additional layers evanescently coupled to FL or non-FL objects. Super-resolution microsphere-based imaging have been reported in the presence of nanoplasmonic structures which can provide near-field enhancement of illumination both under FL conditions [43-59], and label-free conditions

[60-73]. The mechanisms of the super-resolution imaging in the microsphere-assisted microscopy are under intense debate [36]. The microspheres are forming magnified virtual or real images of the objects depending on the refractive index contrast between the microspheres and surrounding environment. Then the magnified images are captured by the conventional microscope and the resolution is improved due to the additional magnification introduced by the microsphere and some near-field effects since the objects are usually within the near-field region of microspheres.

The super-resolution capability of such microscopy assisted by a simple microsphere is extremely important for imaging biomedical samples. These applications became possible after introducing in 2012 imaging through high-index BTG microspheres [39] immersed in liquids. The current goals of developing microscopy in biomedical area are related to improving the resolution, observing deeper regions inside the body in vivo without invasive biopsy, and label-free imaging without injecting potentially poisoning dye molecules. Microscopy assisted by microspheres shows great potential in this area and a lot of new ideas based on such designs can be further developed.

1.1.4 Building up WGM by total internal reflection

Whispering Gallery Mode (WGM) was first explained using the example of propagation of sound waves along the internal walls of whispering galley of St Paul's Cathedral by Lord Rayleigh. The soundwave with long wavelength can be totally internally reflected by the sidewalls of a building. The acoustic wave completing one full rotation is resonantly enhanced under condition of constructive interference, as shown in Fig. 1.4(a). Similar principle can be applied to optical waves with much shorter wavelength

propagating in microcavities with the mesoscale dimensions. Microcavities with circular cross-section shapes such as spheres, cylinders, disks and rings, have the ability to strongly confine EM field along the inner surface of cavity due to total internal reflection (TIR) illustrated in Fig. 1.4(b) [74-77]. This leads to constructive interference of clockwise and counterclockwise waves which, in its turn, result in formation of standing WGMs illustrated in Fig. 1. 4(c).

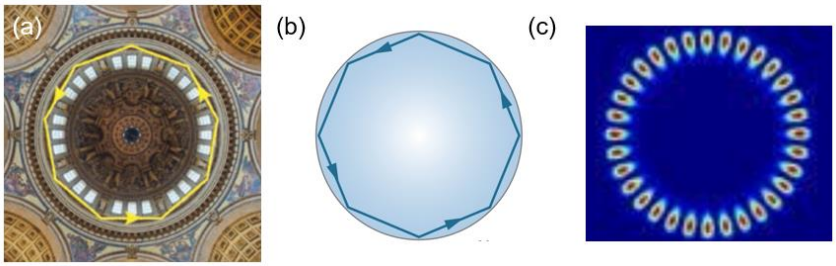

Figure 1.4: (a) Acoustic whispering gallery (b) Optical whispering gallery mode built up inside a microspherical cavity in mesoscale due to TIR (c) EM field map of whispering gallery mode inside microcavity.

WGMs can be excited spontaneously by exciting FL emission of the dye molecules inside the microspheres. Alternatively, they can be forced by evanescent coupling to tapered microfibers or totally internally reflecting prisms as illustrated in Fig. 1.5 [78].

Such coupling requires a strict condition of phase matching between the optical mode propagating in a fiber and WGMs in a microsphere [79] and a precise control of the distance between the tapered fiber and microcavity. Such coupling has been studied in literatures [80-98].

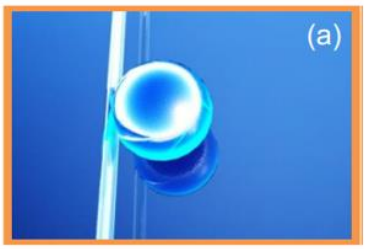

Figure 1.5: WGM by coupling microcavity with tapered waveguide. [78]

WGMs can also be generated by the photonic nanojet generated in chains of microspheres there are two mechanisms of optical transport. One is based on coupling between WGMs, but it requires a perfect resonance condition for uncoupled WGM resonances which is difficult to achieve. The second mechanism has nothing to do with WGMs, but it is based on relying on light along the chain microspheres considered as periodical spherical microlenses. WGM propertied coupled by photonic nanojets was widely studied [99-102].

A particularly important area is represented by WGM spectral sensors since the position of WGM resonant peaks is very sensitive to the presence of nanoparticles or to the index variations in the surrounding medium [103,104]. Fig. 1.6 shows a microfluidic platform integrated with tapered fiber to study the resonant spectra of WGM generated in the microsphere when it is coupled to the tapered fiber [105].

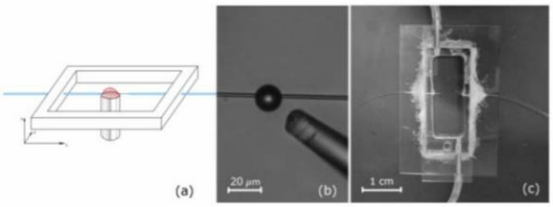

Figure 1.6: (a) Sketch illustrating the process of fiber etching in the meniscus above the vessel with hydrofluoric acid. (b) Positioning of a 16 μm sphere on the fiber with a piece of a sharpened optical fiber. (c) A photograph of the microfluidic cell with a tapered fiber and micropump tubing. [105]

The typical resonant spectra of WGM with narrow peaks representing different modes generated inside microsphere is shown in Fig. 1.7 [105]. The position of the peaks is determined by the properties of microcavity and surrounding environment. A tiny perturbation to either the cavity or the environment causes a shift of the peaks which can

be used in sensors. The detailed study of the sensing ability of WGM were found in literature [106-116]. The unique properties of WGM generated in different spherical microcavities can help to resonant optical force and optical propulsion which will realize optical sorting. [117-134]. The optical transport effects in optically coupled chains or arrays of can be applied to build focusing microprobes by integration of microcavities [135-141].

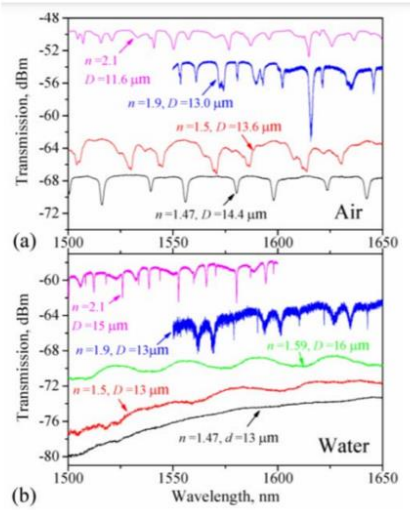

Figure 1.7: Fiber transmission spectra, measured in air (a) and in water (b) with the spheres attached at the thinnest place on the fiber (d~1.2 μm), as labeled on the graph. For clarity, the spectra are shifted vertically with respect to each other. The index and diameter of spheres is indicated. [104]

The three optical properties introduced above are intrinsic for mesoscale structures due to the fact that the typical dimensions of their building blocks are comparable (but larger) than the wavelength of light. This means that the optical near-fields play a larger role in these structures compared to their millimeter-scale counterparts. This also means that the geometrical optics is not applicable for describing EM phenomena in mesoscale structures. It also means that understanding of these phenomena in many cases require full

wave solutions of Maxwell equations considering optical near-field contributions and often requiring numerical computational approaches.

1.2 Microconical Si light concentrators for integration with FPAs

In this section, we give an introduction to the imaging system based on focal plane arrays (FPAs). First, we introduce different types of photodetectors such as III-V semiconductors, type-II superlattice (T2SL), quantum well IR photodetectors (QWIPs), and quantum dots IR photodetectors (QDIPs), along with Si photodetectors and PtSi Schottky-barrier detectors. After that we introduce the heterogeneous and monolithic integration of different types of photodetectors with integrated circuits (IC), and the two illuminating orientations as back-side and front-side illumination based on the fabrication techniques of photodetectors. Then we describe the cooled and uncooled imaging devices in the context of the problem of reducing their thermal noise. Finally, we discuss the technique of anisotropic wet etching of Si, which show the ability to fabricate Si microconical or micropyramid arrays in short time with low cost as a potential novel method of fabrication light concentrating structures integrated with FPAs.

1.2.1 Introduction of focal plane arrays (FPAs)

Focal plane arrays (FPAs) are arrays of photodetectors placed on the focal plane of an imaging system. The adventure of photodetectors began in the late XIX centuries when Smith first discovered photoconductivity in selenium in 1873 [142], Einstein explained the photoelectric effect in metal, and Plank introduced quanta hypothesis to explain the blackbody emission. In the early 1960s, the development of photolithography allows the

fabrication of Si monolithic FPAs, and the charge-coupled devices (CCD) camera developed in 1980s brought the photodetector technologies into modern age [143].

The photodetector techniques have been matured significantly allowing many kinds of imaging over an extremely broad spectral band from ultraviolet (UV) around 200nm to far infrared (FIR) around 100μm. In this dissertation, we are interested in photodetectors operating in MWIR and LWIR range of wavelength, which are the main tools for thermal imaging.

FPA is an integration of individual elements into a lattice-like structure. The pixels in a FPA are connected by contacts which determines the electrical and readout speed. The photodetectors are only a small part of the whole sensor devices. Besides photodetector pixels, a complete sensing system includes optics, cooling system (optional), pointing and tracking systems, readout integrated circuits (ROIC), processing system, communications and displays shown in Fig. 1.8 [144]. For FPAs operating in IR range, we often consider the structure of the 2-D photodetector arrays connected with indium bumps to a ROIC as an assembled sensor chip.

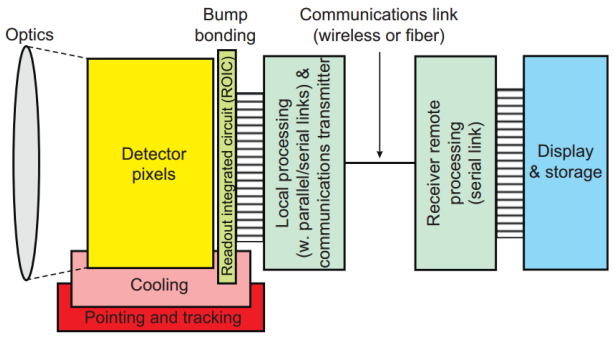

Figure 1.8: Schematic representation of an imaging system showing important sub-systems. [144]

With so many different elements in an imaging system, the photodetectors are possibly the most important component that influence the performance of the system. Photodetectors are sensors of photons or other EM radiation [145]. There are many types of photodetectors determined by the detecting mechanism. The typical semiconductor-based IR photodetectors are the mostly widely used photovoltaic detectors, which are based on the p-n junction inside the semiconductor materials that converts photons into electric current.

The photons incident into p-n junctions of photodetectors with higher energy than the energy gap can create electron-holes pairs which will create photocurrent. It is obvious that efficiency of converting the incident photons to charge carriers created by absorption is the key factor that influence the performance of photodetectors. We define this factor as quantum efficiency (QE). Different semiconductor materials have different QE which provide a guidance of fabricating photodetectors with better performance.

It is well-known that materials with direct bandgap have strong absorption coefficient which lead to a high QE > 95%. III-V semiconductors and HgCdTe shown in Fig. 1.9 became the main materials with direct bandgap for short-infrared (SWIR) and MWIR detectors, respectively, with the best quantum efficiency and low dark current at low temperature [146].

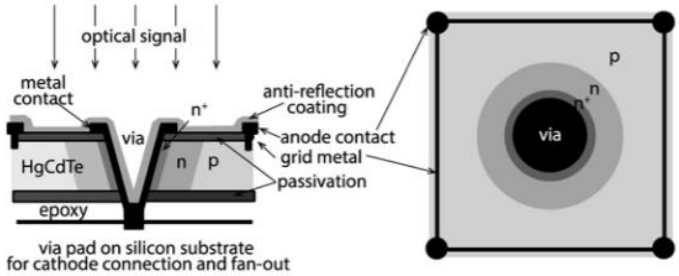

Figure 1.9: Schematic of the HDVIP® HgCdTe APD, left: side view; right; top view (Conceptual drawing only, the layer thickness and the via size not to scale). [146]

Another type of photodetector with high quantum efficiency, Type-II InAs/GaSb superlattice (T2SL), which represents a periodic structure with alternating InAs and GaSb layers, was proposed in 1970s [147]. The type II alignment of gap leads to a separation of electrons and holes into different layers of InAs and GaSb, respectively [148]. Such superlattice (SL) has several advantages such as reducing the dark current [149], and large tunability of band edge energies which could increase the operating temperature [150,151]. Fig. 1.10 shows the schematic of a novel SWIR heterojunction phototransistors based on T2SL [152].

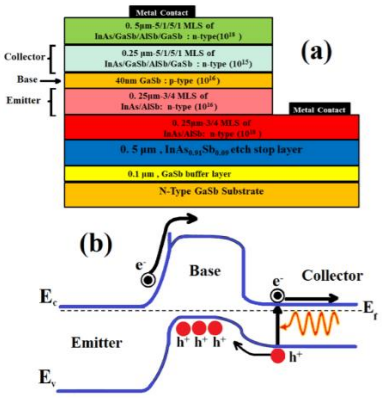

Figure 1.10: (a) Schematic of the heterojunction phototransistors design and structure. (b) Schematic energy-band diagram of the SWIR heterojunction phototransistors. [152]

Another type of III-V semiconductor photodetectors based on quantum well (QW) with very fast time response was proposed for IR photodetectors [153]. Such photodetectors use inter-subband transitions in quantum well with discrete energy transitions to absorb photons. Quantum well IR photodetectors (QWIPs) are one of the simplest quantum mechanical devices operating in MWIR and LWIR. Their advantages are high speed, high stability, and high pixel-to-pixel uniformity [154]. However, they

require low operating temperature due to its high thermionic emission rate [155]. Also, another disadvantage of n-type QWIRs is that they cannot detect incident radiation in normal direction due to the polarization selecting rules [156]. Fig. 1.11 shows the schematic of a AlGaN/GaN step QW MWIR photodetectors and the corresponding conduction band profiles [157].

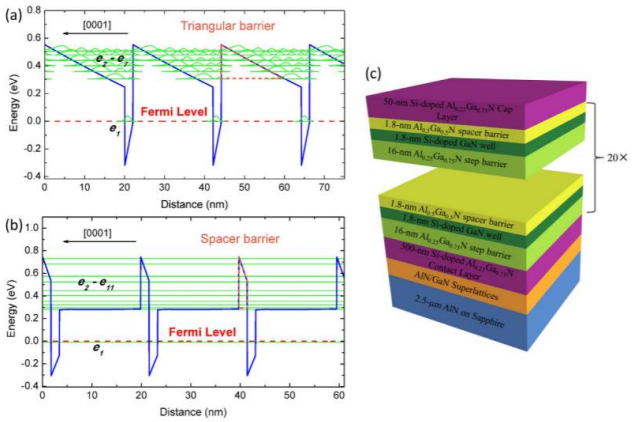

Figure 1.11: (a) Conduction band profile of $Al_{0.35}Ga_{0.65}N$/GaN (20nm/2nm) multiple-QWs and the triangular barrier (orange dashed line). (b) Conduction band profile of $Al_{0.5}Ga_{0.5}N$/GaN/$Al_{0.25}Ga_{0.75}N$ (1.8nm/1.8nm/16nm) step-QWs designed for B-to-QC ISBT and the spacer barrier (orange dashed line). (c) Schematic image of the designed sample structure. [157]

Similar designs of IR photodetectors were proposed by replacing the quantum wells by quantum dots (QDs). Quantum dots are semiconductor particles with a size of a few nanometers. Such quantum dots IR photodetectors (QDIPs) are different from QWIPs that they are sensitive to all directions of incidence including normal incidence, which allows a 3-D confinement of electrons in quantum dots [158-162]. Also, the thermionic emission rate of QDIPs is lower than QWIPs, which reduces the thermal excitations and allow a higher operating temperature and lower dark current [163]. Fig. 1.12 shows a schematic of n-i-n QDIPs based on InAs self-assembled quantum dots [155].

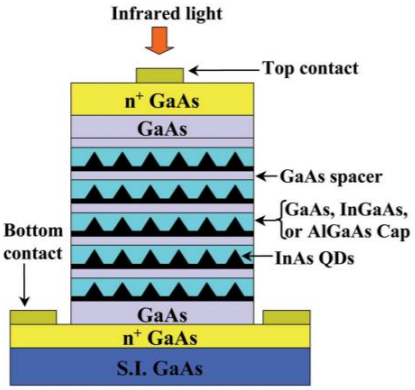

Figure 1.12: Schematic cross-section of n-i-n quantum dot infrared photodetectors (QDIP). [155]

We introduced several different types of photodetectors with high QE made mainly by III-V semiconductors with direct bandgap. However, such photodetectors made by III-V semiconductors requires heterogeneous integration with Si-based IC to read and process the signals collected by the photodetector arrays enable to display the image. Heterogeneous integration (HI) refers to the integration of components which are separately manufactured into a higher-level assembling [164]. Such integration can be difficult considering the alignment of photodetector mesas and electric circularity contacts with high accuracy.

An alternative approach is presented by a monolithic integration of photodetector and IC. The major material of IC Si can also be used to build IR photodetectors which allows a monolithic integration of photodetectors with the electric circuits. In this case, the manufacturing of Si photodetectors and Si integrated circuits can be achieved at the same time during single photolithography in Fig. 1.13. However, the QE of single p-n junction is limited by a well-known rule of Shockley-Queisser (SQ) limit [165] that the energy band gap of the semiconductor determines the minimum photon energies that can be converted into charge carriers. In the case of Si, photons with energies corresponding to MWIR and

LWIR spectral ranges experience its indirect bandgap resulting in much smaller absorption coefficients compared to direct bandgap materials. The low QE of IR photons is the main drawback of Si photodetectors.

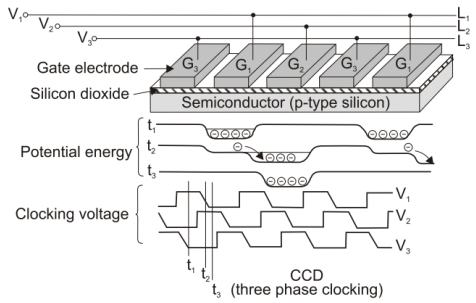

Figure 1.13: Monolithic Si focal plane arrays of CCD. [143]

Another type of IR photodetector was proposed by using Schottky barrier. A popular design of Si photodetector is represented by a metal-semiconductor junction. When a metal is directly deposit on n-type semiconductor without any other material layers in between, a Schottky barrier can be created which leads to a rectifying behavior of electrical contact shown in Fig. 1.14. When device is forward biased, the major carriers can be easily moved from *n*-type semiconductor into metal layer. Therefore, the thermionic emission rate is much higher than in the case of *p*-*n* junction, and the saturation current in Schottky-barrier detector is several orders of magnitude higher.

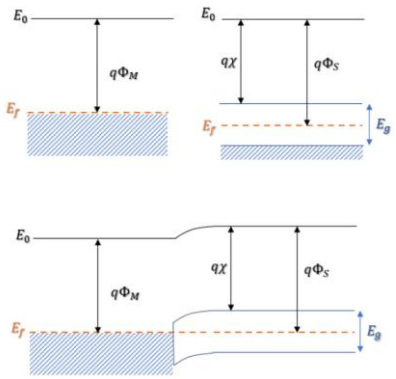

Figure 1.14: Band diagrams of metal and semiconductors when they are not in contact (up) and when they are in intimate contact.

The first silicide (metal-Si) Schottky-barrier detector FPAs was proposed in 1973 [167]. The widely used silicide Schottky-barrier detector is PtSi, which can be applied to MWIR range of 3μm to 5μm. Fig. 1.15 shows the schematic and operation of PtSi detector integrated with a Si CCD [168]. For monolithic Schottky-barrier photodetectors, a smallest pixel size of $17\times17\mu m^2$ was developed on a 1040×1040 element array among 2-D IR FPAs [169]. It should be noted that PtSi detectors have very low quantum efficiency in MWIR spectral range from 3μm to 5μm around 1%, but excellent imaging can be achieved at room temperature by full frame integration in area arrays [170]. Unfortunately, the development PtSi Schottky-barrier detectors has been stagnated in recent 20 years [170,171].

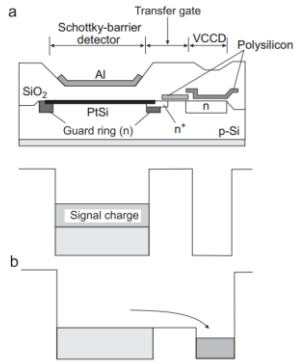

Figure 1.15: Typical construction and operation of PtSi Schottky-barrier IR FPA designed with interline transfer CCD readout architecture. (a) and (b) show the potential diagrams in the integration and readout operations, respectively. [168]

1.2.2 Illumination and temperature regimes

We discussed several different IR photodetectors made by high-QE materials such as III-V semiconductors and QD, and low-QE materials such as Si and silicide PtSi Schottky-barrier detectors. The integration of different photodetectors with integrated

circuits can be realized for front- and back-illuminated photodetectors. Fig. 1.16 shows the schematic of back-side and front-side illuminations. The back-illumination represents that the radiation is incident into photodetector region first with integrated circuits below. The front-illumination represents that the radiation incident into the circuit's region first, then absorbed by the photodetecting area below the circuits. The conventional fabrication techniques of photodetectors are easier for front-illuminating devices and the back-illuminated photodetector is a novel approach to arrange the imaging elements to increase the photons absorbed by photodetectors. The front-illumination orientation is usually applied to heterogeneous integration of high-performance photodetectors by III-V semiconductors, T2SL and QDIPs with Si ICs. On the other hand, the monolithic integration of PtSi Schottky-barrier detector with circuit connections is usually achieved using back-side illumination.

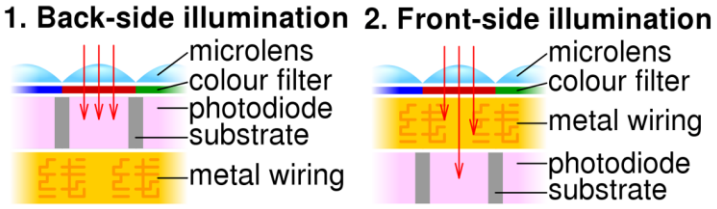

Figure 1. 16: Schematic of back-side and front-side illuminations.

We introduced different types of photodetectors made by high efficiency materials such as III-V semiconductors and QD, and low-efficiency materials such as Si or silicide, and the methods of integration of photodetectors with electricity circularity connections and illumination orientations based on different integration. Now we are ready to consider other parts of the whole imaging system.

Fig. 1.17 show the operating temperature varies for the IR photodetectors operating in different sub-spectral ranges. We can tell that for MWIR photodetectors which we are interested in this dissertation, a cooling system is required to operate in a low temperature around 100K.

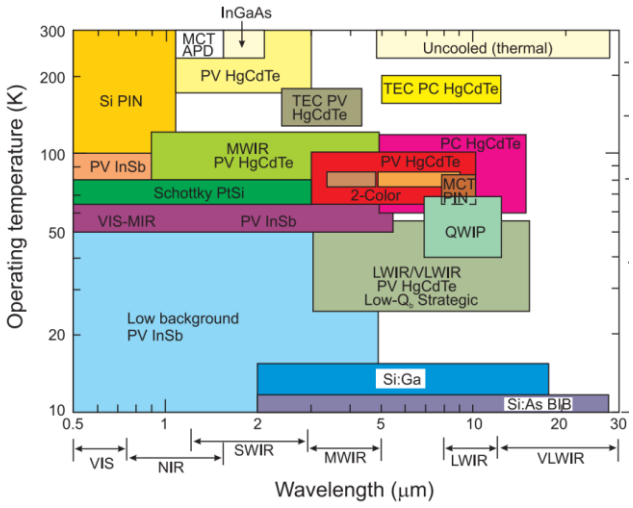

Figure 1.17: The operating temperature and wavelength regions spanned by a variety of available IR detector technologies. [143]

The uncooled imaging system operating in a range of temperature slightly below room temperature of 250K to 300K on the other hand, shows a huge advantage in budget, power supply, and reducing the size and weight of the devices, but the large thermal noise level limits the imaging quality and sensitivity of the imaging system.

The factors that influence the thermal noise level of photodetectors can be very complicated, however it was shown by Jones that for many detectors, the noise equivalent power (NEP) is proportional to the square root of the detector signal that is proportional to the detector area A_d [172]. The noise current I_n is defined by Jones as:

$$I_n^2 = 2\phi_B \times A_d \times \eta \times q^2 \times g^2 \times \Delta f, \quad (1.1)$$

Where ϕ_B is background photon flux density, η is the quantum efficiency, q is the electron charge, g is the photoelectric current gain, and Δf is the frequency band. The reduction of the noise can thus be achieved by reducing the area of photodetector which is particularly important for uncooled systems.

However, with the decreasing of photodetector area, the total amount of photons that can be collected by the detectors with larger area will be reduced, which leads to a negative impact on the imaging performance. In principle, this problem can be solved by using a light concentrating structure with the simplest example given by a microlens array illustrated in Fig. 1.18.

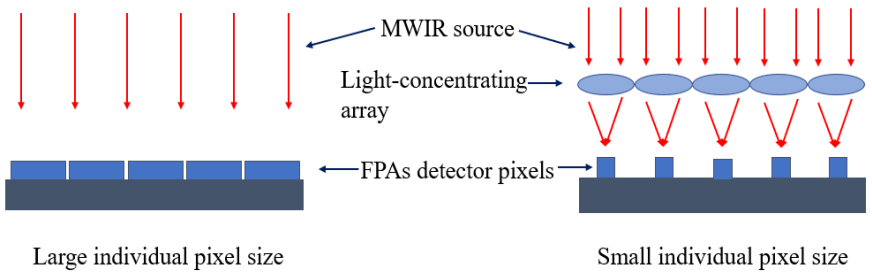

Figure 1.18: The schematic of collection of radiation over a large area by photodetector array with large pixel size (left), and by light concentrator array which concentrate and focus light into small areas of photodetectors (right).

The idea of non-imaging light concentrators was first brough up in the developing of efficient solar cells such as compound parabolic concentrators [173] and Köler integrators [174]. Fig. 1.18 shows the principle of microlenses array as light concentrators associated with FPAs. A high level of photon collection efficiency for FPAs with smaller mesa sizes can be maintained by focusing light over a wide area by light concentrators into small detecting pixels, which leads to a high-response level and a low thermal noise for the uncooled imaging devices.

1.2.3 Anisotropic wet etching of Si

Besides the previous designs of light concentrators varying in materials and shapes, Si has attracted our attention since it is the major material in microelectronics such as building integrated circuits, which could simplify the fabrication and integration of light concentrators and photodetectors, and it has extraordinary mechanical properties [175]. The anisotropic wet etching of Si is a typical bulk micromachining method which is dependent on crystallographic directions, and the etching rate is always much faster in one crystallographic direction than in another, which will expose the crystal planes with slowest etching speed after a period of etching [176].

The most commonly used aqueous alkaline solutions of anisotropic wet etching are potassium hydroxide solution (KOH) [177] and tetramethylammonium hydroxide (TMAH) [178], in which the (1,1,1) crystal plane has the slowest etching rate. The (1,0,0) Si wafer is covered by mask in Fig. 1.19. The etching starts at the exposed parts and the (1,1,1) crystal planes will form an angle of 54.7° with the horizontal directions of (1,0,0) Si wafer. Based on this idea, photomasks in the shape of circles or squares covering the (1,0,0) Si wafer with other parts exposed can be used to etch microcone or micropyramid arrays on Si wafer.

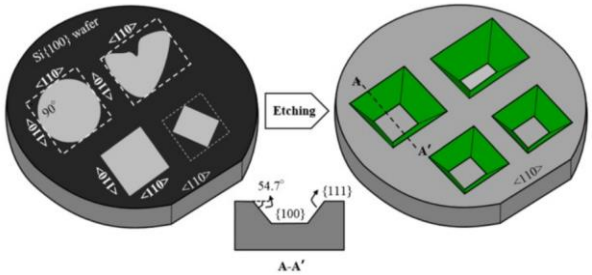

Figure 1.19: Schematic representation of the etched profile using (1,0,0) Si wafers. [176]

Other shapes can also be fabricated by using Si wafers with different orientations and etch along different crystal planes, but we will not discuss too deep into this area. The anisotropic wet etching of Si has the advantage of low-cost, fast fabrication speed with massive number, simple fabrication procedure and setup, and easy operation. Such ability to fabricate microconical or micropyramid arrays on Si wafer is interesting for us to design light concentrator arrays in Si integrated with FPAs.

1.3 Microconical low-index (n ~ 1.6) light concentrators

The main property expected from the photoresist is transparency in MWIR and LWIR regimes. There are low-index materials such as special type of photoresin IP-Dip and plastic material polyethylene terephthalate (PET) which are relatively transparent in MWIR and LWIR regimes. Their typical transmission spectra are shown in Fig. 1.20(a) and 1.20(b), respectively. There are still approximately half of the power at absorbing band at λ ~ 3.4μm can be delivered to the photodetector mesa after passing through 150μm thickness IP-Dip layer, and the PET can be considered completely transparent over the whole MWIR band.

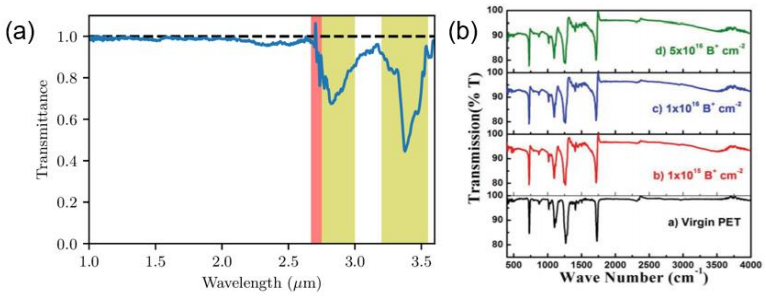

Figure 1.20: (a) Absorption spectrum of a thin homogeneous film of made of the developed photoresin IP-Dip. The thickness of the layer is 10 μm. [209] (b): FTIR spectra of PET (a) Virgin and implanted at 50 keV to (b) $1x10^{15}$, (c) $1x10^{16}$ and (d) $5x10^{16}$ B^+ cm^{-2}. [179]

We are looking for materials to be designed as light concentrators arrays with mature fabrication technology. There are two major fabrication technologies for low index (n = 1.6) materials: 3-D printing of micron-size structures by laser-writing on photoresist such as IP-Dip using commercial devices such as Nanoscribe, and injection molding of plastics with low melting temperature to fabricate any structures in the shape of designed mold.

Fig. 1.21(a) shows the commercial Nanoscribe tool which is a 3-D printing device in micron-scale using photoresist such as IP-dip and IP-L. A designed structure in photoresist is recorded (or "inscripted") by a focused laser beam. In the case of positive photoresist, the desired structure can be obtained after dissolving the unexposed parts of the sample. Such Nanoscribe 3-D printing devices have been widely used in fabricating photonic structures with the micron-scale accuracy as shown in Fig. 1.22(b). Since this is a point-by-point fabrication, the laser inscription can be a rather slow process which is a disadvantage of this method.

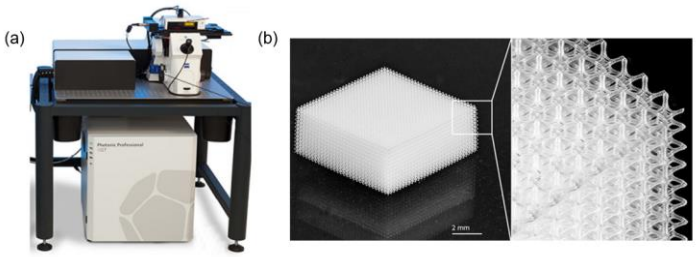

Figure 1.21 (a) Naoscribe nanoscale 3-D printing machine (b) Capability of fabricating accuracy.

Another fabrication method of micron-scale structures with massive number is injection molding of plastic [180]. Plastic with low melting temperature is melted and injected into a split mold by a syringe. After cooling, the mold is split, and the designed

structure can be taken out shown in Figure 1.22(a). Such fabrication method can also achieve a very high accuracy in several microns illustrated in Fig. 1.22(b). The “posts” on the top of the main structure have a dimension of 3μm ×3μm. The injection molding method is capable of fabricating massive number of micron-scale structures in a short time, so it is preferred for its fast fabrication and low cost in industry.

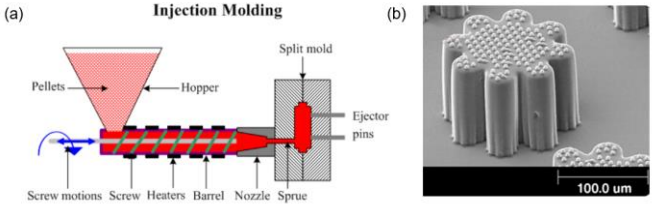

Figure 1.22: (a) Schematic of injection molding process of plastic (b) Capability of fabricating accuracy, the “posts” on the top have a dimension of 3μm ×3μm.

1.4 Super-resolution microscopy

Resolution of an imaging system shows the ability to resolve small feature size, and it is the most important parameter to determine the performance of imaging system. Exploring the extremity of resolution capability is the eternal task for microscopy and it is crucial to a wide range of applications especially in biomedical area for diagnostics of diseases. In this section, we first introduce the definition and limitation of resolution, and then we introduced the development of techniques to achieve super-resolution. In the end, we discussed several different methods of resolution quantification.

1.4.1 Definition and diffraction limitation of light

In the case of incoherent imaging, each point on the object plane can be considered as an independent point source. After passing through an imaging system, the point will be

imaged as a spot with a finite size. Such broadening of points into spots is due to the limited resolution capability of imaging system. A better imaging system with higher spatial resolution will image a smaller spot from a point. However, the size of the imaged spot cannot be infinitely small which is limited by diffraction of light.

Several different criteria for quantifying resolution were proposed based on the condition of aberration-free imaging system neglecting SNR such as Abby criteria [181], Rayleigh criteria [182], Sparrow criteria [183], and Houston criteria [184].

In 1873, Ernst Abby first proposed a resolution limit with coherent illumination based on Fourier optics by using grating objects with periodic structures [181,185,186]. The diffraction angle through the grating is increasing as the spatial frequency of the grating is increasing, and the size of the aperture stop on the back focal plane of the lens is limiting the acceptable diffraction angle of the lights to form images, thus the spatial resolution cutoff, which corresponds to the resolution, is related to the aperture size of the lens and the illumination angle [185]:

$$d = \frac{\lambda}{2NA}, \quad (1.2)$$

Where d is the full period of the grating, and NA is the numerical aperture, it can be expressed as:

$$NA = n\sin\theta, \quad (1.3)$$

Where n is the refractive index in the object space, and θ is the half-angle of the maximal acceptance angle of incident light that can be collected by the imaging system shown in Fig. 1.23.

Abby suggested that the spatial resolution is proportional to the illuminating wavelength and inversely proportional to the NA of the imaging system. Such criteria are

also proposed by Helmholtz at the same time [187]. For conventional optical microscope with visible white light illumination, the best resolution capability is up to $\lambda/2$ when consider NA is approaching to 1, which is around 200nm to 250nm.

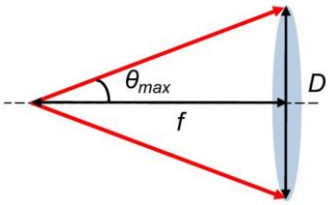

Figure 1.23: Illustration of NA of an imaging system of lens.

Rayleigh first proposed the criteria of resolution quantification for two self-illuminous incoherent points as Airy disks. It is claimed that the two point sources are just resolved if the central maximum of the intensity diffraction pattern produced by one point source coincides with the first zero of the intensity diffraction pattern produced by the other shown in Fig. 1.24 [188]. The Rayleigh criteria was generalized to include point-spread functions (PSFs) with no zeros next to their central maximum, by taking the resolution as the distance for which the ratio of the value at the central dip in the composite intensity distribution to that at the maxima on either side to be 73.6% and 81.1% determined by either circular or square shape of the aperture, respectively [188].

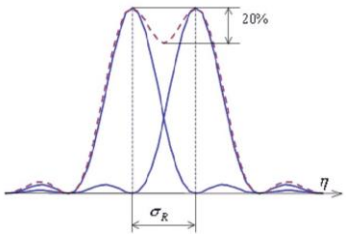

Figure 1.24: Illustration of spatial resolution defined by overlapping of diffracted patten as Airy disks of two-point sources.

The Sparrow resolution criteria is similar to Rayleigh criteria based on two-point incoherent sources, but with the consideration that no well-recognized zero intensity in the diffraction pattern can be found due to the “undulation condition”. So, it was suggested that the two-point incoherent sources with same intensity separated by a distance can be resolved when the second order derivative of the composite intensity distribution reaches zero at the central dip [183,188].

The last criteria were proposed by Huston in 1972 that the two-point incoherent sources with same intensity separated by a distance can be resolved when the distance between the two central peaks of diffraction pattern equals to the full width at half maximum (FWHM) of each individual diffraction profile of point source [184]. In this thesis, we are using Houston criteria for resolution quantification.

1.4.2 Development of techniques of super-resolution microscopy

For conventional microscope, the resolution is limited by the diffraction of light. The best objective with extremely close working distance in micron scale can achieve an acceptance angle near 1. In this case, the only option to further improve the resolution is increasing the refractive index in object space by designing liquid-immersion objectives. Based on a formula for diffraction limit, liquid-immersed objective can provide resolution improved by the factor of n_0, where n_0 can be as high as 1.74 in the case of diiodomethane [189,190].

Liquid immersion microscopes are the best techniques for far-field diffraction-limited resolution. An even better resolution beyond the diffraction limit can be achieved by obtaining information from the near-field evanescently coupling with the objects shown

in Fig. 1.25. The evanescent field is generated from the surface wave propagating along horizontal direction. Such surface wave decays away from the surface exponentially. The subdiffraction-limited details can be visualized once the evanescent wave is captured and projected to the far-field. [191].

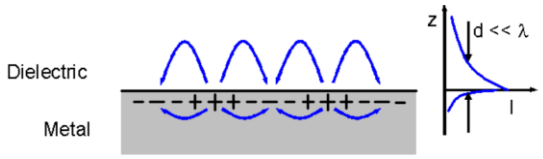

Figure 1.25: Schematic representation of a surface wave (surface plasmon polariton) propagating along a metal-dielectric interface.

In 1980s, the near-field scanning optical microscope (NSOM) was first proposed [192]. The probe is placed very close to the surface of specimen in a distance $d << \lambda$ to simultaneously scatter and collect evanescent waves in near-field region to collect higher spatial frequencies [191]. Fig. 1.26 shows the schematic of NSOM including a probe, a microscope objective, and a scanning attachment in three directions. The resolution is determined by the diameter of the probe aperture and the distance between the tip of the probe and the specimen, both of which have to be much smaller than the illuminating wavelength to achieve resolution beyond far-field diffraction limit [192].

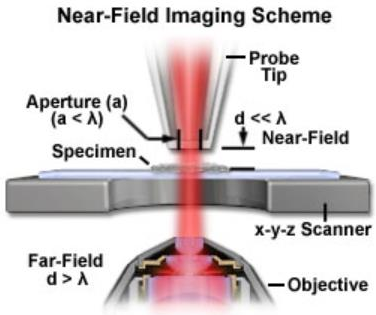

Figure 1.26: Schematic of near-field scanning optical microscope (NSOM). The probe has a diameter of the aperture and the distance to the specimen much less than the illuminating wavelength.

The evanescent field can be further amplified, and super-resolution can be achieved based on these techniques. In 2000, Pendry first proposed to build “perfect lens” by metamaterial structures with negative refractive index [2]. It was claimed that such perfect lens is able to focus both the propagating and evanescent waves. However, such perfect lens requires that the object and image are located in the near-field proximity to the lens which is not possible for remote imaging. It also does not have the ability to magnify image.

An advent of the perfect lens concept has stimulated an entire area of superlens and hyperlens imaging. A 2-D plasmonic nanoscope (2DPN) use the imaging magnification at plasmonic wavelength which is much shorter than that in the air to achieve a super-resolution ~λ/8 [193]. A far-field superlens (FFSL) was proposed to enhance the evanescent waves and convert them into propagation waves and a super-resolution ~λ/6 was achieved [194]. An anisotropic metamaterial with hyperbolic dispersion is designed as hyperlens which can provide magnification in a cylindrical geometry [195,196]. The design based on the far-field time reversal (FFTR) of object with near-field scatterers achieved a super-resolution up to ~λ/30 [197].

Another way of achieving super-resolution is using metal-substrate structures such as nanoplasmonic and metamaterial structures which can create higher spatial frequency illumination patterns. Plasmonic structured illumination microscopy (PSIM) was proposed where the interference pattern was created by counter propagating surface plasmon polariton (SPPs) waves, as illustrated in Figure 1.27 [198]. A 2.6-times advantage of resolution was claimed. A metamaterial-assisted illumination nanoscopy by hyperbolic

metamaterials was proposed with a 6-times advantage of resolution in label-free imaging down to 80nm [199].

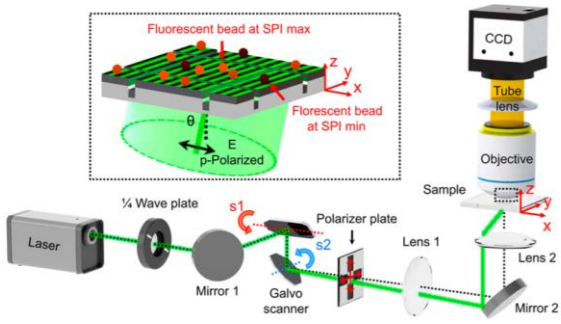

Figure 1.27: Schematics of the PSIM system. [198]

Microspherical superlens imaging (MSI) is another direction to achieve super-resolution. A self-assembled plano-spherical nano solid immersion lens (nSIL) was proposed [37]. Figure 1.28 shows the optical microscope image of the plano-spherical lens and the magnifying ability when it is placed on top of structures. Fig. 1.28(b) shows the pattern with 220nm spacing can be resolved leading to a resolution ~λ/3.

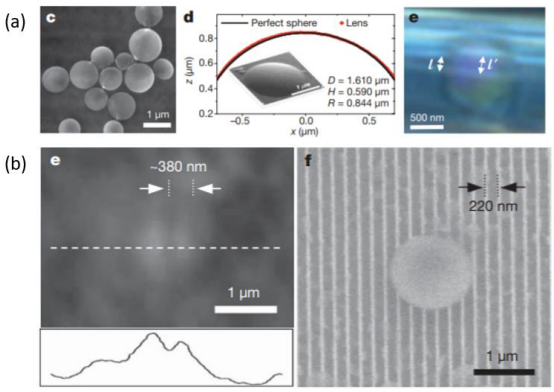

Figure 1.28: (a) Optical microscope image of plano-spherical lenses on a CHQ nanotube crystal, showing the magnification by the lens. (b) The sub-diffraction-limit patterns cannot be resolved in conventional optical microscopy, but the magnifying effect through the lens allows the stripe patterns of 250/220 nm spacing to be resolved. [37]

A pioneering development in this area was observation of virtual imaging with resolution exceeding the SIL values in 2011 by Zengbo Wang et al [38]. Silica microspheres with index $n \sim 1.46$ and diameters $2 < D < 9\mu m$ were deposited in contact with the sample in Fig. 1.29(a). The virtual images formed by the microspheres were captured by the white-light microscope. The objects of stripe arrays with 360nm width and 130nm separation, and array of circles with 50nm diameter and 50nm gaps can be clearly resolved, as illustrated in Fig. 1.29(b). A super-resolution ~ $\lambda/8$ to $\lambda/14$ was claimed. Later, by using rigorous resolution criteria, it was shown that the resolution of white light imaging through microspheres is closer to ~$\lambda/7$ [6,39,65] which still significantly exceed the SIL limit determined by the far-field diffraction.

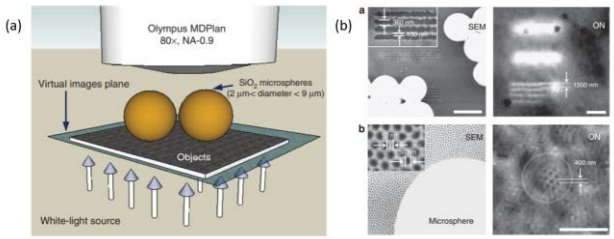

Figure 1.29: (a) Schematic of the transmission mode microsphere superlens integrated with a classical optical microscope. (b) Objects of stripes with 360 nm width and 130 nm spacing are clearly resolved, and a gold-coated circular array with 50 nm in diameter and 50 nm gap are clearly resolved. [38]

The next significant development in this area was a proposal and realization of imaging through high-index microspheres which are able to produce strongly super-resolved virtual images in the aqueous environment [39]. This work was directed by my research advisor at UNC-Charlotte and the significance of this work was due to the fact that it made possible imaging biomedical samples such as cells which exist in a liquid form [39]. In this work it was proposed to use the microspheres made by BTG with high index

n ~ 1.9-2.1. The BTG microspheres with diameters about several microns were deposited on top of the objects immersed in isopropyl alcohol (IPA) with an index of 1.37. The virtual images through the microspheres were captured by the standard upright microscope as illustrated in Figure 1.30. The resolution estimation (~ λ/7) was performed based on observation of minimally discernable features without using a convolution with the PSF. It was markedly poor resolution value compared to that claimed in Ref. [38], but many experimental studies performed more recently based on rigorous resolution criteria confirmed that the resolution of microsphere superlens nanoscopy is indeed close to ~ λ/7 [36]. It is interesting that the observed resolution was still better than the SIL resolution limit which is about λ/4 for high-index liquid-immersed microspheres. The dependence of magnification on the microsphere diameter was also measured for the first time in [39]. The following studies [42] showed that this super-resolution capability is a property of mesoscale microspheres with diameters on the order of several microns. For larger microspheres with diameters in 50μm < D < 220μm range the resolution was found to be closer to ~ $\lambda/4$ values.

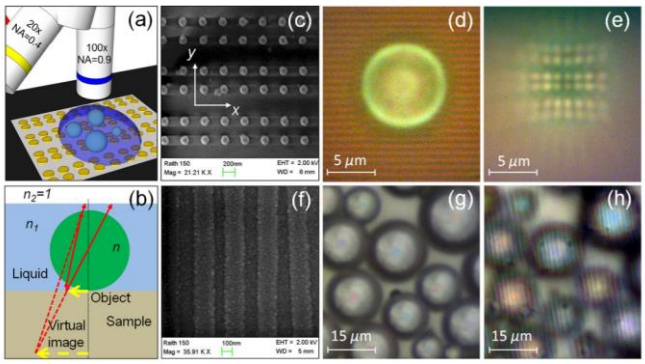

Figure 1.30: (a) Schematic of the setup; (b) Virtual image formation by a liquid-immersed sphere; (c) SEM image of an array of gold dimers formed by 120 nm nanoparticles with 150 nm separations; (d) BTG sphere with n=1.9 immersed in IPA; (e) Virtual imaging of the array shown in (c) through the microsphere at a different depth compared to (d) by 100× (NA

= 0.9) objective; (f) SEM image of a Blu-ray disk with 200 nm width stripes separated by 100 nm width grooves; (g) BTG microspheres with diameters in the range 5–20 μm fully immersed in IPA; and (h) Virtual imaging of the Blu-ray disk through the microspheres at a different depth compared to (g) by 20× (NA = 0.4) objective. [39]

Use of contact microspheres for imaging can be viewed as a natural progression of development SIL concept from hemispherical SIL (hSIL) to superspherical SIL (sSIL) to MSI [42]. Fig. 1.31 shows that MSI has much better resolution capability than other types of SILs with a higher additional magnification through the microspheres.

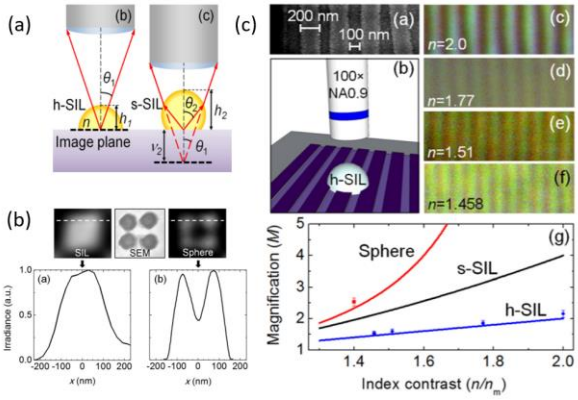

Figure 1.31: (a) Schematic of h-SIL and s-SIL. (b) Middle inset is the SEM image of the 4-cylinder structure with 50-60 nm gaps between 100 nm cylinders. (c) SEM image of a Blu-ray Disk and schematic of the SIL setup. [42]

The main application areas of super-resolution imaging through microspheres include the biomedical imaging where it can be used for imaging subcellular structures and viruses [203,204]. In addition, MSI can be used for inspection of computer chips.

1.4.3 Methodology of resolution quantification

Resolution quantification is a key for comparing different microscopy methods, but it requires careful methodological approach. Theoretical definition is based on using

incoherent point sources. Such sources can be easily realized in FL microscopy. In the case of label-free microscopy, however, the sufficiently bright point sources are not easily available, and the textbook recipe requires a convolution with the PSF [202]. Historically, several approaches have been used for the experimental resolution quantification in MSI. The first was semi-quantitative approach based on determining the minimally resolved feature sizes (MRF) [38,39,200,201]. The next approach was based on one-dimensional (1-D) convolution [42,203]. This approach is applicable to 1-D objects such as stripes and slits, but it is not applicable to 2-D objects with the arbitrary shapes. Finally, the resolution quantification can be performed by 2-D convolution, the method applicable to objects with the arbitrary shapes [6,20,53,65].

The first method of judging the MRF is still frequently used means to quantify resolution due to its simplicity. The principle is to determine if the feature can be considered as "resolved" based on its appearance in the image and using typically the knowledge about the object which can be characterized by a precise method such as SEM. In this method, the resolution of the optical system is associated with the physical dimension of MRF sizes. This method cannot be viewed as reliable, and, in fact, it often leads to exaggerated resolution claims. A super-resolution of $\sim \lambda/8$ to $\lambda/14$ was claimed by silica microsphere-assisted microscopy [38]. And later even better resolution of $\sim \lambda/17$ was claimed by similar microsphere-assisted scanning laser confocal microscope (SLCM) [204], as shown in Fig. 1.32. Another super-resolution with extremely high value of $\sim \lambda/30$ for microwave was also claimed using such estimation method based on the FFTR [197].

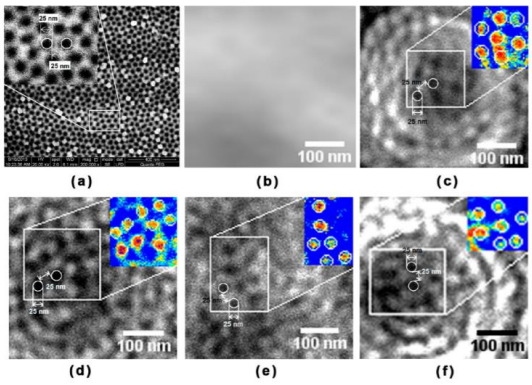

Figure 1.32: Micrographs of the 25 nm AAO template by (a) SEM, (b) standard SLCM, (c) 5 μm diameter FS mSLCM, (d) 2.5 μm diameter FS mSLCM, (e) 7.5 μm diameter FS mSLCM, and (f) 5 μm diameter PS mSLCM, where the insets are the corresponding pseudo color images.[204]

More rigorous methods which provide more accurate estimation of resolution is performing 1-D or 2-D convolution. The image, *I(x,y)*, is a result of convolution of the object, *O(u,v)*, and the diffraction-limited PSF of the imaging system [202], which can be expressed as:

$$I(x,y) = \iint_{-\infty}^{\infty} O(u,v)PSF(u - \frac{x}{M}, v - \frac{y}{M})dudv, \quad (1.4)$$

in which the integration is in object plane, and the coordinates of object plane (x_0,y_0) is linearly related to image plane (x_i,y_i) by the magnification, M as (x_0,y_0) = (x_i/M,y_i/M).

This method is standard in conventional far-field diffracton-limited optics [203]. The application of this methodology for super-resolution quantification in MSI represent an important step in the case of label-free microscopy where very bright point sources are typically not available. It was first applied in 1-D case (case of stripes or slits) in [42]. To develop applications to 2-D objects with arbitrary shapes, a convolution of such objects with 2-D PSF is required that was proposed and realized in [6,20,53,65]. Typically, the image is modeled by convolution with the "perfect" drawn object with a PSF. A series of images is calculated for Gaussian PSFs with various widths. The resolution can be

determined based on the best fit of the calculated image to the experimental image. Based on the Houston resolution criterion, the resolution of the system is associated with the width of thus determined Gaussian PSF providing the best fit to the experimental image. Fig. 1.33 shows a fitting result of experiential images and 2-D convolutional profiles. Using 1-D convolution, a super-resolution on a level of ~λ/4 - λ/7 were claimed [42,201]. Using 2-D convolution, a super-resolution on a level of ~λ/6 - λ/10 were claimed in a broad range of imaging situations where microspheres with different parameters were used at different illumination conditions [6,8,69,205,206]. It is obvious that the 1-D or 2-D convolution provides a more accurate estimation of the resolution based on classical imaging theory compared to semi-quantitative procedure based on MRF visualization. In this dissertation, the 2-D convolution will be applied to the resolution quantification process.

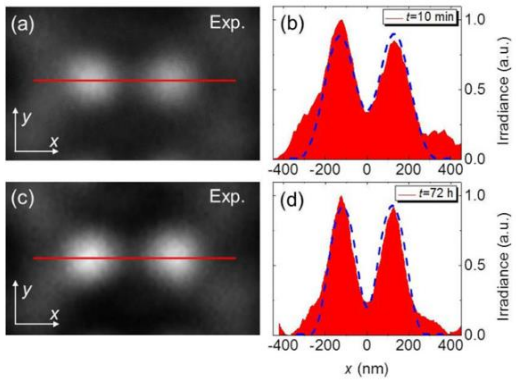

Figure 1.33: (a) Image of an Au dimer obtained through BTG microsphere after 10 minutes of the IPA evaporation. (b) Comparison of the measured (red background) and calculated (dashed blue curves) irradiance profiles through the cross-sectionof the Au dimers (x-axis). (c,d) Same as (a,b), respectively, but after drying for 72 hours. [6]

1.5 Assembling monolayer of microspheres

1.5.1 Techniques for assembling monolayer of microspheres

The main advantage of MSI is its ability to improve the resolution of standard microscopes. However, this method has a drawback related to its limited FoV. In principle, a tightly packed array of microspheres can be deposited on top of the object to image different positions over the large area of object at the same time. Different parts of the object can be seen through different microspheres that can enlarge the FOV of microscopy. Such assembling of microsphere array can also be applied to a completely different application related to developing retroreflectors.

Assembling a monolayer of microspheres can be a difficult task since the microspheres usually have micron-scale dimensions and the large quantities of microspheres need to be packed with the minimal concentration of defects. Currently three major techniques of fabricating monolayer of microspheres are applied: (i) laser-writing-based technologies [207,208], (ii) self-assembly-based technologies [209-214], and (iii) optical tweezers-based technologies [215].

(i) Laser-based technologies. The first method of laser writing is based on the 3-D printing techniques by using laser inscription in photoresist followed by dissolving the unexposed parts. Either the microsphere array itself or the mold with shallow holes which can be used to fabricate microsphere arrays in other materials by injection molding [207,208]. Such method can produce arbitrary shapes. However, the fabrication time and cost are high in the case of massive number of microspheres

(ii) Self-assembly based technologies. The second way of self-assembling of microsphere array is the most-commonly used method to fabricate large-scale microsphere arrays. The principle which is based on evaporating microsphere suspension on well-cleaned substrate is shown in Fig. 1.34 (a) [209]. The substrate is placed vertically inside

a suspension of microsphere distributed unevenly at different heights, or the substrate is placed horizontally, and the suspension is deposited on the substrate by syringe or tube with small aperture. The water in the suspension evaporates and a meniscus is formed due to surface tension. Moving meniscus drags the microspheres and they aggregate into a compactly arranged array or close-packed cluster. Fig. 1.34(b) show the assembled monolayer of microspheres. The uniformity and compact degree of microsphere array is determined by many factors such as the cleanness of substrate, the concentration of the suspension, the material and diameter of the microspheres, etc. Multiple layers were found during assembling due to the shape of meniscus [210]. Assembling results using similar procedures of self-assembling can be found in [211-214]. It should be noted, however, the self-assembly inevitably results in a certain concentration of point-defects, interstitial microspheres and presence of domains with different crystallographic orientation. Somewhat better results can be obtained in the case of patterned substrates, but all these structures are not free from defects and the concentration of defects on the level of several percent is inevitable.

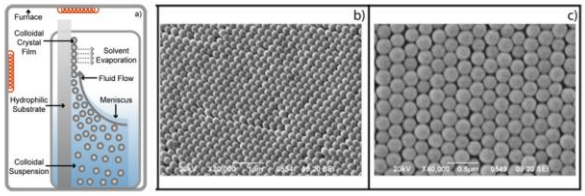

Figure 1.34 (a) Vertical convective self-assembly diagram. (b) and (c) SEM images of assembled monolayer of microspheres. [209]

(iii) optical tweezer-based technologies. The third method uses the trapping of microspheres by the optical tweezers. Multiple optical traps can be created using the optical fiber bundles [215]. The laser is coupled to an objective lens and focused on fiber bundle

with multiple tubes. Each fiber in the bundle is illuminated forming optical tweezer array illustrated in Fig. 1.35(b). The microspheres can be captured from the opposite side of the fiber bundle. Such method can optically trap more than a thousand of microspheres simultaneously. However, the microsphere array can only be trapped under conditions of illumination with a high-power laser beam, and it will be dissolved immediately when turning of the illumination. Such microsphere arrays holding by optical tweezers generated by a bulky and complicated optical setup are inconvenient in further application such as improving resolution of microscopy or building retroreflectors.

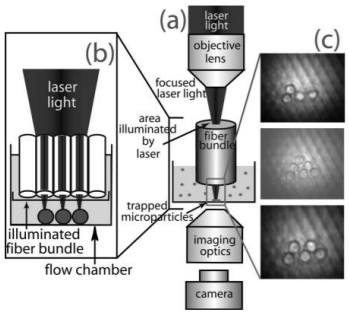

Figure 1.35: (a) Schematic for an imaging fiber-based optical tweezer array system. (b) Region of optical tweezer array system shown in more detail. (c) Consecutive images of trapped 4.5mm silica microspheres. [215]

1.5.2 Retroreflectors

The ordered arrays of microspheres can be used in a different function, namely as retroreflectors. That is why at the end of Introduction Chapter, we will briefly consider basic types of retroreflectors. Unlike mirrors with specular reflection and rough surfaces with scattering in all directions, retroreflectors have the ability to reflect the light back towards the direction of source with minimum scattering for a wide range of incident angle. Such particular property can be applied to road signs, vehicles, and clothing more visible for warning purposes. It can also be installed in space for laser ranging research.

The most commonly used retroreflectors are prismatic retroreflector and spherical lens retroreflector [216]. The prismatic retroreflector consists of three walls each two of which are perpendicular to each other, like the corner of a cube in Fig. 1.40(a). The incident light at an arbitrary angle is reflected twice at two walls of the corner-cube and the reflected beam is parallel to the incident direction.

The second design of retroreflector is built by a dielectric sphere, so-called “cat eye”, with high refractive index of n = 1.8~2.0, as shown in Fig. 1.36(b). Such sphere with high index will focus the incident wave on the shadow surface of the sphere. The light is reflected in an exact backward direction by the back surface of the sphere and propagate in the same direction with the incident beam. In commercial retroreflectors, the back surfaces of the dielectric spheres are usually coated with a layer of metal to increase the intensity of reflection. Characteristically, the prismatic retroreflector has better performance with much brighter reflection and less loss compared to spherical lens retroreflectors, but they are only suitable for narrower range of angle of incidence. The spherical lens retroreflector has worse performance with more loss during retroreflection, but they are still suitable for a larger incident angle [217].

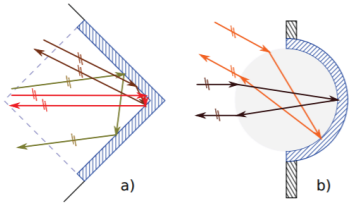

Figure 1.36: Retroreflector: common shapes. a) Corner-cube retroreflector b) Spherical retroreflector (cat’s eye). The sphere is from material with higher refractivity index. [216]

Fabricating the arrays of corner-cube structures in micron scale can be a difficult task since it requires precise 90° angle between three walls and smooth surface quality. Currently, the fabrications were developed mainly by diamond micro chiseling [218] and anisotropic wet etching of Si [219]. Both fabrication procedures are complicated and time consuming. The fabrication of spherical lens array retroreflectors is simpler based on the introduction of achievable methods of assembling monolayer of microsphere array in section 1.5.1. For industry manufacturing, a layer of metal is deposited below the microsphere array to increase the reflection.

Another less common retroreflector is made by phase conjugate mirror based on non-linear optical phenomenon of phase conjugation shown in Fig. 1.37 [220]. The retroreflection behavior is much more accurate compared to cube corner and spherical lens retroreflectors, with the expense of a series of complex and expensive instruments and high incident power. In this case, they are usually used in advanced optical systems.

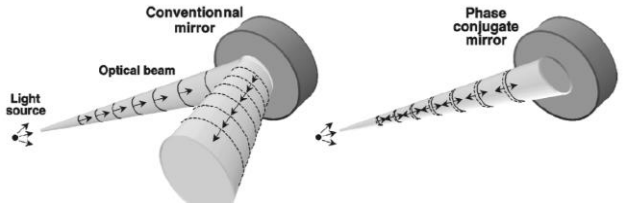

Figure 1.37: Comparison of beam reflection by (a) a conventional mirror and (b) a nonlinear phase conjugate mirror. [220]

1.6 Summary

This dissertation work is devoted to optical properties and potential applications of microconical and microspherical structures with characteristic dimensions on the order of several wavelengths of light which are referred to as mesoscale photonic structures. Their properties are reach, diverse, and some areas are not particularly well studied. As an

example, photonic nanojets are well studied in dielectric microspheres, but relatively poorly studied in structures with the arbitrary shapes such as cubes, cones, pyramids, etc. In this thesis, we plan to study concentration of light by the microcone arrays for concentrating light on pixels of uncooled MWIR FPAs with small photodetector mesa size [221-231]. Potentially interesting properties include their power enhancement factors in comparison with the same structures without microcones that can be used for increasing sensitivity and reducing thermal dark current in the uncooled MWIR FPAs. Other interesting properties of such structures are based on their ability to resonantly trap light which can be used for developing multispectral imaging with narrow bands [221,226,227]. Light concentrating capability do not represent all functions in which mesoscale photonic structures can be used in various novel devices. Due to a larger role of near-field optical phenomena in such structures compared to their enlarged millimeter-scale counterparts, they can be used in super-resolution imaging applications as contact microlenses. The physical mechanisms of microsphere superlens imaging is still debated in the literature. Due to its simplicity and inherently high resolution MSI technology can result in developing novel biomedical applications such as diagnostics of diseases *in vivo* without invasive biopsy.

In Chapter 2 we are aiming to design microconical arrays which can be integrated with the IR imaging sensors such as MWIR and LWIR FPA. It is known that these FPAs operate at temperatures below 100K which requires a cooling system to maintain the high-performance level. A large thermal noise intrinsic for the uncooled FPAs which can be reduced by minimizing the individual photodetector mesa size of FPAs [172]. In this case, the light concentrators can collect light over a wide area and deliver it into smaller

photodetector mesas to maintain the photon collection efficiency for smaller photodetectors and reduce their thermal noise. Previous designs of light concentrators have the problems of either non-feasible manufacturing procedure or limited AoVs [223-225,230,231]. Considering the fact that Si is the major material in microelectronics such as ICs, and the well-established anisotropic wet etching is able to fabricate microconical array on Si substrate [176-178], we propose the design of microconical Si light concentrators integrated with FPAs [221]. We propose three ideas of Si microcone array with different orientation (regular or inverted) designed for different types of FPAs with specific integration and illumination requirements. These include: (i) heterogeneous integration with front-illuminated FPAs made by III-V semiconductors with high QE, and (ii) monolithic integration with back-illuminated FPAs formed by PtSi Schottky-barrier detectors with low QE which requires an enhancement of absorption by resonance build up inside the microcone. The goal of the study is designing Si microconical light concentrators which is feasible for practical fabrication and study their optical performance such as the power enhancing ability and AoV. We use FDTD modeling to study this problem by exact numerical solution of Maxwell equations. Our results can predict the performance of concentrating and power enhancing ability and the AOV for proposed designs, they can also suggest the potential application of multispectral imaging.

In Chapter 3, another design of low-index (n = 1.6) microconical light concentrators heterogeneously integrated with FPAs was proposed. To take advantage of FPAs with high QE properties such as III-V semiconductors or quantum dots [146-163], we study a possibility of using photoresists and thermoplastics with a modest index of refraction about 1.6. Microconical arrays can be fabricated using the laser-writing by Nanoscribe and

injection molding in such materials [222]. The goal is to study the performance of power enhancing ability, AoVs, and provide theoretical explanation of the preliminary experimental testing results performed on similar structures integrated with photodetector FPAs by our collaborators at AFRL. It is shown that the characterization results are in good agreement with the predictions of our theoretical modeling results.

In Chapter 4, we proposed a novel label-free cellphone microscopy assisted by contact ball lens with high index n = 2.02 to achieve a submicron resolution. Previously the microscopy assisted by microspheres in mesoscales have been developed by using microscopes equipped with the best quality objectives to achieve super-resolution [38,39,42]. It is attractive to develop such imaging in combination with cellphone camera without using heavy and bulky microscope stands and expensive objectives. Our goal is to design a compact, low cost, lightweight and user-friendly microscopy with high-resolution (not necessarily super-resolution) which can be used for diagnostics of diseases *in vivo* without invasive biopsy. By using dispersive properties of high-index microspheres in combination with the rigorous methodology of resolution quantification we prove that such cellphone microscopy can achieve label-free imaging with a submicron resolution ~600nm which exceeds previously obtained resolution by almost three times. The limited FoV provided by the individual ball lenses can be enlarged by using suction assembly of microspheres through the microhole arrays.

In Chapter 5, we developed the technology of assembling well-ordered monolayer of microsphere arrays in the microhole arrays. Previously, the assembling of microspheres can be achieved by laser writing, self-assembling via evaporation of microsphere suspension, and trapping by optical tweezers. We show that the forced nature of suction

assembly has many advantages over other known methods. These advantages are especially pronounced for larger ball lenses; however, the proposed technology has a potential to be improved for assembling microspheres with the mesoscale diameters as well. Potentially, high-index ball lenses can be used in a totally different application related to their retroreflection properties. Similar to the super-resolution imaging applications, assembling large-scale arrays can be also useful for such retroreflector applications. The first experiments performed on arrays of microspheres with the index of refraction perfectly tuned in the vicinity of 2 due to their dispersion properties demonstrated their narrow cone retroreflection properties.

CHAPTER 2: MICROCONICAL SILICON MWIR CONCENTRATORS ASSOCIATED WITH FPAS

2.1 Introduction of light concentrators integrated with FPAs

Nonimaging light concentrators, such as compound parabolic concentrators [173] and Köler integrators [174], is important for building efficient solar cells. Since such concentrators are mostly in the scale much larger than one illuminating wavelength (λ), the optical properties of those structures are under the geometrical optics which leads to a fundamental tradeoff between the concentrating factor, C, and the angle-of-view (AOV), θ, in a relation of $C = 1/\sin\theta^2$ [173,174].

The idea of designing concentrators of light on a photodetector mesa with small size can be applied to reduce the large thermal noise of MWIR and LWIR FPAs [143]. Despite the complexity of the cause of formation of thermal noise in photodetectors, in general, the thermal noise level is decreasing when the photodetecting area is reducing. For uncooled thermal imaging devices, the large thermal noise is one of the key factors that limit the imaging quality and the idea of designing concentrators of light is important for improving the performance of such devices. Fig. 2.1(a) shows the traditional FPAs with large photodetector mesa size and compact arrangement. The thermal noise level will be reduced if the individual photodetector pixel size can be reduced and leave blank spaces between the photodetectors for electrical circularity connections.

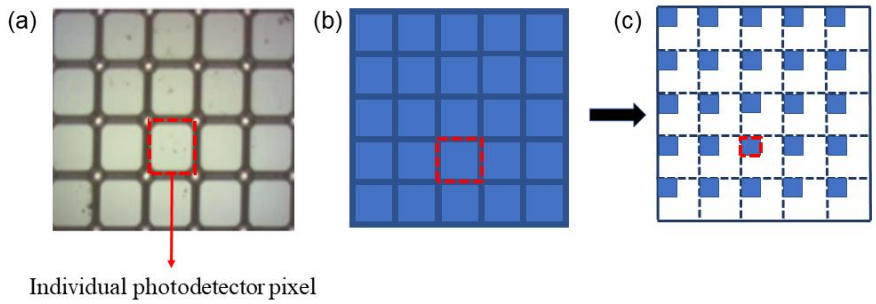

Figure 2.1: (a) Conventional FPAs with large individual photodetector mesa size and compact arrangement. (b) and (c) Illustration of reducing the individual photodetector mesa size and leave blank spaces for electrical circularity connections.

The current limitation of the size for photodetector mesa in MWIR FPAs is approximately ~2.5λ [239,240]. Considering the problems that the area fill-factor will be reduced for photodetector array with smaller mesa size and same pitch, and there will be stronger diffraction of light occurs at the edge of the photodetectors, photodetector mesas are usually designed in a relatively large scale. However, these problems can be solved in principle if a photodetector array can be designed as structures collecting the light from a wider area and delivering it to a compact and narrow photodetector mesa. Till now, the ideas of such structures of collecting and concentrating light are limited into two designs: (i) *macroscale (characteristic dimensions* ~10λ-100λ*) dielectric structures* [223,224,241-245] and (b) *wavelength-scale Si microcone arrays* integrated with Schottky barrier detectors [246,247].

The optical properties of the first design of macroscale dielectric structures are limited by geometrical and/or diffractive optics since the marcoscle structures are much larger than on illuminating wavelength (λ). In this case, they have the optical properties similar to the nonimaging light concentrators for solar cells. In general, they are in the formation of different kinds of lenses, and they can achieve large concentration factors

however sacrificing the AoVs. For example, a metalens with specially designed periodic surface structure was proposed as light concentrator [242]. Fig. 2.2(a) shows the schematic of such light concentrator optical coupled with photodetector mesas of FPA with small size. The metalens collect light over the wide area of the metalens surface and focus it into small and compact spots with a narrow waist of ~10 μm shown in Fig. 2.2(b). The focused spots confine power into small areas which can be detected by photodetector mesas with small sizes. However, such metalens has a long focal length *f* of 155 μm, which will cause a huge lateral shift of the focusing positions even with a slight tilt in the incident angle of light and the focused power will be out of the detecting area. We define the AoV as the angle of the incidence at which the power collected by the detector decreases to half of the maximal at normal incidence. Such designs based on lens arrays such as commercial lens array [143] has very mature fabrication techniques at low cost, but they usually have long focal length larger than 100 μm leading to a bad AoV < 2° which is not applicable for many uses.

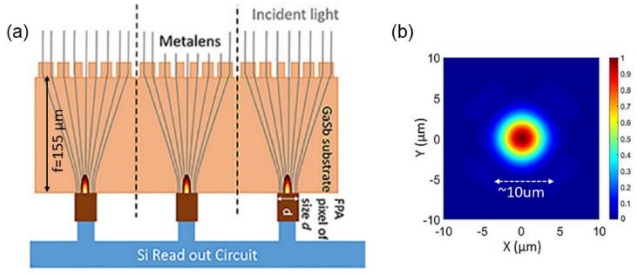

Figure 2.2: (a) Schematic of metalens as light concentratos optically coupled with FPAs with small photodetector mesa size. (b) Power distribution map of the focused beam after passing through metalens. [242]

Concentrating structures with shorter focal length is the key to improve the AoVs. Another proposal was made by assembling a monolayer of microspheres with high refractive index of n = 1.8 shown in Fig. 2.3(a) [223]. Such high index microspheres have a short focal length f around several microns, which allows a huge AoV larger than 20°

when the microspheres are in contact with the front-illuminated photodetector mesas shown in Fig. 2.3(b). A broadband photocurrent gains for MWIR FPAs up to 100 times was claimed for individual photodetector mesa coupled with microspheres above [232]. However, the fabrication the integration of such monolayer of microsphere array with FPA photodetectors can be not feasible in practical considering the difficulty to assemble a single layer of microsphere with massive number and the alignment of individual microsphere with one photodetector mesa. To simplify the integration, new ideas were proposed such as integrated microlenses [241], metalenses [242,245], dielectric microdisk antenna arrays [243], and axilenses [244], unfortunately those designs have worse AoVs than the microsphere array.

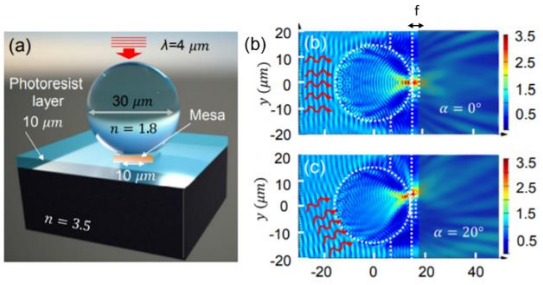

Figure 2.3: (a) Microsphere with high index of n = 1.8 optically coupled with photodetector mesa with 10 μm size. (b) Simulation showing an AoV larger than 20° that still half of the power for normal incidence can be collected by the detector. [223]

Microconical structures is another approach of light concentrating structures since dielectric microcones was reported to show the ability to focus light tightly [248]. However, in practical, the microcones were in very compact scale close to illuminating wavelength and the sidewalls of them were covered with a thin layer of metal. The concentrating ability was actually achieved by the plasmonic adiabatic compression towards the apex of the tip of the microcones [249]. The mechanism of the enhancement of photocurrent for such

structures are complicated and the plasmonic hot spots formed at the top of the microcones which increases the internal photoemission efficiency may be involved in it [246]. An improved performance of Schottky detector over broadband in near-IR regimes was shown over similar detectors with flat barriers when optically coupled with both regular microcone array coated with Al nanofilms [246] and inverted microcones coated with Cu nanofilms [247]. Both designs of microcone array have a scale close to illuminating wavelength, however they are too small to contribute to the photoelectric response by the internal dielectric resonant properties of microcones.

Recently, the technology of anisotropic wet etching of Si allows a simple, low-cost, and parallel fabrication of arrays with large scale and makes the Si microconical array as an interesting approach as light concentrating structures. Different from the previous designs, in this chapter, we are interested in the properties of Si microcone arrays in a mesoscale regime, which means the characteristic dimensions of microcones are several times larger than the illuminating wavelength. Such regime has not been studied for microconical concentrators as far as we know. Microcones with sizes in mesoscale regime are large enough to form resonant modes with high Q-factor. This property shows a tremendous potential of solving a classic problem of photodetectors build in Si due to the small QE at the photon energies below the fundamental absorption edge of Si. It was demonstrated that for resonant devices with high Q-factors such as all-Si spherical Mie-resonators, the IR photons tend to stay in the cavity for a very long period which increases the probability of them to be absorbed [166]. An enhancement of photocurrent response occurred at photon energy below the absorption edge of Si where the absorption coefficient is extremely low.

To study the properties of Si microcone structures as light concentrator, we are using exact numerical solution of Maxwell equations which is also known as finite different time-domain performed by the software of Lumerical to find out if the resonant enhancement of photocurrent response can also happen in Si microcones in mesoscale regime. In this chapter, we are not calculating either the absorption efficiency or the photocurrent response of the devices in practical since a comprehensive and detailed understanding of the structures of specific device with all parameters is required which is far beyond the main purpose of this work. Instead, we are interested in the photon fluxes incident on the larger case of the microcone then transmitted through the photodetectors close to the smaller base of the microcones with a characteristic dimension of 4 μm. The photon fluxes present strongly pronounced spectral peaks because the photons are trapped inside the microcones due to resonance which increase the absorption of photons and potentially increase the QE of photodetectors. Such properties of resonant peaks show a potential application of multispectral imaging through microcones. To measure the enhancing ability of such microcone structures illuminated with plane wave, a parameter called power enhancement factors (PEFs) is defined as the ratio of photon flux collected by the photodetectors when they are equipped with the microcone structures to the photon flux detected by the same photodetector without equipment of microcones. Besides the resonant light concentrating properties due to the resonant trapping of photons inside the microcones, non-resonant light concentrating properties also appear in the microcone causing by the tapering effect on light propagation. It is claimed that such non-resonant light concentrating properties can be obtained in structures with arbitrary shapes when they are in mesoscale [250].

In practical, the shape of the bases of microcones fabricated by anisotropic wet etching can be two different types by changing the experimental fabrication conditions: the rectangular shape, or the octagonal shape [251,252]. To compromise and simplify our numerical analysis, we are designing the microcones with bases in the shape of circles. The angle of the sidewalls of the microcones is determined by the orientation of the Si wafer and photoresist mask and the type of etchant. If the (1,1,0) direction of a square mask is aligned on a (1,0,0) wafer, the sidewalls of the microcones will follow the (1,1,1) crystal planes of Si, causing a sidewall angle of 54.7° to the horizontal direction. We simplify the geometry of microcone structure from real fabrication to a truncated microcone with larger circular base of 14 μm diameter and smaller circular base of 4 μm diameter. In this chapter, we propose three designs of microcone structures integrated with photodetector mesas of FPAs [221]: (i) inverted microcones (light incident on larger base first and transmitted to smaller base) heterogeneously integrated with fromt-illuminated FPAs, (ii) inverted microcones monolithically integrated with metal-Si Schottky barrier photodetectors, and (iii) regular (not inverted) microcones monolithically integrated with near-surface photodetectors. The first design has the advantage of the Si microcone array can be integrated with MWIR FPAs fabricated in different material systems other than Si such as II-VI or III-V semiconductors superlattices, quantum dots, and quantum well photodetectors with the highest efficiency. However, our numerical analysis shows a relatively low PEF<10 and modest AoV<10° for such design. The second design has the advantage of the integration of Si microcones and photodetectors of FPAs can be simplified to pre-fabricate metal-Si Schottky barrier detectors during the etching process of Si microcones. Another advantage of such design is that the resonant trapping of photons is

strongly increased due to the reflectivity of photons on the smaller base of the microcones coated with a thin layer of metal, and a large PEF>20 was observed in our numerical analysis. The most interesting property is the stability of the positions of some PEF spectral peaks without shifting when increasing the angle of incident at two polarizations (TE and TM) leading to a huge AoV>30°. This property is extremely attractive for developing multispectral imaging with ~100nm bands and large AoVs. The third design of regular (not inverted) microcones is to compare the properties of regular and inverted microcones theoretically. Such design of regular microcones show properties similar to single pass contact microlenses. We did not observe any resonant effect, but we found that such design shows a property to focus the incident light into an extremely small photodetector with huge AoVs similar to the high-index microsphere arrays [231].

In section 2.2, we present the geometries of the three designs and the numerical analysis of them. In section 2.3, we present our conclusions.

2.2 Three numerical designs of microcones integrated with FPAs

Anisotropic wet etching of Si has been studied due to its applications in the fabrication of microelectromechanical systems (MEMS) [228]. Such fabrication is capable of fabricating high-quality low-cost Si microcone array with massive number in a short time which is perfect for our purpose. Solutions of TMAH or KOH are frequently exploited for the anisotropic etching process of the exposed (1,1,1) system of planes on Si (1,0,0) substrates [176-178]. Once the (1,1,1) planes are exposed, the higher density of atoms on the surface of (1,1,1) planes are causing a strong reduction of the etch rate of those planes.

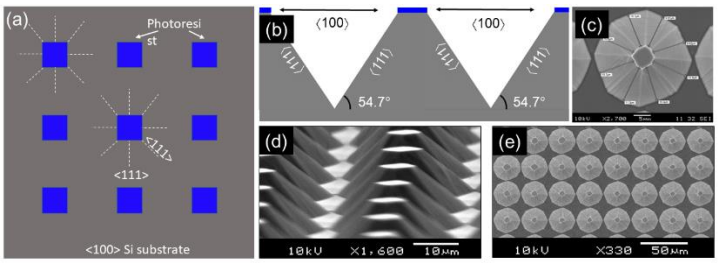

Figure 2.4: (a) Top-view (1,0,0) Si substrate patterned with square shape photoresist array (blue squares). Microcones are fabricated by anisotropic wet etching of Si along (1,1,1) planes (white dashed lines) around each photoresist square. (b) Side-view microcones with (1,1,1) oriented sidewalls, the angle formed by the sidewalls with the surface of the wafer is 54.7°. (c) (d) (e) Top and side SEM pictures of Si microcone array fabricated by anisotropic wet etching performed by Grant Bidney. [253-255]

The often-used microstructure (for passive fiber alignment etc.) is obtained by patterning the (1,0,0) Si substrate with photoresist array in square shape. Fig. 2.4(a) showed the top view of (1,0,0) Si substrate patterned with square shape photoresist array. The solution will etch the Si deep along the (1,1,1) system of planes shown by the white dashed lines around each photoresist square. The etching will be stopped at certain point determined by the designed etching depth and microcones are formed after removing waste during etching. Fig. 2.4(b) showed the side view of microcone array. The sidewalls of microcone are (1,1,1) planes of Si and the angles between the (1,1,1) and (1,0,0) systems of planes are 54.7°. Practical fabrication by anisotropic wet etching of Si microcone array can be found in Ref. [256]. In this work, we are interested in designing Si microcone structure as light concentrator based on such fabrication method with 54.7° sidewall angle to integrate with photo-detecting mesa of FPAs.

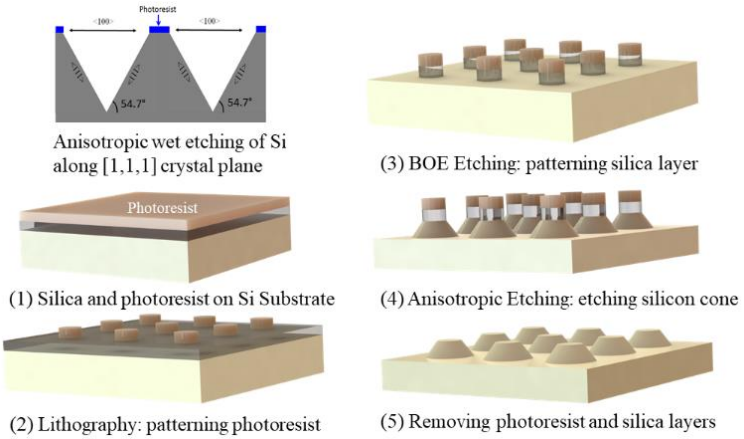

Figure 2.5: Fabrication procedure of Si microcone using anisotropic wet etching we developed in the cleanroom of UNC Charlotte.

Our group also performed the fabrication procedure of Si microcone array with our desirable geometry. The fabrication work is leaded by our group member Grant Bidney, and I joined all the fabrication activities to assist him [253-255]. The fabrication procedure of Si microcone array we developed in our cleanroom is shown in Fig. 2.5. A layer of SiO_2 and a layer of photoresist is deposited on a Si wafer, respectively. A photomask with characteristic dimensions same to the smaller base of designed microcone is in tightly contact with the wafer and pillar array of photoresist will be obtained by lithography. After applying buffered oxide etch (BOE), same pattern of SiO_2 can be obtained. After that a solution of TMAH will etch the Si under SiO_2 and photoresist pattern along (1,1,1) crystal plane and form microconical shape of Si. The etching will be stopped when it is long enough to etch the desired height of the microcone considering the etching speed. After removing the SiO_2 and photoresist layers, regular microcone array (not inverted) on Si substrate can be obtained. For further use, it will be flipped upside down and the smaller base of the microcone will be integrated with FPAs. Detailed information of fabrication will be reported by Grant Bidney in his dissertation.

2.2.1 Inverted microcones heterogeneously integrated with front-illuminated FPAs

We begin with the design of inverted microcones heterogeneously integrated with front-illuminated FPAs. By designing the pitch and size of the photoresist array and controlling the etching time of Si, the Si microconical array can be fabricated with the pitch and size of the tips of the microcones matching the period and size of the photodetector mesa in a front-illuminated FPA, respectively. The heterogeneous integration of the microcone array with the photodetector array in principle can be achieved by an optical alignment using a liquid layer (adhesive or a photoresist) that can be solidified, which would enable slight adjustments of the mutual position of these arrays to maximize the signal collected by the photodetector pixels. Such heterogeneous integration is feasible since only a micron-scale accuracy is needed for the design. An antireflection coating can be applied to the back surface of the Si slab (top surface in Fig. 2.6(a)) into where the light will incident to increase the collecting efficiency.

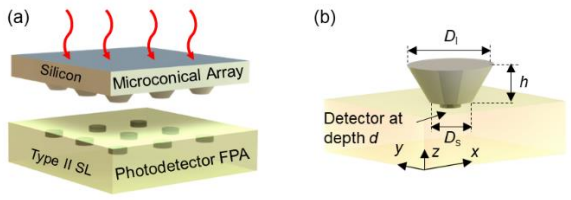

Figure 2.6: (a) Inverted Si microcone array heterogeneously integrated with the front-illuminated FPA exemplified by strained-layer type II superlattice. (b) Simplified theoretical model of individual inverted microcone heterogeneously aligned with one photodetector mesa. [221]

To reduce the reflection loss at the interface between Si and FPA considering the index of Si and FPA are close, the gap between the small tips of the microcones and mesas filled with adhesive, epoxy, or photoresist can be minimized below ~$\lambda/2$ by applying a

gentle pressure. This condition would be well preserved for example in the case of integration with rapidly maturing III–V InAs/In*x*Ga1−*x*Sb strained-layer type II superlattice (T2SL) detectors and quantum well and dot III-V detectors [146-163].

To simplify our theoretical model, the thick Si substrate above the microconical array shown in Fig. 2.6(a) was completely removed and the small base of the microcone was considered to be in contact (without a gap) with the photodetector mesa illustrated in Fig. 2.6(b). A more detailed illustration about the schematic is shown in Fig. 2.7(a). We assumed that the index of the photodetector substrate and Si microcones are the same. Although there will be an index mismatch between the photodetector substrate and Si microcones causing a slight reflection at their interface if the photodetectors are fabricated using III-V semiconductors, the results would be still close to the predictions of our model qualitatively. In our model, we assumed a circular cross-section of microcones with the large top base D_l = 14 µm, small bottom base D_s = 4 µm, and height h=7.07 µm.

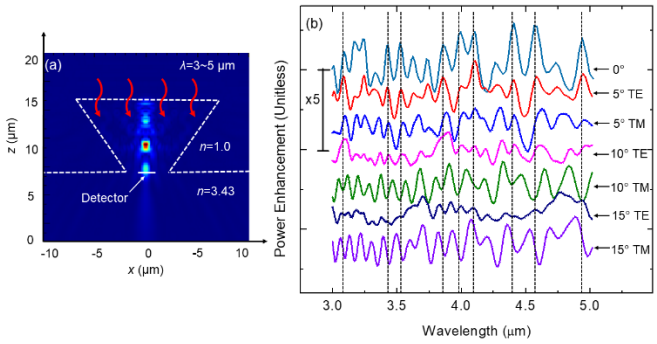

Figure 2.7: (a) EM field distribution calculated at normal incidence for inverted Si microcone with the circular cross-section and with the large base D_l = 14 µm, small base D_s = 4 µm, and height h=7.07 µm. (b) The PEF spectra calculated using a square monitor with the 4 µm side placed 100 nm below the surface of Si substrate (shown as a "Detector" in (a)). [221]

The numerical modeling was performed using 3-D FDTD calculations by Lumerical software for incident plane waves with broad band λ=3~5 µm. A "Transmission"

(T) monitor without causing any perturbing on flux was used to calculate the photon flux passing through the microcone into the detector mesas. A square shape T-monitor with the sides equals to one wavelength (4 μm) was placed 100 nm below the small base of microcone inserted in FPA to measure the potential photo-response of the front-illuminated photodetector.

To estimate the power enhancing and concentrating ability of the microcone, we defined a parameter power enhancement factor (PEF) as the ratio of the photon flux collected by the T-monitor through the microcone to that measured by the same size T-monitor without the microcone above. According to our definition of PEFs, smaller size of T-monitors leads to a progressively larger PEF value. However, we decided to assume the size of monitors to be the same with one wavelength (4 μm) which is the minimal physical dimensions of the photodetector mesas which is feasible by the existing well-established technologies. Even though a much larger PEFs can be achieved by using the subwavelength monitors, we did not analyze such cases in this Section because of the problem of challenging fabrication, alignment, and coupling light in small mesas. The power distribution map for light incident into the microcone and be delivered to monitor is shown in Fig. 2.7(a). A resonance built up inside the microcone due to the bounce on sidewalls caused by large index mismatch between Si and air can be clearly seen and the output of the resonance is delivered to the monitor below the microcone. It should also be noted that the bright spots inside the microcone in Fig. 2.7(a) represent the maxima of constructive interference which do not necessarily represent the maxima of the photon fluxes measured by the T-monitor.

The PEF spectra in a wavelength range between 3μm and 5μm calculated for different angles (α) and polarizations (TE and TM) of incident light are shown in Fig. 2.7(b). The spectra are vertically presented for different α s and polarizations (the scale bar indicating a 5-times enhancement). The key feature of the inverted microcones illustrated in Fig. 2.7(a) is that such structures trap light and build up a resonance due to multiple reflections by their sidewalls. This resonant effect is extremely important which allows developing multispectral imaging. In addition, the resonant enhancement of EM field along the smaller base of the microcone could potentially increase the absorption of photons by the detectors. The PEF peaks have a spectral width ~100 nm. The magnitude of PEF peaks in Fig. 2.7(b) are less than 10× for 4 μm detector, but the resonant PEF's enhancement can be further optimized by varying the dimensions of microcones. The positions of the resonant peaks are determined by the geometry of microcones and increasing the height of the microcones (keeping the same 54.7° angle of the sidewalls) can cause a spectral shift of the PEF peaks and it can also lead to further increase of their *Q*-factors.

An interesting property of inverted microcones is shown in Fig. 2.7(b) related to the incident angular dependence of the enhancement factors. A relatively weak spectral shift of the peak positions is observed with different angle of incidence (α) and polarizations (TE and TM). It is seen that at α = 5° to 15°, the resonant peaks have positions almost identical to that at normal incidence at TE polarization. This property distinguishes such inverted microconical arrays from the traditional multilayer structures where Bragg reflection causes strong polarization-dependent shift of the stop band with the angle of incidence. The fact that in microcones the resonant peaks have a tendency to overlap in a

much wider range of angles and for both polarizations of incident light is related to 3-D nature of trapping light inside the individual microcones.

2.2.2 Inverted microcones monolithically integrated with PtSi Schottky Barrier diodes

Using various material system based MWIR FPAs is favorable considering its high quantum efficiency, and the design introduced in last section allows the integration of such FPAs and Si microconical arrays. However, a nonstandard procedure of alignment with the photodetectors in heterogeneous integration is required. On the other hand, Si-based photodetectors makes it possible to realize monolithic integration of Si microcones with the photodetectors on the same wafer during single lithography process. Fig. 2.8(a) and 2.8(b) shows the geometry of such design and illustrate the advantage of monolithic integration. Indeed, fabricating efficient Si MWIR (or LWIR) photodetectors is a problem considering the low QE of Si detectors.

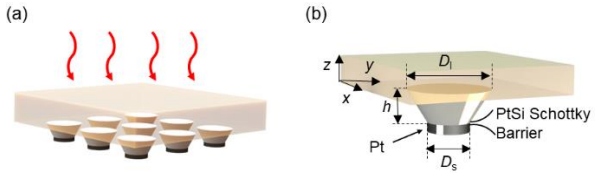

Figure 2.8: (a) Inverted Si microcones monolithically integrated with the metal-Si Schottky photodetectors and (b) Corresponding theoretical model.

Si, as an indirect bandgap semiconductor, can be used as an extrinsic MWIR and LWIR photodetector. The metal silicide/Si Schottky barrier detectors were once proposed to achieve sophisticated readout circuits for photon detection and electronic readout on a Si chip [167]. PtSi detectors are most used in MWIR range. The MWIR radiation is transmitted through the p-type Si and absorbed in the metal PtSi, which produces hot holes and are emitted over the potential barrier into the Si [168-171]. It should be noted that the

QE of such photodetector is usually very limited at ~0.1 level, while many other applications such as the generic NASA Earth and planetary spectral imaging applications require a QE larger than 0.5.

Several methods such as plasmonic resonators, waveguide integrated devices and photonic resonant cavities have been proposed to increase QE by increasing the absorption. A promising way of using NiSi Schottky barrier detectors on n-type Si was proposed since it has a ~600 meV barrier height which is enough for detection in SWIR spectral range and maintains a relatively low dark current density at room temperatures [257,258]. When the thickness of the silicide film is reduced to its percolation threshold, the QE of NiSi Schottky barrier photodetectors can be significantly increased. An even higher QE can be provided using back-illuminated photodetectors with an anti-reflection coating and quarter-wave resonant reflector compared to front-illuminated structures with backside reflector [257,258]. Similar ideas based on PtSi or AuSi Schottky barrier detectors can be applied to MWIR and LWIR ranges to increase the QE.

In our work, we are interested in the electromagnetic field enhancement provided by the Si microcone structure with an additional platinum (Pt) layer on the bottom shown in Fig. 2.9(a). The microcone has a dimension same as that in Fig. 7(a) of $D_l = 14\mu m$, $D_s = 14\mu m$, and $h = 7.07\mu m$, to make comparison between the behavior of Si microcone with and without metallic layer on the bottom. The metallic layer is a standard part in the designing of practical back illuminated metal/Si Schottky barrier detectors. For example, a SiO_2 layer can be deposited between the Cr/Au (5/200nm) mirror and the extremely thin layer of PtSi, AuSi, or NiSi silicide to separate them [257,258]. To simplify our theoretical

model, we removed such spacing layer of SiO_2 and assume a 1μm thickness of Pt mirror is directly deposited on the 4um-size bottom base of Si micrcone.

Fig. 2.9(a) shows an extremely strong EM field enhancement inside the microcone at the position approximately 1μm above the metallic surface due to a combination of strong reflection by the bottom base and the sidewall surfaces of the microcone. The exact position of such enhancement shown by those "hot spots" is determined by the geometry of the microcone. In practical fabrication of such structure, an additional layer of SiO_2 can be introduced between the metallic mirror and PtSi silicide layer to separate them, and the thickness of it can be adjusted to achieve highest field enhancement in the PtSi silicide layer to optimize the absorption of light and QE. However, similar with the case shown in Fig. 2.7(a), the maxima of constructive interference do not necessarily show the highest photon fluxes measured by T-monitors.

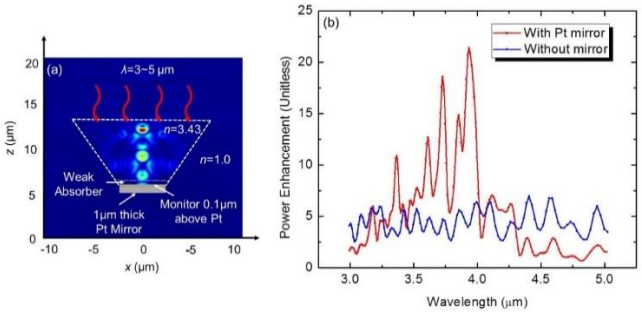

Figure 2.9: (a) EM field distribution calculated at normal incidence on the microcone with the same dimensions as in Fig. 2.7(a), but with a 1 μm thick Pt mirror at the bottom base. (b) Direct comparison of the PEF spectra calculated with (red) and without (blue) Pt mirror using a 4 μm monitor placed 0.1 μm above the bottom base. [221]

The photonic fluxes at the position submicron close to the metallic mirror has been studied and the PEF spectra transmitted through the Si microcone with (red) and without (blue) the metallic layer are shown in Fig. 2.9(b). A T-monitor with 4μm size same to the

bottom base of the microcone was placed 100nm above the bottom of the cone for both cases. We also inserted a slight absorbing layer in our modeling to represent the absorption effect in the depleted layer of real device. The absorbing layer has 1% absorption and 1μm thickness at the lowest 1μm section of microcone. It should be noted that such weak absorption did not significantly change the results.

The comparison of PEF spectra for the cases with and without the metallic layer shown in Fig. 2.9(b) demonstrates a significant resonant enhancement of the photonic fluxes close to the metallic layer. The positions and the total number of the PEF peaks in the same spectral range from 3μm to 5μm are different for microcones with same geometry with and without the metallic layer. It is shown that the intensity of some PEF peaks is increased by several times even up to 20 with the presence of the mirror. It should be noted that such values do not reach the limitation of this design, we can always vary the dimensions of the microcone and reduce the size of the detector to further increase the value of PEF.

Such high resonant enhancement of photon fluxes can be a potential solution of the old problem of Si-based photodetectors related to the low QE at the photon energies blow the fundamental absorption edge of Si. There are peaks in the PEF spectra since the IR photons were confined in the microones and stayed in the cavity for very long times, the possibility of those photons being absorbed is increasing, similar effect has been studied of all-Si spherical Mie-resonators [166]. Such effect can achieve a photocurrent response enhancement in MWIR range (below the absorption edge of Si) with an extremely low absorption coefficient. It should be noted that the monolithic integration of microcones with PtSi Schottky barrier photodetectors can introduce a significant enhancement to the

PEF peaks compared to the similar effects in heterogenous integration without metallic mirror. Such properties show a potential of developing multispectral imaging.

The property is particularly valuable for developing such applications because it also shows a very unusual phenomenon of the positions of these resonant PEF peaks when the angle of the incident is changing shown in Fig. 2.10. It shows that those peaks have a tendency to remain at the same spectral position in a very broad range of incident angle. The most fascinating behavior is that such stability of spectral positions of the peaks in a very broad incident angle range is also true for TE and TM polarization of incident light.

Take the example of the PEF peak at λ = 3.73 μm (red vertical dashed line), it is shown that this peak has a value larger than 10 in the whole incident angle range up to 30° and it stays in the same spectral position for both polarization of light. Similar to the case of microcone structures without metallic mirror on the bottom, such behavior is due to the 3-D nature of confining light inside the microcone structure, which is different from the well-known planar multilayer structures. And our simulation results show a much more pronounced property due to stronger optical confinement inside the microcones with the metallic layer which can be easily fabricated on the bottom of it monolithically integrated with PtSi Schottky barrier photodetectors.

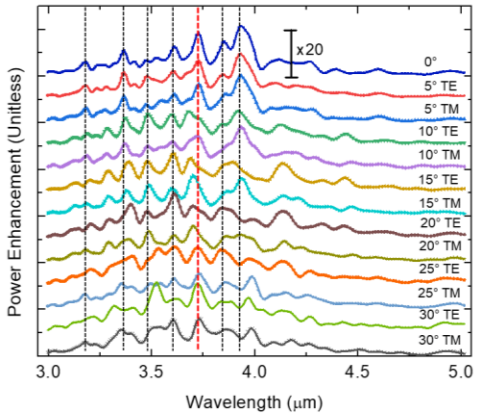

Figure 2.10: The PEF spectra calculated for broad range of angles of incidence in two polarizations (TE and TM) of incident plane waves for a Si microcone containing a metallic mirror at its bottom base. [221]

2.2.3 Regular microcones monolithically integrated with the near-surface detectors

The third case of the integration of microcones with photodetectors is illustrated by regular (not inverted) Si microcones fabricated on the top of near-surface Si detectors shown in Fig. 2.11(a). A nonstandard fabrication procedure is probably also required for such design and discussing about the possible fabrication procedures is out of the range of current simulation work. We decided to assume that the location of the photodetector mesas is inside the near-surface region of the FPA substrate. We made the assumption that the depth (*d*) of the photodetector mesas is below 1μm and center of the mesa and microcone are vertically aligned which is shown in Fig. 2.11(b). In this section, we also assume different sizes of the square photodetectors as 1, 1.5, 2, and 4μm.

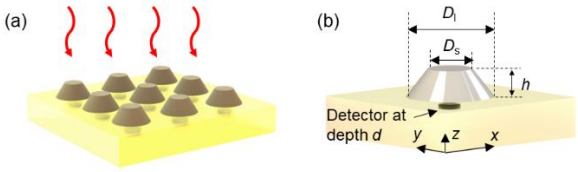

Figure 2.11: (a) Regular Si microcones monolithically integrated with the near-surface detectors. (b) Corresponding theoretical model. [221]

From the prospective of light propagation theory, the regular microcones are very different from the inverted ones since there is no trapping of light inside the regular microcones and the incident light tends to follow the single-pass propagation rule. In this case, the regular microcones show optical properties similar to conventional focusing effect

instead of strong optical resonances and form the “photonic nanojets” similar to light focusing by dielectric microspheres [248].

Fig. 2.12(a-d) illustrated the “photonic nanojets” formed below the microcone represented by the focal point, and it shows how the position of it can be controlled by the height of the microcone when the larger base of the microcone D_l is fixed to be 11μm and the smaller base D_s is reducing. Noted that since the angle of the sidewalls of the microcones is fixed, the reduction of D_s leads to an increase of the height of the microcone.

It is illustrated that different geometry of the microcone can provide focusing on different depths below the microcones and precisely adjustment of the height of the microcone can control the focusing depth. Under the limit of geometrical optics, the focusing position scales with the size of the microcones. A focusing can be even achieved inside the microcone if it is high enough which is not included in Fig. 2.12.

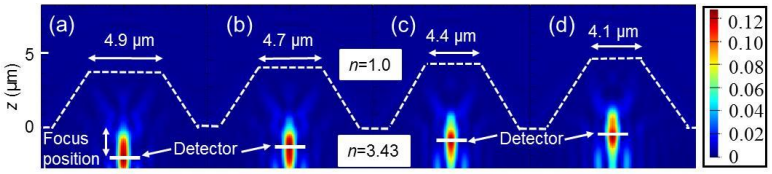

Figure 2.12: (a-d) Photonic nanojets produced by the regular (not inverted) microcones with the bottom base 11 μm and different sizes of the top base: 4.9, 4.7, 4.4, and 4.1 μm, respectively. [221]

The lateral dimension, which can be also called “waist” of the photonic nanojets, are significantly less than one wavelength up to ~$\lambda/(2n)$ level. Such extremely narrowly focused photonic nanojets allows coupling into photodetector mesas with compact sizes. In this section, we use the same definition of PEF to measure the enhancement of regular microcones. Similar to the two previous cases of inverted microcones, the decreasing of

the photodetector mesa size will increase the PEF values since the power collected by the detector without the microcone is proportional to the size of the photodetector.

Fig. 2.13 shows the PEF values calculated at different angle of incidence. In Fig. 2.13(a), at normal incidence, the power of photonic nanojet can be completely collected by the smallest photodetector with 1 μm size since the photonic nanojet is so narrow. When the angle of incidence is increasing, the location of the focal point starts to shift from the center. Fig. 2.13(b) shows that even for a large angle of incident of 40°, the location of the focal point only slightly shifted, and a large portion of the power can still be collected by the 1.5μm photodetector. Fig. 2.13(c) shows the power collected by 1.0 and 1.5μm photodetectors when changing the angle of the incidence for different geometry of microcones.

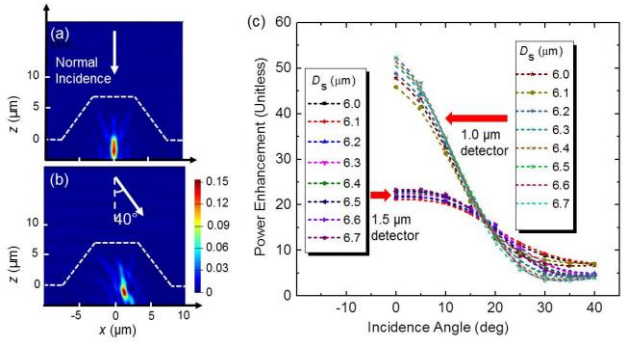

Figure 2.13: Photonic nanojets for microcones with D_l =15 μm calculated for plane waves incident (a) at normal incidence and (b) at 40°. (c) Power enhancement factors calculated for 1.0 and 1.5 μm detectors as a function of angle of incidence for microcones with the same D_l =15 μm and a range of parameters D_s indicated in the legend. [221]

It is seen that there is a tradeoff between the PEFs and AoVs for such structures, and a larger PEF can be achieved by sacrificing the AoVs for smaller photodetectors. For photodetectors larger than 2μm, the PEF can still exceed 10 at normal incidence and the AoV can reach 30°. Such properties can be interesting for applications, but in practice, it

requires further development of technology to realize the monolithic integration of such regular microcones with the photodetectors.

2.3 Conclusions

The development of MWIR and LWIR thermal imaging devices applied in many areas is required to be smaller in size, lighter in weight, energy saving, and lower cost compared to the conventional bulky and extremely expensive MWIR cameras equipped with cryogenically cooling system. The uncooled LWIR cameras can achieve the missions above, but such microbolometer-based imaging devices are suffering from insufficient sensitivity. Recently, a new approach of reducing the thermal noise of MWIR FPAs is proposed by high operating temperature (HOT) technology based on T2SL emerged. However, an operating temperature cooled down to roughly T=130K is still required.

In this chapter, we proposed a photonics approach to solve the problem of reducing the large thermal noise of FPAs by integrating with Si microconical concentrators of light. The idea is to reduce the individual photodetector mesa size of FPAs which will reduce the thermal noise level of photodetectors and in the meanwhile keep a high efficiency of photons collection by the photodetector mesas with smaller sizes. The Si microconical array structures can be fabricated in a massive number by anisotropic wet etching of Si for integration with FPAs in MWIR and LWIR region.

We performed the numerical analysis of three different kinds of designs of microconical concentrators integrated with MWIR FPAs. The first design (Fig. 2.6) is an inverted Si microcone array heterogeneously integrated with front-illuminated FPAs. This design has a main advantage of allowing integrating the Si microcone array with the most

efficient MWIR FPAs made by T2SL with high QE or other material system. It should be noted that the optical alignment of microcones with photodetectos in heterogeneous integration is still a problem, but in practical, an alignment accuracy only in micron scale is required which seems to be feasible. The power enhancement spectra of such design showed resonant peaks in our numerical modeling results which indicates an application of multispectral imaging with a modest AoV up to 10°.

The second design (Fig. 2.8) is an inverted microcone concentrator array monolithically integrated with back-illuminated PtSi or AuSi Schottky barrier photodiode arrays. This design has the advantage of a minimal coupling losses in such structures due to the achievable perfect alignment between the microcones and the photodetectors during a single procedure of lithography. However, MWIR and LWIR Si photodetectors with small quantum efficiency have to be used in such design. An interesting numerical result indicates a strong resonant trapping of photons inside the microcones assisted with the strong reflection by the thin layer of metal on the bottom base of microcone, which could significantly increase the absorption of photons and therefore increase the QE of the Si photodetectors. It is shown that such design could achieve an enhancement factor PEF>20. We also found a fascinating phenomenon that the spectral peaks have the tendency to be fixed at certain positions at a broad range of angle of incident light up to 30° in both polarizations (TE and TM). It is illustrated that the resonant properties of such design can be applied to the area of multispectral imaging with ~100nm bands.

The third design (Fig. 2.11) is the regular (not inverted) microcone array monolithically integrated with the near-surface photodetectors of FPAs. Such design is capable of focusing light into an extremely narrow and compact photodetector mesa, which

is similar to the phenomenon of photonic nanojets formed by light passing through high-index dielectric microspheres. Such design is also capable of achieving very large PEFS and AoVs, but in practical, the feasibility of fabricating such approach considering the heterogeneous integration and alignment of microcone structures and photodetectors is still a problem.

Finally, the numerical modeling studies performed for the three designs above gave a guidance on the fabrication efforts of microcone array by anisotropic wet etching and integration of microcone array with different types of FPAs. This work is mainly performed by Grant Bidney and we are interested in the fabrication results of the three designs and the corresponding testing results of the optical properties.

CHAPTER 3: MICROCONICAL LOW-INDEX PHOTORESIST MWIR CONCENTRATORS ASSOCIATED WITH FPAS

3.1 Introduction of designs of MWIR light concentrators

As introduced in chapter 2, nonimaging light concentrators, such as compound parabolic concentrators [173] and Köler integrators [174], is important for building efficient solar cells. With the scale of such concentrators mostly larger than one illuminating wavelength (λ), the optical properties of those structures are under the geometrical optics which leads to a fundamental tradeoff between the concentrating factor, C, and the AoV, θ, in a relation of $C = 1/\sin\theta^2$ [173,174].

Similar idea of designing concentrators of light and integrated with a photodetector mesa with small size can be used to solve the problem of the large thermal noise level of MWIR and LWIR FPAs [143]. In general, the thermal noise level can be reduced by decreasing the individual photodetector mesa size of FPAs [172]. The idea of developing light concentrators is very important to reduce the photodetector mesa size of FPAs and therefore potentially lower the thermal noise level and improve the sensitivity, SNR, and imaging quality [143,240] for building compact and inexpensive thermal imaging devices without the bulky and expensive cryogenic cooling system.

The development of the designs of light concentrators has been introduced detailly in Chapter 2. To briefly cover it again, the ideas are limited into two directions: light concentrators based on lens-shaped structures with mature fabrication techniques but long

focal length (f). And light concentrators based on spherical lenses with sharp focusing due to shorter focal length but low feasibility in massive fabrication.

Using commercial microlens arrays as the light concentrators is a typical example of the first direction which is integrated with IR photodetector FPAs to increase the sensitivity of the pixels. Since it is true for may photodetectors that the larger photodetector area leads to a larger noise level [143], sharp, narrow spots of power can be focused by the microlens and be totally collected by photodetectors with small mesa size which consequently reduce the thermal noise of photodetectors. However, due to the long focal lengths (f) of most of the microlenses larger than 100μm, a huge lateral shift of the focusing position on the photodetectors will occur when the angle of the incident (α) is slightly tilted, and the relationship can be expressed as: $\alpha < \arctan(d/2f)$, where d is the characteristic photodetector mesa size. The AoV of imaging devices is one of the most important parameters to evaluate the performance, and such commercial microlens array as light concentrators for FPAs has a limited AoV< 2° [242].

Another direction of designing light concentrators is using high-index ($n \sim 1.8$) contact dielectric microspheres with a much shorter focal length (f) within several microns to provide sharp focusing of light on photodetector mesas [223]. Such short focal length allows the position of the focused beam still be in the photodetector area even at a large angle of incidence α up to 20°. However, considering the difficulties of assembling of a monolayer of small microspheres with massive number and the alignment of the center of each microsphere and photodetector mesa, the feasibility of such design is questionable. Other ideas of light concentrators such as integrated microlenses [241], metalenses [242,245], dielectric microdisk antenna arrays [243], and axilenses [244] with much

feasible technology for integration with FPAs were proposed, however the AOVs of those designs are rather limited.

Curved FPAs were proposed to be integrated with light concentrators to increase the AoVs [259,260]. Flexible adiabatically tapered waveguides were also proposed to be integrated with FPAs to increase the AoVs [261,262]. However, in practical, it is rather difficult to realize either idea.

In practical, an approach of light concentrators with a more feasible fabrication method and integration techniques with FPAs is desired [250]. Based on this situation, we proposed the idea of building high-index (n ~ 3.5) Si microconical array as light concentrators integrated with FPAs [221] based on the well-established fabrication technology of anisotropic wet etching of Si [176-178]. The designs and numerical analysis were detailly discussed in chapter, in order to summarize up things, we proposed three different ideas of microconical Si structures as light concentrators:

The first design is an inverted Si microcone array heterogeneously integrated with front-illuminated FPAs. A parameter called power enhancement factors (PEFs) to measure the enhancing ability of light concentrators is defined as the ratio of photon flux collected by the photodetectors when they are equipped with the microcone structures to the photon flux detected by the same photodetector without equipment of microcones. The power enhancement spectra indicated an application of multispectral imaging with a modest AoV up to 10° with a modest PEF value <10.

The second design is an inverted microcone concentrator array monolithically integrated with back-illuminated PtSi or AuSi Schottky barrier photodiode arrays. An enhancement factor PEF>20 and a fascinating phenomenon that the spectral peaks have

the tendency to be fixed at certain positions at a broad range of angle of incident light up to 30° in both polarizations (TE and TM) were observed. Such design can be applied to the area of multispectral imaging with ~100m bands.

The third design is the regular (not inverted) microcone array monolithically integrated with the near-surface photodetectors of FPAs. Such design is capable of achieving very large PEFS and AoVs, but in practical, the feasibility of fabricating such approach considering the heterogeneous integration and alignment of microcone structures and photodetectors is still a problem.

In previous work of Chapter 2, huge AoVs >30° with the extreme interesting application of multispectral imaging with narrow bands due to the unique resonant effect built up inside high-index microcone structures can be achieved. However, all of the three ideas provide a relatively modest PEF up to 20 times. We are interested in further develop such microconical light concentrators using other materials to achieve even higher PEFs while maintaining the AoVs at a high level which also has a mature technology of fabrication in massive number and easy integration with FPAs.

In this work, we propose a new approach of dielectric inverted microcone array with a relatively low index of $n \sim 1.6$, which is the typical refractive index of photoresist or plastic, allowing mature fabrication techniques by commercial products or in industry [222]. Fig. 3.1(a-d) shows the fabrication procedure of the inverted microcone array in photoresist by a commercial micron-scale 3-D printing machine called Nanoscribe. The geometry of the microcone structures and the period of the array can be designed in software and a focused laser beam will write the designed structure on the photoresist droplet deposited on the FPAs by scanning. Since the location of each microcone is

accurately designed by the software, it can achieve perfect alignment of the bottom of microcone with the FPA photodetector. This method in principle allows arbitrary designs of the structures with good fabrication accuracy, however the fabrication time is relatively long for writing an array of the microcones which is not favorable in industry.

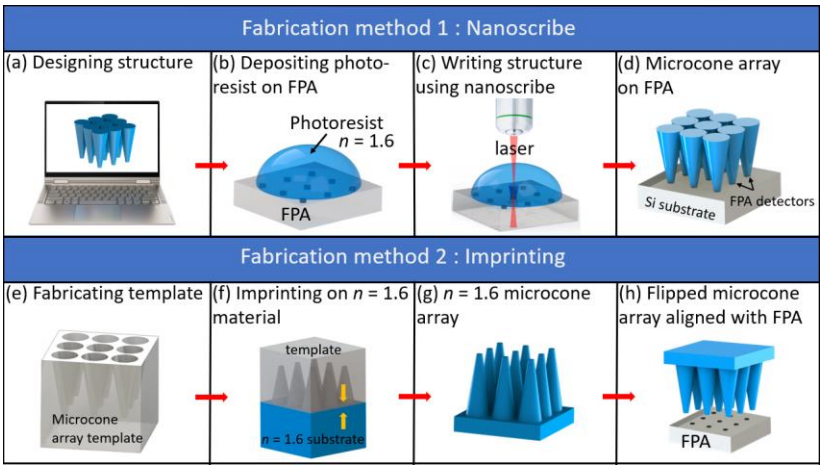

Figure 3.1: (a-d) Fabrication procedure of inverted microcone array in photoresist by Nanoscribe. (e-h) Fabrication procedure of inverted microcone array in plastic by injection molding.

Another fabrication method of injection molding of microcone array in plastic is shown in Fig. 3.1(e-h). A mold with the shape of designed microcone array can be designed with multiple uses, and softened plastic can be injected into the mold and a microcone array in plastic can be obtained. Such fabrication method allows fast fabrication of microcone array with massive number by using a small budget in industry. It should be noted that such fabrication requires a heterogeneous integration of the microcone array with MWIR FPA photodetectors which is another problem in practical fabrication introduced in Chapter 2.

With the two proposals of fabrication methods of dielectric inverted microcone array in practical, we are interested in the optical properties of such microcone array in MWIR spectral region. The purpose of this work is same to that in Chapter 2, which is to

illustrate the enhancing ability of light collected by the photodetector mesas of FPA when equipped with microconical structures over the same photodetectors without any microcones coupled. We are not studying the thermal noise level of FPA is this work.

In this chapter, we perform an extensive full-wave numerical simulation of the optical properties of such low-index (n = 1.6) inverted microcones by varying the geometry of them in a broad range: bottom base diameter $\lambda/2 \leq D_b \leq 2\lambda$, sidewall angle $5° \leq \theta \leq 30°$, and the height of the microcone $10 \leq h \leq 150$ μm, for λ=4 μm which is the center of MWIR spectral range [222]. Our simulation analysis shows no obvious resonant trapping of photons causing PEF spectral peaks inside the low-index (n = 1.6) microcones, which presents the performance similar to adiabatically tapered fiber instead of resonators like high-index (n ~ 3.5) Si microcones [222]. A predicted maximal PEF ~100 in 3-D model is shown in the simulation for microcones with $h \geq 120$ μm, $\theta \leq 10°$, and $D_b \leq \lambda$. To verify the theoretical performance with real fabrication, microcone array with the optimal geometry were fabricated by Nanoscribe with a certain level of imperfection on top of the front-illuminated short-wave IR Ni/Si Schottky barrier photodetector FPA. A three-time enhancement of photocurrent response was observed.

3.2 Numerical design of low-index (n = 1.6) microcones

The schematic design of the dielectric light-concentrating microcone structure is illustrated in Fig. 3.2. The microcone is inverted with its larger base on top and smaller base on the bottom optically coupled with a photodetector mesa. The photons of the incident MWIR light are collected by the wider top base of the microcone and be delivered to the narrower bottom base. We are defining the same parameter of PEF as in Chapter 2

that PEF = P_{cone} / P_0, where P_{cone} is the power measured by the detector equipped with microcone, and P_0 is the power measure by the same photodetector without microcone above. The microcone as four parameters to describe the geometry: top base diameter D_t, bottom base diameter D_b, the height h, and the angle of the sidewalls θ.

Without the optical losses, the value of PEF is limited by the geometry of the microcone as $(D_t / D_b)^2$. However, in practical, only the paraxial rays which are experiencing no or single reflection on the sidewalls will reach the bottom of the microcone with minimal losses providing a PEF larger than 1 shown in Fig. 3.3(a). Fig. 3.3(b) shows the complicated scenario of events for off-axis rays. They can either reach the bottom of the microcone and collected by the photodetector to increase the PEF by multiple internal reflections on the sidewalls or be scattered out of the microcone (and partically retroreflected) after multiple reflections or refractions on the sidewalls. The scenarios are dependent on the geometry of the microcones, and it is especially interesting of studying the dependence of properties on geometry of microcones in mesaoscale regime ($D_b \sim \lambda$, where λ is the wavelength) since the ray optics is not applicable in this regime and a full wave simulation is required.

Therefore, in this work, we study the performance of the PEF of the low-index (n = 1.6) microcone structures with different geometry by an extensive full-wave numerical simulation by FDTD calculations by Lumerical software. The MWIR plane wave in a range of $3 \leq \lambda \leq 5$ μm is incident on the top base if the microcone with index n = 1.6 at an incident angle α and be delivered to the semiconductor substrate with n=3.43, representing the index of Si at λ=4 μm.

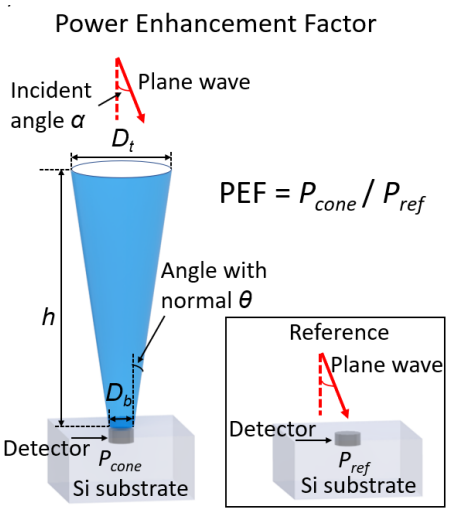

Figure 3.2 The schematic of inverted microcone structure integrated with photodetector mesa of FPAs and the definition of power enhancement factor. [222]

There are four parameters that determine the geometry of microcone, and if the three of them are assigned to a certain value, the value of the fourth parameter is automatically settled. In our work, we vary the bottom base diameter D_b, the height h, and the angle of the sidewalls θ in a broad range: $10 \leq h \leq 150$ μm, $5° \leq \theta \leq 30°$, $\lambda/2 \leq D_b \leq 2\lambda$ in MWIR spectral range with a central wavelength of λ=4 μm. The photon flux is measured by the "transmission" (T) monitor we used in Chapter 2 with the same size of D_b buried inside the Si substrate located at 100nm below the bottom of the microcone. Our results can be also applied to other different FPAs with the index values close to Si such as InAs/$In_xGa_{1-x}Sb$ T2SL as well as III-V QE and QD semiconductor structures [146-163].

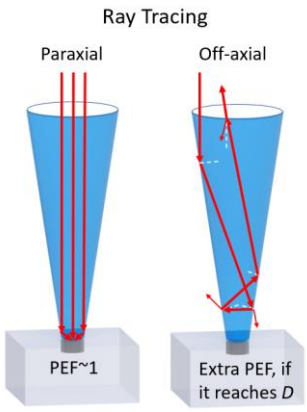

Figure 3.3: (a) Paraxial ray tracing propagating through the microcone. (b) Off-axis ray tracing propagating through the microcone. [222]

Since the geometry of microcones are varying in a broad range reaching h~40λ and D_t~20λ, it requires significant computational time and resources in 3-D calculation. In this case, we performed 2-D simulation for most of the analysis. The 2-D and 2-D models are relevant by the rotation symmetry that at any axial cross-section of microcones, the traces of meridional rays are similar. It is safe to conclude that the value of PEF calculated in 3-D is close to the square of that calculated in 2-D, $(PEF_{2\text{-}D})^2 \approx PEF_{3\text{-}D}$.

To verify the hypothesis in the mesoscale wave optics, we calculated the $PEF_{3\text{-}D}$ spectra (Fig. 3.4(a)) and $(PEF_{2\text{-}D})^2$ spectra (Fig. 3.4(b)) at the cross-sections of the microcones with several random sets of values of D_b, h, and θ at normal incidence and compare them to seek some similarities. It is seen that for smallest D_b = 2μm, the maximal values of $PEF_{3\text{-}D}$ and $(PEF_{2\text{-}D})^2$ are comparable in a ~30-60 range. The photodetector is in square and linear shape with the same size D_b for both 3-D and 2-D cases, respectively. In this case, we are performing 2-D calculations for the following analysis to simplify the simulation and save computational time and use the square of $PEF_{2\text{-}D}$ to roughly estimate the value of $PEF_{3\text{-}D}$.

The properties we are mostly interested in such low-index (n = 1.6) microcones is if it can show resonance performance inside the microcone similar to the high-index Si microcone introduced in Chapter 2. Fig. 3.4(c) shows the $PEF_{2\text{-}D}$ spectra in the $3 \leq \lambda \leq 5$ μm range with some random combinations of values of D_b, h, and θ which cover the whole range of interest and it is illustrated that the variations of the spectra are relatively small (within ~10%). In this case, the low-index (n = 1.6) microcones show different properties from the high-index (n = 3.43) microcones which present marked resonant PEF spectral peaks [222]. Considering the lack of strong peaks in the $PEF_{2\text{-}D}$ spectra, we decide to simplify our analysis for the following studies by performing the simulation at the central wavelength of MWIR range at λ=4 μm instead of calculating the whole spectra.

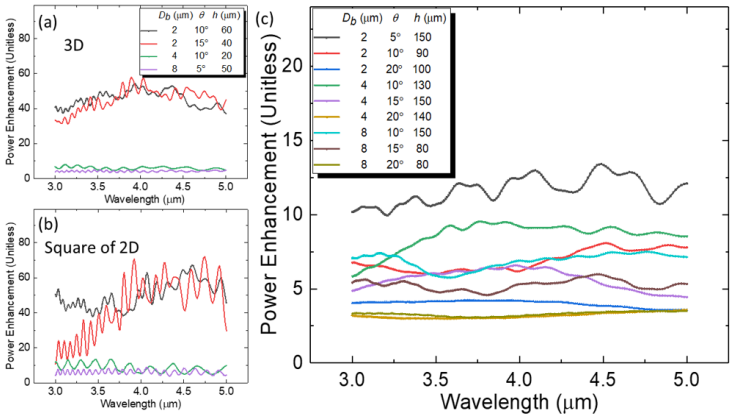

Figure 3.4: (a) $PEF_{3\text{-}D}$ spectra at $\alpha = 0°$. (b) Spectra of corresponding $(PEF_{2\text{-}D})^2$ values. (c) $PEF_{2\text{-}D}$ spectra calculated in a broad range of parameters D_b, θ, and h for 2-D model. [222]

The 2-D simulation results of propagation of plane waves with λ=4 μm at normal incident ($\alpha = 0°$) through low-index (n = 1.6) microcones with a broad variation range of h, θ, and D_b are shown in Fig. 3.4. Fig. 4(a-c) are the EM field distribution maps for plane wave propagate through microcones with h = 100 μm, θ = 10°, and D_b = 2, 4, and 8 μm, respectively. It is illustrated that the wave passing through the microcone and being

delivered to the photodetector has the tendency to be focused into a photonics-nanojet-shaped beam with a narrow width in submicron scale. A linear T-monitor for 2-D modeling with the length same to D_b is placed inside the Si substrate with an index of 3.43 at λ=4 μm approximately 100nm below the bottom base of the microcone to measure the transmitted power.

Fig. 3.5(d-f) shows the calculated $PEF_{2\text{-}D}$ when varying the geometry of the microcone for $10 \leq h \leq 150$ μm, $5° \leq \theta \leq 30°$ and D_b = 2, 4, and 8 μm, respectively. It is shown that when the sidewall angle is small as θ = 5° (and for some cases with θ = 10°), the $PEF_{2\text{-}D}$ values are monotonously increasing with the height. However, when the sidewall angle is larger as $15° \leq \theta \leq 30°$, the $PEF_{2\text{-}D}$ has the tendency to saturation regardless of the increasing of height. It is indicated that only the power in the central region of the wavefront of the incident plane waves can be collected by the detector. It is coincident with the scenario shown in Fig. 3.3(a) that only the paraxial rays confined in an area close to D_b can be directly collected by the detector to increase the PEF.

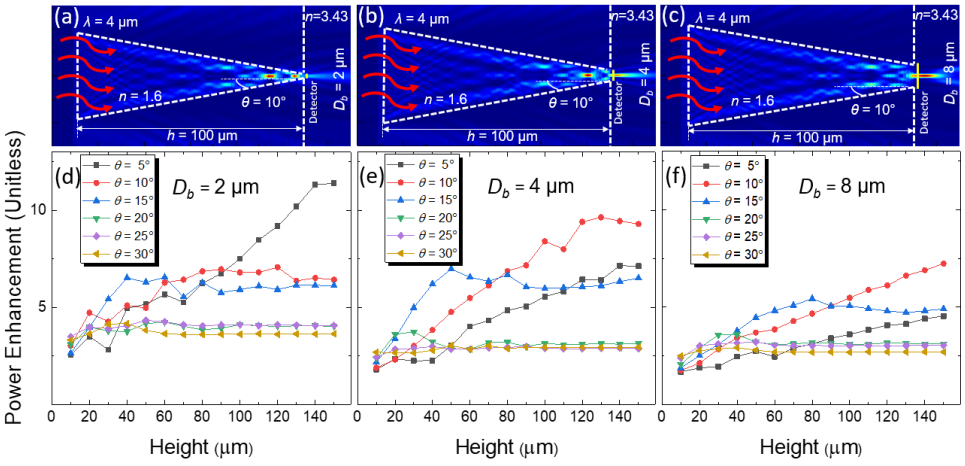

Figure 3.5: (a-c) EM field distributions calculated at normal incidence on the top base of the microcones with index n = 1.6, sidewall angle θ = 10°, and height h = 100 μm placed on top of a high-index (n = 3.43) substrate at a wavelength λ = 4 μm for different sizes of the microcone's bottom base, D_b = 2, 4, 8 μm, respectively. (d-f) $PEF_{2\text{-}D}$ spectra calculated as a function

of the microcone height, $0 \leq h \leq 150$ μm, for a range of microcone angles, $0° \leq \theta \leq 30°$, with D_b = 2, 4, 8 μm, respectively. [222]

For the geometry of microcone with a narrowest bottom D_b = 2 μm, a smallest sidewall angle θ = 5°, and a longest height h = 150 μm, a maximal $PEF_{2\text{-}D}$ of ~12 can be achieved, allowing a predicted $PEF_{3\text{-}D}$ of ~144 corresponding to the square of 12, shown in Fig. 3.5(d). For larger D_b = 4 μm and θ = 10° when height is still tall enough as $120 \leq h \leq 150$ μm, the $PEF_{2\text{-}D}$ still maintains at a high level up to ~10, allowing a predicted $PEF_{3\text{-}D}$ up to ~100 shown in Fig. 3.5(e). In practical, the most feasible geometry of microcone for fabrication is D_b = 8 μm with θ = 10° and h = 150 μm, and it can provide a maximal $PEF_{2\text{-}D}$ = 7.2 which allows a predicted $PEF_{3\text{-}D}$ ~50 shown in Fig. 3.5(f).

Another important property of interest of such microconical light concentrators is their AoVs. As we discussed in Chapter 2, when the incident angle (α) is increasing, the propagation losses inside the microcone is also increasing, also the focused beam with photonic-nanojet-shaped will be shifted towards the edge of the photodetectors causing a reduction of measured power by the detector [221].

The AoVs of the low-index (n = 1.6) with a broad variation range of h, θ, and D_b at λ=4 μm is illustrated in Fig. 3.6. Fig. 6(a-c) are the EM field distribution maps for plane wave propagate through microcones with h = 100 μm, θ = 10°, and D_b = 8 μm when the angle of incident α = 0°, 10°, and 20°, respectively. Although the redistribution of field seems dramatic when α is increasing, the calculated $PEF_{2\text{-}D}$ by integrating of the photon flux collected over the whole length (D_b) of the monitor is monotonously decreasing except for one case in Fig. 3.6(d).

Fig. 3.6(d-f) show the calculated $PEF_{2\text{-}D}$ for increasing the angle of incident (α) at two polarizations (TE and TM) of incident light through the microcone with h =50, 100, and 150 μm, θ = 10° and D_b = 2, 4, and 8 μm, respectively. The AoV is defined as the incident angle at which the $PEF_{2\text{-}D}$ decreases to the half of the maximal value of $PEF_{2\text{-}D}$ at normal incident [263]. However, there is an unusual case for D_b = 2 μm that a maximal $PEF_{2\text{-}D}$ was found at α = 5° for all heights instead of at the normal incident in our calculation shown in Fig. 3.6(d). For both the cases of D_b = 4 μm shown in Fig. 3.6(e) and D_b = 8 μm shown in Fig. 3.6(f), the maximal $PEF_{2\text{-}D}$ were found at the normal incident with an AoV of 12.5° and 15°, respectively.

In general, the calculated results show a tradeoff between the maximally achievable $PEF_{2\text{-}D}$ and AoV when varying the value of D_b [263]. It turns out a larger photodetector (D_b = 8 μm) tends to allow a wider AoV, with a lower $PEF_{2\text{-}D}$ at normal incidence.

Our experimental goals were to fabricate the microcone array with the geometry corresponds to numerical modeling, realize the integration of the bottom bases of microcone array with FPAs photodetectors in MWIR region, and verify their ability to introduce enhancement of the photoresponse of the detectors with small sizes same to the bottom base of the microcone [230]. To realize the integration of microcone array, a front-illuminated MWIR FPAs with small photodetector mesa sizes of 2, 4, and 8 μm and sufficiently large pitch as $D_t/D_b >> 1$ is required. To achieve this goal, a technology of metal silicide/Si Schottky barrier detectors has been used to implement the circuits for both photon detection and electronic readout on a Si chip [167] even though it has a reduced QE in indirect bandgap semiconductors.

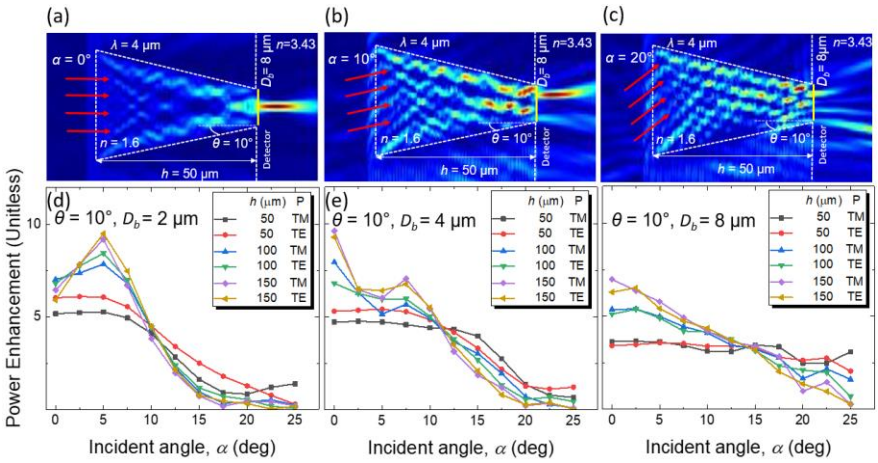

Figure 3.6: (a-c) EM field distributions calculated for microcone with D_b = 8 μm and h = 50 μm at different angles of incidence, α = 0°, 10°, and 20°, respectively. (d-f) $PEF_{2\text{-}D}$ values calculated as a function of α in two polarizations (TE and TM) of incident light for microcones with different heights and θ = 10° and with D_b = 2, 4, and 8 μm, respectively. [222]

The fabrication and testing of microcone array and front-illuminated FPA and the testing after integration has been done before my numerical modeling study. Those results were not published because of lacking the corresponding theory to explain it. I was assigned to the task of helping to interpret the experimental work after I joined the group. With my numerical modeling study, the experimental work can be explained, and I am going to show these results on behalf of our previous group member and collaborators.

We asked Dr. Josh Duran at the AFRL to help us fabricate the front-illuminated Ni/Si Schottky barrier photodetector FPA with an operating wavelength in SWIR spectral range [257,258]. The pitch of the photodetector array is set to be 60 μm while there are several different photodetector mesa sizes: (a) full fill factor with 58 μm aperture, and (b) 22 μm aperture. Several 10×10 arrays of photodetectors were arranged on the same die bonded to a fanout. To simplify the fabrication and testing, all the photodetectors were electrically connected in parallel inside each array.

The fabrication procedure is done by our previous group member Dr. Aaron Brettin by using Nanoscribe. The only feasible size of the bottom base of microcone for manufacture by Nanoscribe is D_b = 8 μm, so we are aiming to fabricate the microcone array with the geometry of D_b = 8 μm, h=150 μm, θ = 10°, and D_t=60 μm, providing a marked $PEF_{2\text{-}D}$ = 7.2, shown in Fig. 3.5(f) and Fig. 3.6(f). They were fabricated on top of the photodetector FPAs with 22 μm aperture.

The first step of fabricating microcone array using Nanoscribe is depositing photoresist on top of the FPA. We used polymerizable monomers such as IP-Dip and IP-L allowing transparency in SWIR range as the photoresist, but it should be note that they have absorption peaks at 3.33 μm and 2.86 μm [264]. A layer of 150μm thickness photoresist was deposited on the front surface of FPA. For practical fabrication in industry, microcone arrays operating in MWIR range can be fabricated with materials such as PET by injection molding introduced in Fig. 3.1(e-h) [179]. Second step is scanning the photoresist by the focused laser in Nanoscribe. The microcones can be formed by two-photon-induced polymerization and they can be designed to be centered with the corresponding photodetector mesas. The last step is to dissolve the unexposed parts of the photoresist to the laser beam.

Fig. 3.7(a) shows the first attempt of fabricating microcone array at a high scanning speed. The microcones showed layers in the structures which is determined by the large distance between the neighboring focusing planes. Fig. 3.7(b) shows the second attempt of fabrication at a low scanning speed and the sidewall surface of the microcones were first exposed and polymerized. Even though we can see the area of some microcones near the photodetector mesa bulged a little bit and some other problems, there are still

approximately half of the microcones did not show any visible imperfections. We used such microcone array with approximately 50% perfection to study the optical properties.

We asked our collaborators at AFRL to perform the optical characterization of the integration of the microcone array with front-illuminated FPA to measure the photoresponse of SWIR source. There are three types of photodetectors in 10×10 array fabricated on same die: (i) full fill-factor photodetector mesas with 58 μm aperture without integration with microcone array, (ii) photodetector mesas with 22 μm aperture without integration with microcone array, and (iii) photodetector mesas with 22 μm aperture integrated with microcone array. The photoresponse to the three structures were measured. The SWIR source is provided by a Thermo Scientific Nicolet 8700 FTIR spectrometer, and the spectral response was corrected by the reference spectrum obtained from a calibrated blackbody source.

The unpolarized photocurrent spectra from the front-illuminated Ni/Si Schottky barrier photodetectors we measured at low-temperature (80K) with a 1V reverse bias. It should be noted that the angular acceptance of all three types of front-illuminated SWIR FPAs discussed above were much larger than the narrow illumination cone (< 3°) at normal incidence.

The theoretical model of the optical performance of the fabricated microcone array is shown in the red curve of Fig. 3.5(f). However, there are two differences between the theoretical model and experimental measurements. First, as shown in Fig. 3.7(c), the position of the photoresponse peak is at λ = 1.08 μm, which is different to λ = 4 μm in our numerical calculations. Regardless of the significant deviation in the spectral range, the comparison between the theoretical modeling and experimental results can still be justified

since an additional calculation was performed to confirm that the $PEF_{2\text{-}D}$ values only have s small variation within ~10% between SWIR and MWIR, as shown in Fig. 3.6(d).

Second, the photodetector mesa in the fabrication has a size of 22 μm, which is much larger than the size of the bottom base of microcone D_b = 8 μm. According to our definition of PEF, it was normalized by the photoresponse to the same photodetector mesa without integration of microcone array. In this case, a larger mesa size leads to s maller PEF value. In our case, the corresponding theoretical $PEF_{3\text{-}D}$ can be accounted by dividing the $PEF_{3\text{-}D}$ estimated for 8 μm mesa which is ~50 by the increasing of mesa size of $(22/8)^2$ which is ~7.56, and the estimated theoretical $PEF_{3\text{-}D}$ value for a photodetector mesa with 22 μm size is ~6.6.

The main result of our optical characterization is the observation of the enhancement of photocurrent peak at λ = 1.08 μm for the 10×10 FPA with 22 μm mesa integrated with microcone array shown by the red curve in Fig. 3.7(c) to the photoresponse peak from the same FPA array without integration of microcone array shown by the blue curve in Fig. 3.7(c). The enhancement of the peak is ~0.27/0.09=3, which is found to be smaller than the predicted theoretical $PEF_{3\text{-}D}$ ~6.6, but this difference can be explained by considering the fact that only approximately half of the microcones were relatively perfect and functioning, the other half of the microcones were damaged.

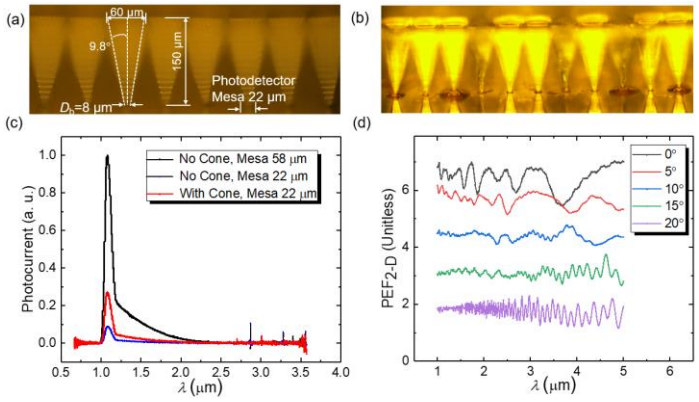

Figure 3.7: Microscope images showing results of the (a) high-speed and (b) Low-speed nanoscribe fabrication of the microconical arrays. (c) Photocurrent spectra from 10×10 arrays in the following cases: (i) full fill-factor detectors with 58 μm aperture without the microcones (black), (ii) detectors with 22 μm aperture without the microcones (blue), and (iii) detectors with 22 μm aperture with microcones (red). (d) $PEF_{2\text{-}D}$ values calculated at TE polarization show relatively small variations for each angle of incidence (α) in a broad spectral range $1 \leq \lambda \leq 5$ μm. Similar results were obtained at TM polarization. [222]

3.3 Conclusions

In conclusion, different ideas of designing light concentrators integrated with FPAs to reduce the thermal noise level and therefore improve the sensitivity, SNR, and imaging quality by different shape of structures and materials have been proposed. The two parameters of PEFs and AoVs of the light concentrators are the main evaluation method of the performance. The commercial microlens arrays as light concentrator usually allows high $PEF_{3\text{-}D} >> 10$ by varying the geometry of it, however an extremely narrow AoV < 2° caused by the long focal length (*f*) of conventional lenses has weakened the prospect of application for such design.

The high-index (n = 1.8) dielectric microsphere array as light concentrator integrated with front-illuminated FPAs allows a huge AoV > 20° due to its sharp focusing ability with extremely short focal length around several microns. However, the assembling of a monolayer of microspheres with small sizes and massive quantity and the alignment of the center of microspheres and photodetector mesas is very difficult in practical [223]. To make the alignment simpler, structures such as integrated microlenses [241], metalenses [242,245], and dielectric microdisk antenna arrays [243] which can be fabricated by

lithography were proposed as light concentrators, however the AOVs of those designs are rather limited.

In Chapter 2, we proposed three designs of regular and inverted microconical Si array integrated with different types of FPAs by different integration technologies [221]. The best performing results showed a unique resonant enhancement PEF>20 due to the resonant trapping of photons inside the microcones associated with the strong reflection on the metal mirror on the bottom base of microcone, and a fascinating phenomenon that the spectral peaks have the tendency to be fixed at certain positions at a broad range of angle of incident light up to 30° in both polarizations (TE and TM) were observed. Such design can be applied to the area of multispectral imaging with ~100m bands.

In this chapter, we proposed another microconical structure as light concentrators with low-index (n = 1.6) materials such as photoresist and plastic. It can be fabricated by nanoscale 3-D direct laser writing called Nanoscribe with the disadvantage of high-cost, low-speed, and imperfection or damage of the structures. Another method of injection molding is able to fabricate massive number of microcones in parallel with a fast speed which is favorable in industry.

The numerical analysis showed that the low-index (n = 1.6) micricones can be considered as tapered waveguide transmitting and delivering light from the top wider base to the bottom smaller based integrated with the photodetector mesa. A predicted maximal $PEF_{3\text{-}D}$ ~ 100 can be achieved for microcones with a slight tapered angle ($\theta \leq 10°$), small bottom base diameter ($D_b \leq 4$ μm) and sufficient height ($h \geq 120$ μm) under the assumption of $PEF_{3\text{-}D}$ is close to $(PEF_{2\text{-}D})^2$.

A real fabrication of microcone array with D_t/D_b = 60 μm/8 μm and h = 150 μm were fabricated by Nanoscribe with certain level of imperfection on top of the front-illuminated Ni/Si Schottky-barrier SWIR photodetectors with 22 μm mesas was done previously at AFRL. A three-fold enhancement of the photocurrent response was measured compared to that from a same photodetector mesa without equipped with microcone above. Even though there are damage and defect in the fabrication, these results are in a good agreement with my theoretical analysis and the numerical analysis of such design is important to provide theoretical support for the previous fabrication and characterization works.

Such proposed low-index (n = 1.6) microcone array can be used as light concentrators integrated with different types of front-illuminated MWIR FPAs built in different material systems such as Pt/Si or Au/Si Schottky-barrier, T2SL, III-V QE and QD detectors to reduce the individual photodetector mesa size to decrease the thermal noise level without sacrificing the photoresponse efficiency, and therefore improve the sensitivity, SNR and imaging quality of the thermal imaging devices.

CHAPTER 4: LABEL-FREE CELLPHONE MICROSCOPY ASSISTED BY HIGH-INDEX CONTACT BALL LENS WITH DIFFRACTION-LIMITED RESOLUTION

4.1 Introduction of cellphone microscopy

As we introduced in Chapter 1, super-resolution beyond the diffraction limit has been widely developed by various methods such as NSOM [191,192], assisted with superlenses [193-197], nanoplasmonic structures [198,199], nSIL [37], and microspheres [38,39,42]. The resolution beyond the solid immersion lens limit of ~$\lambda/4$ was reported in these studies. Such super-resolution permits the observation of nanoscale structures using label-free microscopy.

In the early 1990s, the development of megapixel CCD sensor arrays in digital cameras brought up a revolution in imaging technologies. In particular, it stimulated developing portable and lightweight imaging systems to replace the bulky and expensive conventional microscopes. The cellphones in people's daily life with high-quality CCD camera and well-designed optics can work as a pocket-size inexpensive microscope which can be taken to the most remote areas in the world. Besides remote locations on our planet, such portable microscope systems can be used in space exploration to study origins of life on different planets or meteorites. Most importantly, they can be applied to biomedical areas such as diagnostics of skin cancers without invasive biopsy which can be performed by inexpensive, portable and user-friendly devices without using expensive

and complicated instruments such as reflectance confocal microscopy, optical coherence tomography, multiphoton microscopy, and Raman spectroscopy [265].

The resolution of cellphone with CCD camera is far below the diffraction limit which is determined by the finite pixel size on CCD chip. Typical cellphone has a resolution ~30 μm. It is needed to be improved to be used in any biomedical applications. One of the first designs of compact imaging system with CCD chip is a microfluidic chip integrated on top of the CCD chip without any optical elements such as lenses is shown in Fig. 4.1. The biomedical samples such as worms are floating inside the channel and illuminated from top. The shadow of the floating worms can be captured by the CCD chip below with a resolution determined by the size of the pitch of the photodetectors array on CCD chip in a 5-10 μm range [266]. The resolution of the CCD chip can be improved by introducing additional magnifications using additional nanoaperture arrays in combination with the microscope imaging which is called optofluidic microscopy (OFM) [267]. Such OFM techniques with improved resolution, however, makes the imaging system more complex and bulkier by involving microscopes, so that it is not a pocket-size imaging system we desired to build with CCD camera.

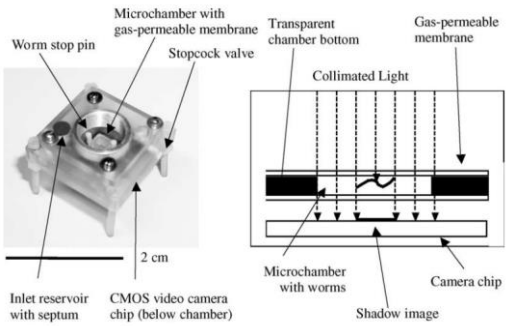

Figure 4.1: Photograph and schematic diagram of the worm imager. Nematodes in a 500 μm high microchamber are illuminated with an LED

and cast a shadow onto a CCD video camera chip attached at the bottom of the chamber. [266]

Another method to improve the resolution of CCD camera is digital in-line holographic microscopy (DIHM) shown in Fig. 4.2. The object is luminated by a spherical wave emanating from a small aperture, and the scattered light which passes through the objects such as cells or microparticles will interfere with the unscattered light and create a hologram of the object, which can be captured by CCD camera. The hologram of each object allows rapid reconstruction of its microscopic image through digital processing [268,269]. Such holographic imaging on CCD chip has a large field-of-view (FoV), but the resolution is limited in a micron-scale. Also, the computational load is significant since it requires rapid reconstructions of images. In addition, the objects are required to be positioned in close proximity to the CCD detectors so that the conventional biomedical samples on standard microscope slides cannot be studied by this technique.

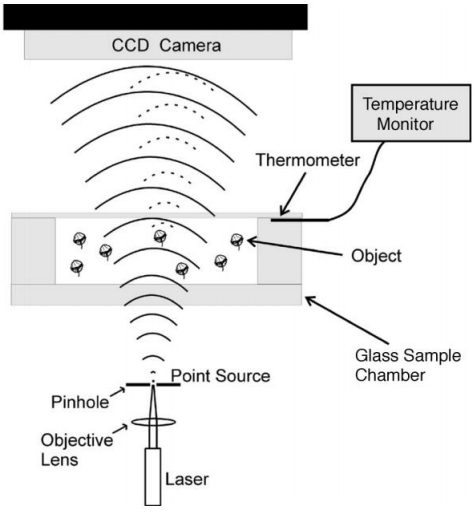

Figure 4.2: Experimental arrangement for biological applications of DIHM. [268]

To further increase the resolution of CCD camera, additional magnification is needed to be introduced which can be provided by a standard microscope objective. Usually, the resolution and magnification concepts are treated separately in the optical microscopy. However, they become directly related in a limit when the resolution is determined by the finite pixel sizes. Fig. 4.3 shows a combination of cellphone camera with an achromat objective with NA = 0.85 and a magnification of 60× and a 20× wide field microscope eyepiece which provide a FoV ~180μm for the system and an effective additional magnification to the cellphone camera of 28×. A spatial resolution of 1.2μm was claimed for such imaging system, which is still three times worse than the diffraction limit. [270]. In addition, the use of microscope objectives and a series of optical elements such as filters and lenses make the imaging system to be bulky and expensive.

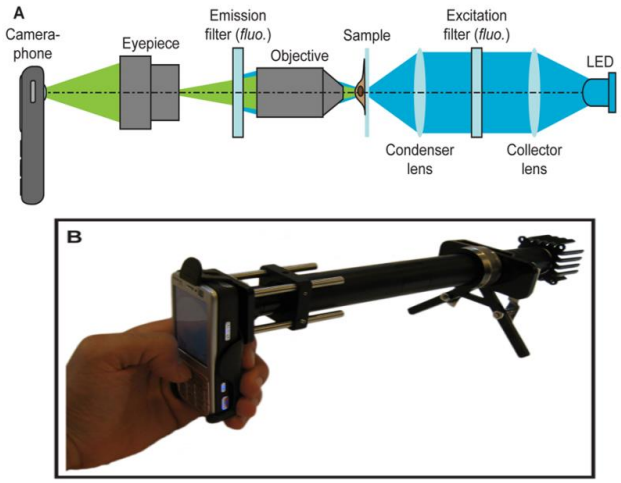

Figure 4.3: (a) Mobile phone microscopy optical layout for fluorescence imaging. (b) A current prototype, with filters and LED installed, capable of fluorescence imaging. [270]

To simplify the imaging system by removing the microscope objectives, a microlens was used to provide the additional magnification as illustrated in Fig. 4.4 [238].

It should be noted that using ball lenses will lead to significant aberrations which will damage the image quality towards the edges of FoV [271]. There is also a fundamental tradeoff in imaging between the magnification and FoV. The additional magnification provided by the microlens was rather limited and the best resolution achieved for imaging fluorescent objects was about 1.5μm [238, 271-274].

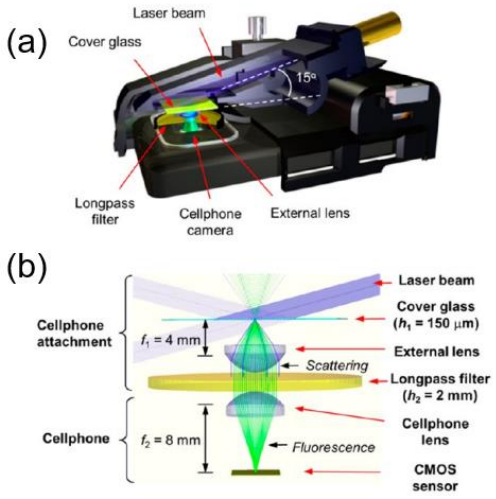

Figure 4.4: (a) Schematic illustration of cellphone-based fluorescence microscope. (b) Ray-tracing diagram of the cellphone microscope where excitation and scattered beams are indicated with solid blue rays, while the fluorescent emission is highlighted with solid green rays. [238]

Considering the requirements of imaging conditions for compact, simple, and inexpensive devices, a label-free imaging with white light assisted by microspheres is the favorable way to improve the resolution of cellphone. Mesoscale microspheres are required for conventional microscopy for super-resolution, however the typical magnification values for virtual imaging through such spheres are limited and, in addition, FoVs are also rather limited.

To overcome these limitations, in this dissertation, we propose a novel label-free cellphone microscopy assisted by significantly larger (millimeter-scale) ball lenses with index of refraction sufficiently close to two. Specifically, we studied ball lenses made by high-index material LASFN35 glass with a n = 2.049 at λ = 480nm in contact with the object. In this Chapter, we show that according to geometrical optics, a huge additional magnification up to 50× can be provided through such contact ball lens, which leads to a significant improvement of the resolution of cellphone camera from ~30μm to ~600nm. Such resolution is three times better than the best current results for cellphone microscopy, which breaks the limitation of finite pixel size on CCD chip and approach to the diffraction of light. We show that such label-free cellphone microscopy with high resolution can be applied to diagnosis skin diseases such as melanoma *in vivo* without invasive biopsy.

4.2 Fabrication of metallic double-stripe array as objects

To evaluate the magnification and resolution of cellphone microscopy, objects with recognizable shape and known dimensions are required. To obtain high-quality images, objects with high contrast properties are preferred such as highly reflecting metallic nanostructures fabricated on transparent substrates. To quantify the resolution with high accuracy, the characteristic features of objects should be comparable in size to the resolution of imaging system.

In this dissertation, we fabricated a standard Au double-stripe array deposited on sapphire substrate by using electron-beam lithography. Fig. 4.5 shows the schematic of the Au double-strip array with high reflectance fabricated on sapphire substrate with high

transparency in the visible regime. Each unit in the array contains two stripes with a gap between them. The width of the stripes is designed to be 1.0μm, and a series double-stripe arrays with varying gaps from 0.4μm to 0.7um were fabricated to find the best situations for the resolution quantification. According to the definition of resolution introduced in Chapter 1, the ability to resolve the smallest gap sizes represents the resolution capability of the system. However, the direct use of such minimally resolvable gap sizes as a resolution measure is incorrect in general case, and more rigorous resolution quantification procedure is required.

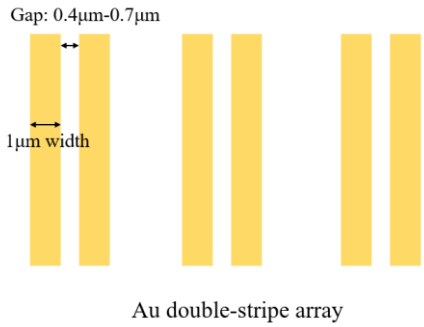

Figure 4.5: Schematic of Au double-stripe array deposited on transparent sapphire substrate. Each unit contains two stripes with 1.0μm width and a gap with variable sizes between 0.4μm to 0.7μm between them.

We performed electron beam (E-beam) lithography to fabricate such structures. Fig. 4.6 shows the fabrication procedure. First, we drew the double-stripe array with designed dimensions in Raith 150, the E-beam lithographer. Then we deposit a layer of positive E-beam resist polymethyl methacrylate (PMMA) on sapphire wafer by spin coating with 1000rmp for 60s. The theoretical thickness of PMMA is 407nm according to the recipe [275]. A thin layer of Cu with 15nm thickness was deposited on top of PMMA layer to provide conduction of electron beam. The electron beam can penetrate through Cu layer and pattern PMMA. After that the sapphire wafer was placed in Raith to be

exposed under electron beam. Since the PMMA is used as positive resist, the exposed parts will be strengthened and other parts without exposure can be removed later by developer CD-24, and the designed double-stripes arrays of PMMA can be preserved. Then the sapphire wafer was placed in Lesker E-beam evaporator to deposit a layer of Au with 100nm thickness on patterned PMMA layer. After the liftoff by removing the PMMA resist, the Au double-stripe array is deposited on top of sapphire wafer.

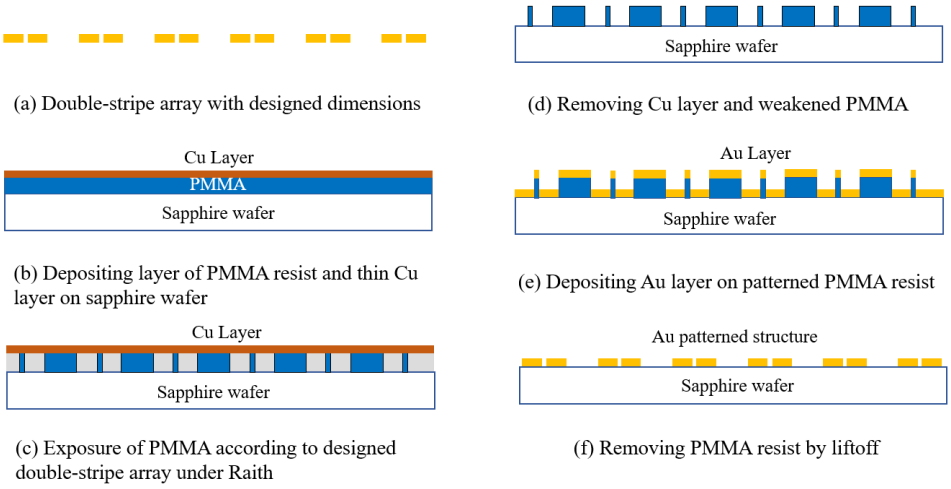

Figure 4.6: Fabrication procedure of Au double-stripe array deposited on sapphire substrate by electron beam lithography.

Fig. 4.7 shows the scanning electron microscope (SEM) images of Au double-stripe arrays with different dimensions by using E-beam lithography introduced above. The actual width of the stripes is approximately 1.1μm, while the fabricated gaps have averaged values of 469nm, 537nm, 644nm, and 707nm. Those four double stripe arrays with different gaps will all be used as objects to quantify the resolution of cellphone microscopy.

Besides the double-stripe array fabricated by E-beam lithography as objects, we purchased the Siemen's Star (Edmund Optics, Fused Silica slide with Chrome deposite)

as the second object to quantify the resolution of cellphone microscopy. Siemen's Star is a standard imaging target for testing the imaging system, which consists of a pattern of metallic "spokes" on a transparent substrate that radiate from a common center and become wider as they get further from it, as shown in Fig. 4.8. Both the double-stripe array and the Siemen's Star will be used to quantify the resolution in this dissertation.

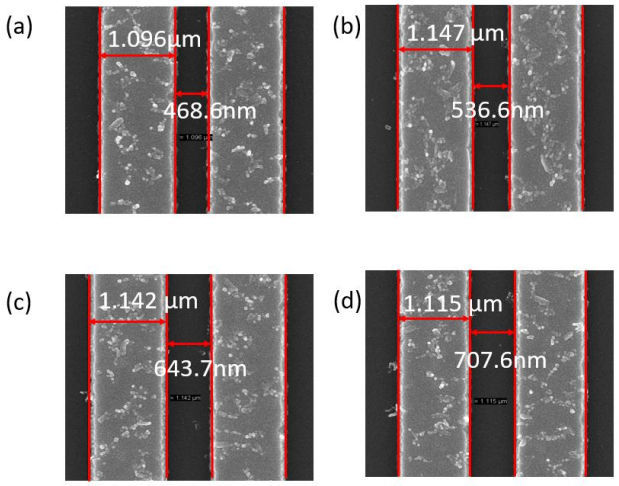

Figure 4.7: SEM images of Au double-stripe arrays with different dimensions by using E-beam lithography. The actual width of the stripes is approximately 1.1μm, while the fabricated gaps have averaged values of 469nm, 537nm, 644nm, and 707nm.

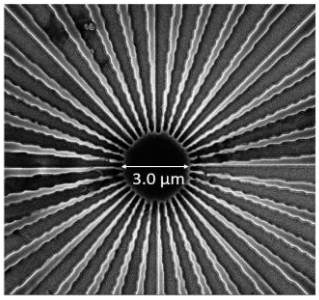

Figure 4.8: SEM image of Siemen's Star.

4.3 Magnification quantification of LASFN35 ball lens

Since the resolution of cellphone camera is far below the diffraction limit and it is limited by the finite pixel size on the CCD camera chip, introducing an additional magnification to the cellphone camera is critical to improve the resolution of it. To this end, we proposed the new cellphone microscopy assisted by contact ball lens. Fig. 4.9 shows the schematic of our proposed cellphone microscopy. The double-stripe array (Electro-beam lithography, sapphire slide with Au deposite) as the object is placed on a diffuser and illuminated by white light source from below to achieve label-free imaging. The LASFN35 ball lens (Swiss Jewel Company) with diameter D = 2.0mm is placed on top of the object, and a real image of the object was found to be formed above the object. A magnified image of object is captured by cellphone camera by focusing the camera on the real image plane. The magnification of such real imaging through the ball lens is the key for improving the resolution of cellphone camera. Diffusers with 10nm bandwidth and central wavelength of λ = 430, 480, 546, 589, and 632nm was inserted below the cellphone camera to provide illumination with different wavelengths considering the dispersion effect of the material.

In the limit of geometrical optics, the lateral image magnification (M) of ball lens is determined by the following equation [63,65]:

$$M\left(n',d,g\right)=\frac{-n'}{2\left(n'-1\right)\left(\frac{2g}{d}+1\right)-n'}\ , \quad (4.1)$$

Where D is the diameter of the ball lens, $n'={}^{n_{sp}}/_{n_0}$ is the refractive index contrast between the ball lens and object space, and g is the gap between the object and ball lens. For contact ball lens when g = 0, formula (4.1) is simplified to,

$$M(n', D) = \frac{-n'}{n'-2}, \qquad (4.2)$$

Where the magnification is determined only by the refractive index contrast of ball lens.

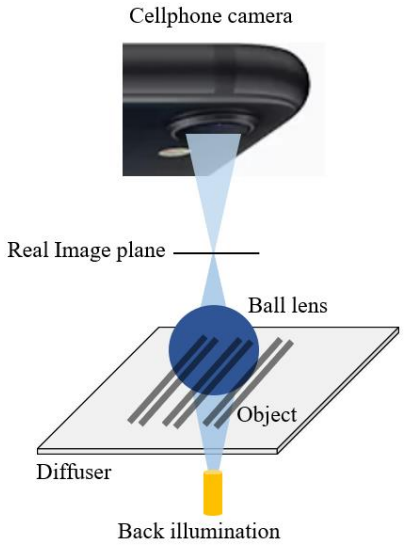

Figure 4.9: Schemtaic of label-free cellphone microscopy assisted by contact ball lens with high refractive index n = 2.049 at λ = 480nm.

There are two imaging modalities through ball lens or microsphere according to geometrical optics: virtual imaing and real imaging shown in Fig. 4.10. For a ball lens with refractive index contrast less than certain values, it forms a virtual image below the object, and the cellphone originally focus on the object needs to be moved lower to capture the its vritual image. For ball lens with refractive index contrast larger than certain values, the ball lens forms a real image above the object, and the cellphone orignally focus on the object needs to be moved higher to capture its virtual image. The threshold refractive index contrast for switching from virtual to real imaging is determined by the diameter of the ball lens D and the gap between the ball lens and object g. According to geometrical optics, the position of the image formed by the ball

lens is related to its magnifcation. We define the focusing distance *d* as the distance from the object to the virtual or real images, which allows to represent the magnification by the following equation:

$$M = 2\frac{d}{D} - 1\,, \quad (4.3)$$

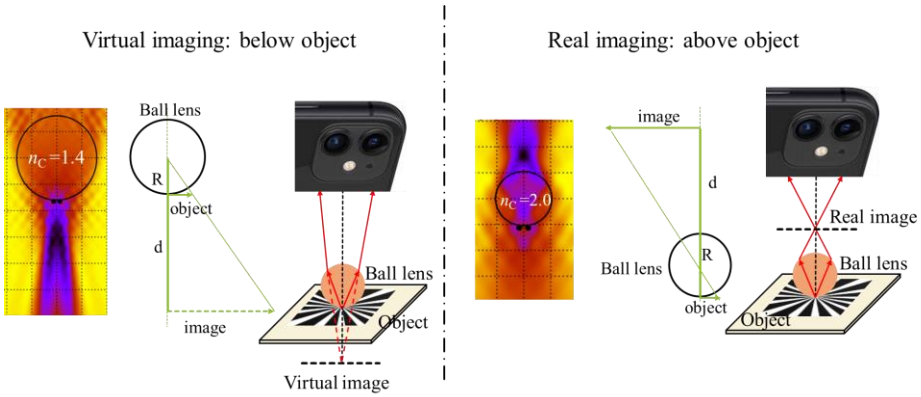

Figure 4.10: Imaging modalities of virtual imaging and real imaging through ball lens in cellphone microscopy. [36]

Fig. 4.11 shows the plot of Eq. (4.2) of how the magnification through contact ball lens in contact conditions with the objects depends on the refractive index contrast. For refractive index contrast $n' < 2$, the contact ball lens forms a magnified virtual image below the object, and the magnification is increasing while the refractive index contrast is approaching a threshold value of 2. The positive value of magnification represents a regular orientation (same up and down sides of the object and image) of image. For refractive index contrast $n' > 2$, the contact ball lens forms a magnified real image above the object, and the magnification is also increasing while the refractive index contrast is approaching 2. The negative value of magnification represents an inverted orientation (opposite up and down sides of the object and image) of image. The datapoints on the left curve are measured magnification values for virtual images through contact ball lens

made by BK7 glass with refractive index n = 1.517 and diameters D = 0.5, 1.0, 1.5, 2.0, 4.0, 8.0mm, fused silica glass with refractive index n = 1.46 and diameter D = 4.0mm, LAF22 glass with refractive index n = 1.76 and diameter D = 1.25mm, and LASFN9 glass with refractive index n = 1.85 and diameter D = 1.5 and 2.0mm. All the experimental values of magnification match the theoretical formula pretty well, and we can tell by the examples of BK7 glass ball lenses that the magnification is the ball lens diameter-independent if the ball lens is in contact with the object. For refractive index contrast n' close to 2, a huge magnification can be obtained (red circles) which can be used to significantly improve the resolution of cellphone camera.

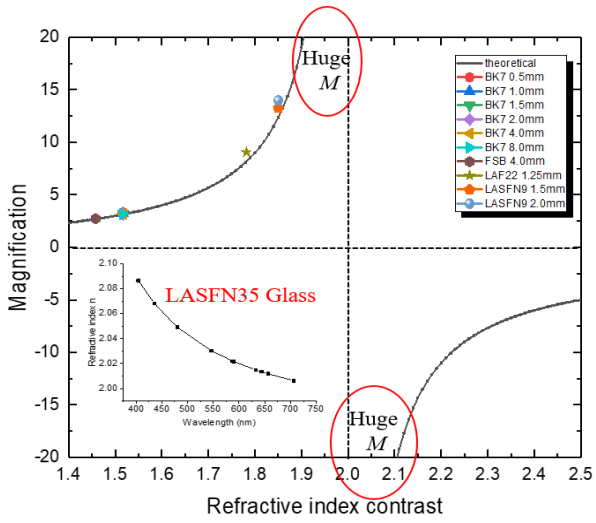

Figure 4.11: Magnification (M) varying with refractive index contrast n' for contact ball lens when g = 0. Insert: dispersion curve of LASFN35 glass in visible spectral range.

According to geometrical optics, the magnification through contact ball lens is significantly increased and widely varied when refractive index contrast n' is close to 2. In our work, we use a special glass LASFN35 with a refractive index of n = 2.049 at λ = 480nm which is really close to 2 to build the contact ball lens. It is shown that the

theoretical magnification of 42 times through LASFN35 glass ball lens can be obatined, which could significantly improve the resolution of celphone microscope limited by the finite pixel size. Also, the dispersion of LASFN35 glass in visible region shown in the insert in Fig. 4.11, which changes the refractive index by 0.05 from λ = 430nm to λ = 632nm. It would introduce a substatial magnification change from 30 times to 135 times theoretically, and allows different resolution capability for different incident illumination wavelengths.

Fig. 4.12(a) shows the images taken by cellphone camera of Siemen's Star (Edmund Optics, Fused Silica slide with Chrome deposite) and metallic double stripes (Electro-beam lithography, sapphire slide with Au deposite) through contact LASFN35 glass ball lens captured by cellphone camera. The illumintation is provided by the diffused white light source from below, and five different filters with λ = 430nm, 480nm, 546nm, 589nm, and 632nm are inserted (one at a time) to provide different incident wavelengths and therefore different magnifications influenced by the dispersion effects. For imaging Siemen's Star (first row), the ball lens is placed slightly off the center of Siemen's Star to make sure that the central black region of Siemen's Star is located at the edge of FoV and the srtipes are located at the center of the image where the pincushion distortions are minimized. For imaging double stripe structure, the ball lens is alighned with the center of double stripe to obatain best quality images. It is illustrated that the magnification is different for different illumination wavelengths., Longer wavelengths lead to smaller refractive index contrasts providing higher magnifications. Fig. 4.12(b) shows the magnification (M) through the ball lenses with different diameters in the limit of geometrical optics for five different illumination wavelengths. A significant

magnification in excess of 100× can be expected for ball lens made by LASFN35 glass. The black dashed lines represent the theoretical relationship between the magnificaiton and focusing distance limited by geometrical optics in Eq. (4.3). It illustrates that the magnification is the ball lens diameter-independent for contact ball lenses. For a fixed magnification, larger diameter ball lens should have longer focusing distance.

Fig. 4.12(c) shows the experimental magnification through the ball lens with different diameters of D = 0.5mm, 1.0mm, and 2.0mm at different illumination wavelengths. To measure the magnification experimentally, images of the objects with known size are taken by both original cellphone (reference case) and cellphone equipped with the contact ball lens. The μm/pixel value of both images are measured, and their ratio represents the additional magnification by the ball lens. It is shown that different diameters of ball lens tend to have roughly the same magnification, and larger diameter of ball lens shows longer focusing distance. However, the experimental value of magnification is much less than theoretical value. This could be explained by the fact that the predictions of geometrical optics are based on paraxial approximation. It leads to a longer focusing distance and therefore larger magnification. In real experiment, the imaging through the ball lenses with relatively large diameters is actually formed predominantly by off-axial rays. In addition, such imaging is a subject for strong spherical aberration. The corresponding of-axis rays cross closer to the object. Effectively, it leads to much shorter focusing distance and less magnification observed in our experiments. Still, large experimental magnification values around 50 times are obtained and an improvement of resolution for cellphone microscope imaging system can be expected.

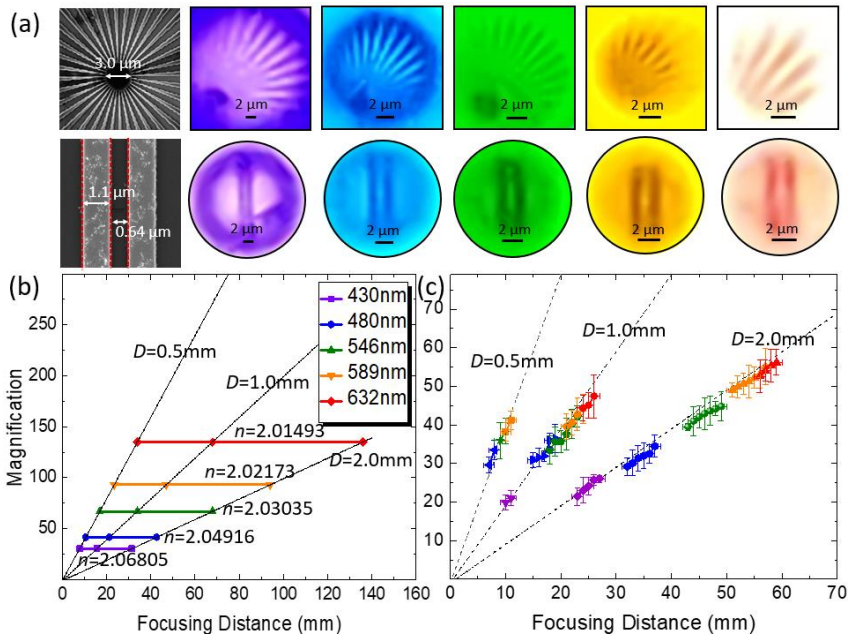

Figure 4.12: (a)The SEM images of the objects of Siemen's Star and metallic double stripes, and the images through the imaging system of cellphone camera plus LASFN35 ball lens at five different illumination wavelength. (b) Image magnification through conatct ball lens limited by geometrical optics for different diameters of ball lens at diferent illumination wavelength. (c) Experimetal iamge magnification captured by cellphone camera thorugh contact ball lens.

4.4 Resolution quantification of cellphone microscopy

The main point of introducing different illumination wavelengths is to obtain better resolution by providing larger magnification values due to dispersion effects. The key point of this dissertation is the improvement of resolution of cellphone camera that a contact LASFN35 ball lens can introduce. As stated in Chapter 1, three methods to quantify the resolution of the ball lens microscopy have been used historically: (i) determining the minimal resolved feature size, (ii) 1-D or (iii) 2-D convolutions. In this chapter, we are using the most accurate method of 2-D convolution to quantify the resolution. Double-stripe arrays and Siemen's Stars have been used to quantify the

resolution, and the resolution of the whole imaging system through ball lens with different diameters at different illumination wavelength have been all quantified.

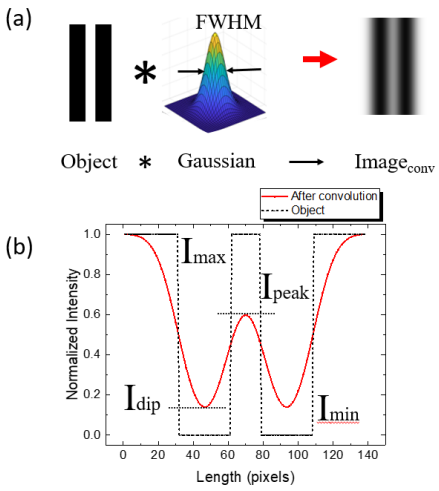

Figure 4.13: (a) Formation of images through imaging system by convolution. (b) Fitting of the experimental and convolutional intensity profiles of the images of double-stripe array.

According to a Houston resolution criterion, the resolution of imaging system is found as a FWHM of the Gaussian PSF providing the best fit of the convoluted images to the experimental images [63,65]. Fig. 4.13(a) illustrate the concept that images can be calculated as a result of convolution of object and the PSF of the imaging system. If we make an assumption that PSF of the imaging system is sufficiently close to the Gaussian function, the resolution can be determined as its width according to Houston criterion. In this case, the intensity profile of an ideal object can be obtained with the dimensions in the image plane measured in pixels. It can be calculated considering the real dimensions of objects in μm and taking into account the μm/pixel value determined due to the known magnification value (*M*). We performed the convolution of the intensity profiles of the idealized "drawn" objects with the perfect shape with Gaussian functions with varying

FWHM and obtain a series of intensity profiles for the convolutional images. When the intensity profiles of the calculated images and the experimental images taken by cellphone microscopy show the maximal similarity, the FWHM of the corresponding Gaussian function is accepted as the resolution of the cellphone microscopy.

Fig. 4.13(b) shows typical shape of the intensity profile of images after convolution. It should be noted that in our cellphone microscopy, the objects are illuminated from below in transmission mode for convenience, so that the two metallic stripes are blocking the light and appear dark. The gap between them appears bright. The intensity limits for different parts of object before passing through the imaging system can reach 0 and 1 (0 and 255 in RGB region) since they are located in strong reflecting and transmitting regions of the object, respectively. After passing through the imaging system, the intensity of the gap between the two stripes can never reach I_{max} which is limited by the resolution of imaging system. Same applies to the intensity of the stripes which cannot reach I_{min} for the same reason. For accurate resolution quantification, it is extremely important to define a reasonable I_{max} and I_{min} values for normalization of the intensity profiles of experimental images so that the I_{peak} and I_{dip} will not reach I_{max} and I_{min}.

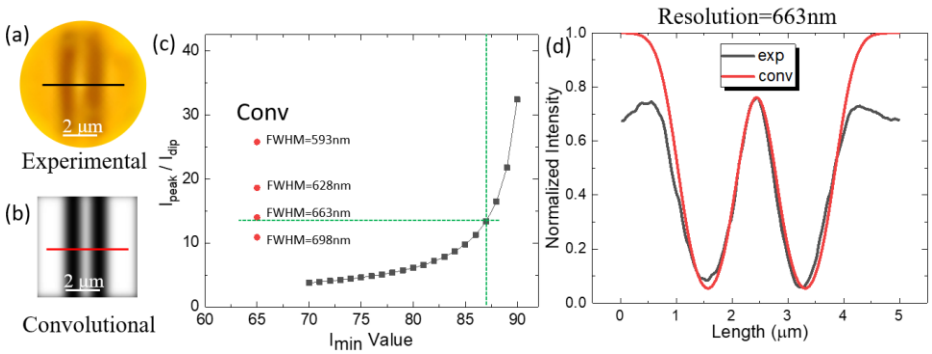

Figure 4.14: (a) and (b): Experimental and convolutional images of double-stripe unit at illuminating wavelength λ = 589nm. (c) Determining the I_{min} value for experimental image to fit the convlution result the best (d) Best fitting results of normalized intensity profiles of experimental and convolutional images indicating a resolution of 663nm of cellphone microscopy.

Fig. 4.14 shows an example of comparison of experimental and calculated images to quantify the resolution. After we obtain the experimental and convoluted images shown in Fig. 4.14(a) and 4.14(b), we extract the intensity profiles along the cross-section lines in the center of the images. The calculated intensity profile does not require a normalization, but the experimental intensity profile needs to be normalized by choosing the reasonable I_{max} and I_{min} values. The normalized intensity can be expressed as:

$$normalized\ \frac{I_{peak}}{I_{dip}} = \frac{(I_{peak}-I_{min})/(I_{max}-I_{min})}{(I_{dip}-I_{min})/(I_{max}-I_{min})}, \quad (4.4)$$

In principle, the values of I_{max} and I_{min} refer to the maximum and minimum intensity that such imaging system would produce. For the intensity profile, the I_{max} will be the intensity of the side lobs where a high transmission of light away from the double stripes takes place. However, the intensity distribution within FoV has a certain distribution function with the maximum at the center of FoV. For this reason, the intensity of experimental images is maximal in the central area of gaps, and the intensity is decreasing towards the side lobs, as illustrated in Fig. 4.14(c). From a more general point of view, this is related to the fact that FoV of such cellphone microscopy assisted by single contact ball lens is limited and the only the central area provide good imaging quality. Taking into account this situation, we decided to choose the maximum intensity outside the double-stripe area (imaged through the ball lens) to represent the I_{max} value for normalization. As for the value of I_{min}, it should be associated with the minimal value

of background intensity (imaged through the ball lens) due to random scattering. In fact, the value of I_{min} was difficult to determine precisely, and we had a freedom to vary this parameter in a certain range. We calculated the I_{peak} / I_{dip} ratio by varying the value of I_{min} in RGB color imaging region (0, 255). The red points in Fig. 4.14(c) are the values of I_{peak} / I_{dip} ratio for calculated intensity profiles with different FWHM of Gaussian function, which also represent the resolution of the imaging system. We chose the value of I_{min} based on the best agreement of the calculated of the I_{peak} / I_{dip} ratio with the experimental intensity profiles. In the case shown in Fig. 4.14(c), the values of I_{max} and I_{min} are 174 and 87, respectively. Fig. 4.14(d) shows the normalized intensity profiles of experimental and calculated results indicating a resolution of 663nm.

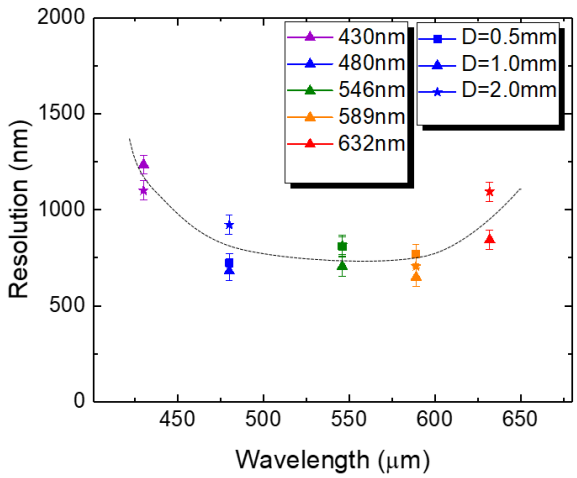

Figure 4.15: The resolution quantification results for different diameters of the ball lens at differetn illumination wavelength.

Figure 4.15 shows the summary of resolution of the imaging system through the ball lenses with different diameters at different illumination wavelength. First, different diameters of ball lenses with same illumination wavelength tend to have same resolution. At the shortest wavelength λ = 430nm, the resolution is found to be around 1200nm. For

longer wavelengths λ = 480nm, 546nm, and 589nm, the resoution is found to be improved to around 600nm. This result is consistent with our expectations that longer wavelength providing larger magnification values should also provide better resolution. However, for the longest wavelength λ = 632nm, the resolution is worsening again to around 1000nm. In principle, this behavior can be explained by the fact that the resolution is no longer limited by finite pixel size of cellphone camera but follows the classical diffraction limit. To summarize our results, we claimed that a sub-micron resolution ~600nm is demonstrated in our work for cellphone camera assisted by single contact ball lens. This resolution is three times better than the best published experimental results for the cell phone microscopy. It can also be explained by the fact that we approached the diffraction limit imposed by a finite numerical aperture (NA) introduced by our high-index ball lens placed in contact with the object. Based on the obtatined resolution value, the effective NA value achieved in our experiments can be estimated to be around 0.5.

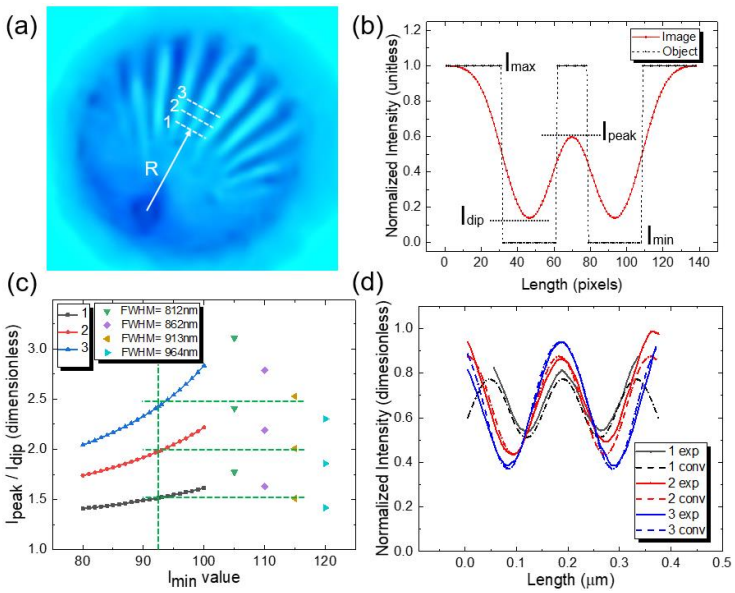

Figure 4.16: (a) Image of Siemen's Star by cellphone microscopy with λ = 480nm inserted, (b) Intensity profile of object passing through imaging system, (c) I_{peak} / I_{dip} ratio for different I_{min} value, (4) Fitting of experimental and convolutional results for Gaussian function with FWHM = 913nm.

The resolution of the same cellphone microscopy was also quantified by using a Siemen's Stars as an object. Fig. 4.16(a) is the image of Siemen's Star by cellphone microscopy assisted with ball lens with λ = 480nm filter inserted. Since the central part of FoV is the least distorted, we micromanipulated with the ball lens until we obtained the region of Siemen's Star maximally suitable for the resolution quantification at the center of FoV. The intensity profiles of two neighboring spokes at three different radial distances are extracted. The advantage of quantifying resolution using Siemen's Star is that the dimensions of the stripes and gaps are gradually varying at different radial distances, and they can be studied in the same image. The whole case can be viewed as an example of double-stripe arrays with different widths and gaps represented in a single image. From the point of view of modeling, after passing through the same imaging system, the intensity profiles of these double-stripes with different dimensions are modified by convolution with the same PSF (Gaussian function). This means that the experimental intensity profiles of different double-stripe units should be all simultaneously described by the calculated results with same Gaussian function. This allows a self-checking or averaging of quantification to make the resolution estimation more accurate.

Fig. 4.16(b) shows the changing of intensity profile of two-spokes object through imaging system. The image is the convolutional result of object and Gaussian function, and the FWHM of the Gaussian function is the resolution of imaging system.

Fig. 4.16(c) shows the I_{peak} / I_{dip} ratio changing with different I_{min}. We follow the exactly the same procedure to determine the I_{max} and I_{min} values for experimental images. When the best fitting can be found for all three radial positions at the same time, the value of I_{max} and I_{min} are found to be 180 and 92.5 in FoV for RGB color image with intensity region (0, 255), respectively. After normalization, the fitting of experimental and calculated intensity profiles is shown in Fig. 4.16(d). It is shown that three intensity profiles measured at three different radial distances are found to be in a good agreement with the results calculated with the same FWHM of Gaussian PSF. Therefore, using Siemen's Stars as an object we obtained a resolution less than 1μm for cellphone camera assisted with a single contact ball lens.

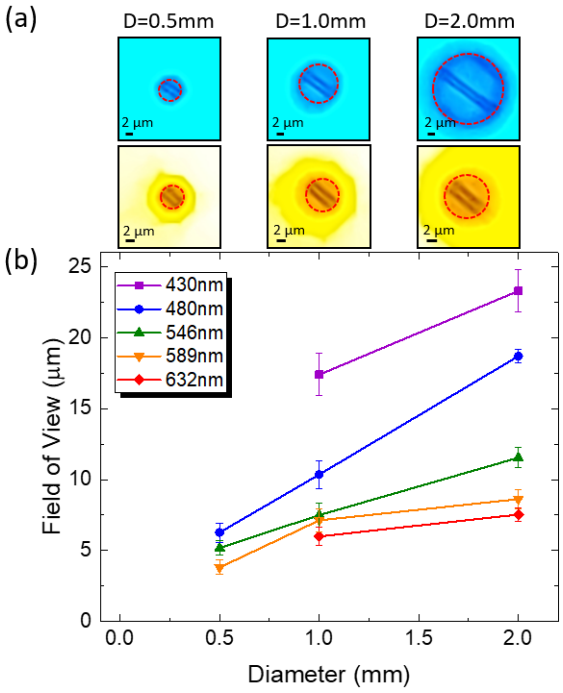

Figure 4.17: (a) The FoV region (red dashed circle) of the images for different diameters of the ball lens at λ = 480nm and λ = 589nm (b) The FoV values for trhee different diameters of the ball lens at five different illumination wavelength.

The limitation of the proposed imaging technology is related it its limited FoV. It is known that imaging through microscope objective leads to a tradeoff between the magnification and FoV. We study such tradeoff for the cellphone imaging throught the contact ball lenses. Fig. 4.17(a) shows the FoV of ball lenses with thediameters D = 0.5mm, 1.0mm, and 2.0mm at different illumination wavelength λ = 480nm and 589nm. Making a decision about the size of FoV is somewhat arbitrary. In our work, we relied on an intuitive distinguishing of the central region with the best quality of imaging and circular shape. We consistently used the same visual semi-intuitive criteria for defining the size of FoV in different situations. This is illustrated by the diameter of red dashed circle region on the object plane. Fig. 4.17(b) shows the estimated FoV in μm for five different illumination wavelength and three different diameters. The value of FoV in μm is determined by the pixel number of the diameter of FoV multiplied by the μm/pixel value for each illumination wavelength.

For the same illumination wavelength, the μm/pixel value for different diameter of ball lens are found to be similar since they have similar magnifications. At the same time, and the larger ball lens tend to have larger diameter of FoV, which can be seen from Fig. 4.17(a). In this case, the FoV in μm for the same wavelenght is increasing with diameter of the ball lens. This becomes especially pronounced for λ = 589nm and 632nm, where the focusing distance (d) becomes so long that the cellphone has to be moved very far away from the ball lens. It is seen that the diameter of FoV for ball lens with the diameter D = 2.0mm is almost the same as that for the ball lens with D = 1.0mm. In addition, it is seen that the shorter wavelength tend to have larger FoV in μm. This behavior takes place due to the fact that for shorter wavelength the larger magnification

leads to a smaller μm/pixel value. In this situation, a similar diameter of FoV in pixels, results in a larger FoV in μm for shorter wavelenghts.

Such limited FoV can be viewed as a limiting factor of the proposed imaging for developing biomedical applications of cellphone microscopy. One of the solutions for this problem is shown in Fig. 4.18 that develpoing a microprobe attached to the ball lens which can provide fast scanning over the wide field of biomedical samples to enlarge the FoV. Since the FoV through single ball lens is limited around ~20μm, the scanning step can be set as ~10μm to provide an overlap between the neighboring images which can be stitched on the next step to provide the image of the whole field of the samples. Another solution to this limited FoV is to assemble a monolayer of microspheres with compact arrangement to image different positions over the wide FoV through different microspheres at the same time. This solution will be introduced in detail in Chapter 5.

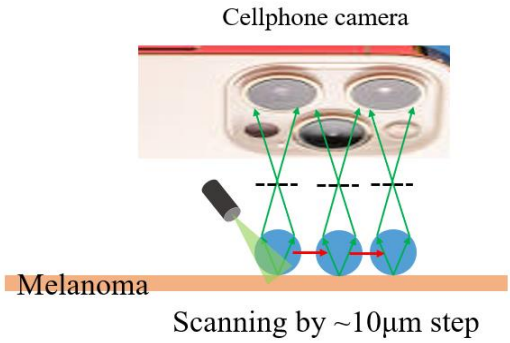

Figure 4.18: Schematic of enlarging the FoV by fast-scanning over the sample by attaching microprobes to the ball lens.

4.5 Application of diagnostics of melanoma *in vivo* without biopsy

Microscopy with high resolution have been widely used in biomedical and clinical field to diagnose and prognose diseases. Observing aimed symptoms by

user-friendly and portable devices *in vivo* without sending smear and section slides of samples to clinics is an important direction of research. The idea of imaging by cellphone camera through contact ball lens will allow the diagnosis of various diseases such as melanoma *in vivo* since the ball lens can be in contact with the skin directly.

Melanoma has been considered as immunogenic malignancy as it contains great number of immune cells, and the development and progression of it requires the interaction with immune cells such as lymphocytes in tumor environment [276,277]. Besides the tumor thickness, the distribution and density of tumor infiltrating lymphocytes (TILs), which means infiltration and disruption of lymphocytes into tumor nests or direct contact between lymphocytes and tumor cells, shows prognostic significance [276,278,279]. The most used Clark and MIA system show their distinct grading based on the distribution pattern and density of TILs and indicate that the more diffusive infiltration lymphocytes in the entire invasive component, more serious the tumor is [277,278,280,281]. Fig. 4.19(a) shows the image of cross-section sample of melanoma (Carolina Biological Supply Company) taken by 10x standard microscope objective. The melanoma cells and lymphocytes cells are labeled which indicates a mild interaction between them. In Fig. 4.19(b), an ordinary cellphone camera cannot resolve a cell-scale structure to judge the grade of TILs. However, by placing a ball lens on top of the sample, the real image of the sample through ball lens can be captured by cellphone camera and the details can be resolved easily due to the additional magnification from ball lens. Fig. 4.19(c) to 4.19(h) show the images of melanoma sample through ball lenses made by LASFN35 glass with n = 2.03 and D = 2.0mm, LASFN9 glass with n = 1.85 and D = 1.5mm, and LAF22 glass with n = 1.78 and D = 1.25mm captured by

cellphone camera. Due to a coverslip with a thickness around 0.2mm on top of the melanoma sample, the LASFN35 ball lens provide an additional magnification of 5.7×, the LASFN9 ball lens provide an additional magnification of 9.5×, the LAF22 ball lens provide an additional magnification of 11.1×, which all allows a big improvement of resolution of cellphone camera to resolve single lymphocyte cell. By assembling a monolayer of such ball lenses, a much larger FoV can be obtained, and the distribution and density of TILs can be determined. Such cellphone microscopy can be used to diagnose diseases *in vivo* in principle.

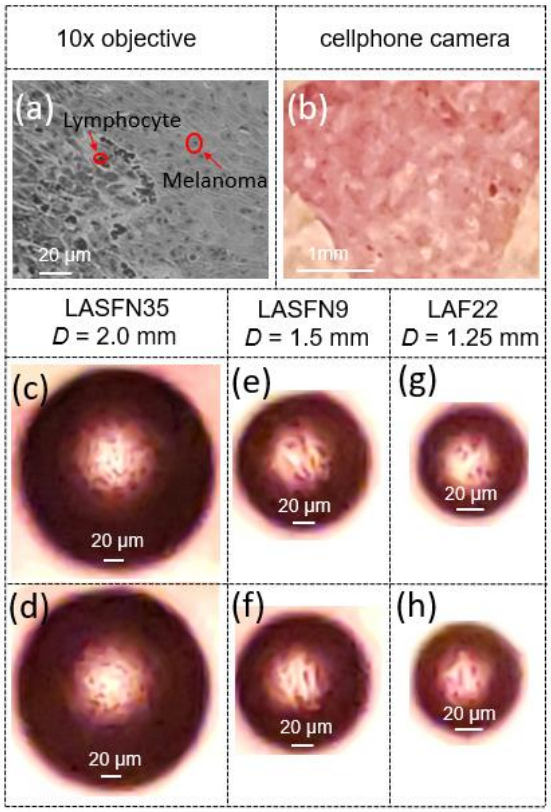

Figure 4.19: Images of Melanoma sample taken by (a) 10x standard microscope objective and (b) ordinary cellphone camera, (c) and (d) taken by cellphone camera through *D* = 2.0mm LASFN35 ball lens, (e) and (f) taken by cellphone camera through *D* = 1.5mm LASFN9 ball lens, (g) and (h) taken by cellphone camera through *D* = 1.25mm LAF22 ball lens.

We introduced the magnification through contact ball lens according to geometrical optics formula 4.2 in Fig. 4.11. According to the original formula 4.1 of magnification through ball lens with a certain gap from the object, the magnification is reduced compared to contact ball lens case. The relationship between the magnification and the refractive index contrast of ball lens with diameters D = 1.0mm and 2.0mm when the gap g is varying from 0 to 0.25 mm is shown in Fig. 4.20. For a ball lens with certain diameter, the ball lens will first form a virtual image of the object and then form a real image when the refractive index contrast of the ball lens is increasing. The threshold refractive index contrast describing a transition from virtual to real imaging is determined by the diameter of the ball lens and the gap between the ball lens and the object, and the magnification through the ball lens can be extremely high when the refractive index contrast is close to this threshold value. As we demonstrated previously in Fig. 4.11 for contact ball lens, this threshold value is n' = 2. However, in our biomedical samples the coverslips have a thin top cover layer to prevent the oxidation of samples. The thickness of this top cover layer is ~200μm that creates a gap between the object and ball lens. As a result, the threshold n' is shifting to the smaller values as such gap is increasing. In our case, the LASFN35 ball lens cannot provide a significant magnification anymore. This indicates that for the ball lens made by any materials, an extremely large magnification, which is required for improving the resolution of cellphone camera, can be always achieved by designing certain diameter of the ball lens and the gap between ball lens and object. For biomedical samples we purchased as object, a refractive index contrast between 1.6 and 1.7 is expected to achieve much higher magnification.

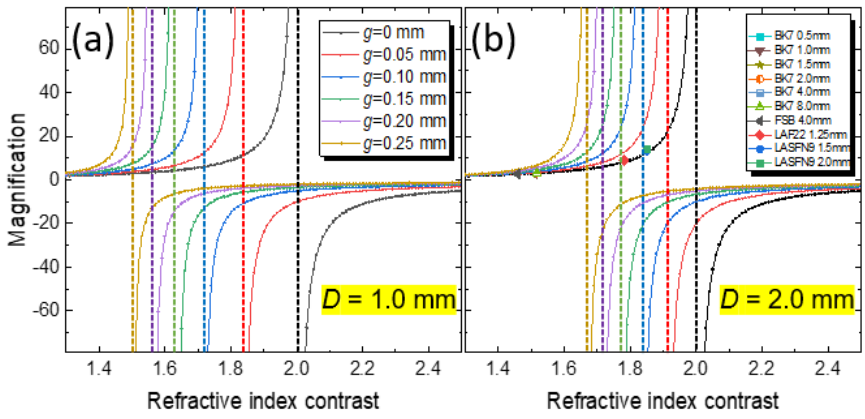

Figure 4.20: (a) and (b) Image magnification through ball lens changing with the refractive index contrast between ball lens and enviroment with diameter D =1.0mm and D =2.0mm and gap g varys from 0 to 0.25mm limited by geometrical optics, the dashed lines are indicating the positions of n'.

Fig. 4.21 shows a collection of images of four different biomedical samples taken by 10× standard microscope objective, by ordinary cellphone camera, and by cellphone camera through D = 2.0mm LASFN35 ball lens. The detailed structure in several micron scale of biomedical samples can be clearly seen by 10× objective, but they cannot be resolved at all by ordinary cellphone camera itself. With a simple ball lens placed on top of the sample, an additional magnification of about 7 times is added to cellphone camera imaging and small structures such as blood cells can be resolved. In our previous studies of magnification and resolution, we illuminated samples from below. However, illumination of the samples based on transmission microscopy cannot be used in most of biomedical applications. To solve this problem, we also took images of the biomedical samples when the illumination is provided from 30° to normal direction and scattered by the sample. Apparently, this way of illumination provided sufficiently bright illumination for the label-free cellphone imaging. This method of illumination can be used in practical

situations for diagnostics of the skin cancers. In addition, we found that significantly larger FoV ~200μm can be realized in the case of oblique illumination in comparison with the transmission mode that can be also helpful factor for developing diagnostics of melanoma.

The detailed imaging of biomedical samples by ordinary cellphone camera with ball lens proves that there is a great resource for increasing the resolution of the optical system. The samples used in our studies were stained with dyes that certainly enhanced their optical contrast properties. Still, the optical contrasts were far below the maximal contrasts available with our nanoplasmonic samples. Generally, this means that the resolution values available with the biomedical samples can be inferior to the diffraction-limited resolution values obtained in our work with the nanoplasmonic structures. In real cases of in-situ melanoma diagnostics in the environment of the doctors' offices, the staining with dye molecules is also not possible which means that the optical contrasts and the corresponding resolution values can be further reduced. These properties require further studies which go beyond the scope of our work. However, our results open the path to developing such diagnostics performed directly on the patient's skin. We predict that under conditions of direct contact between the ball lens and the patient's skin the maximal magnification values can be achieved by using ball lenses with index sufficiently close to two similar the LASFN35 glass ball lenses used in our work.

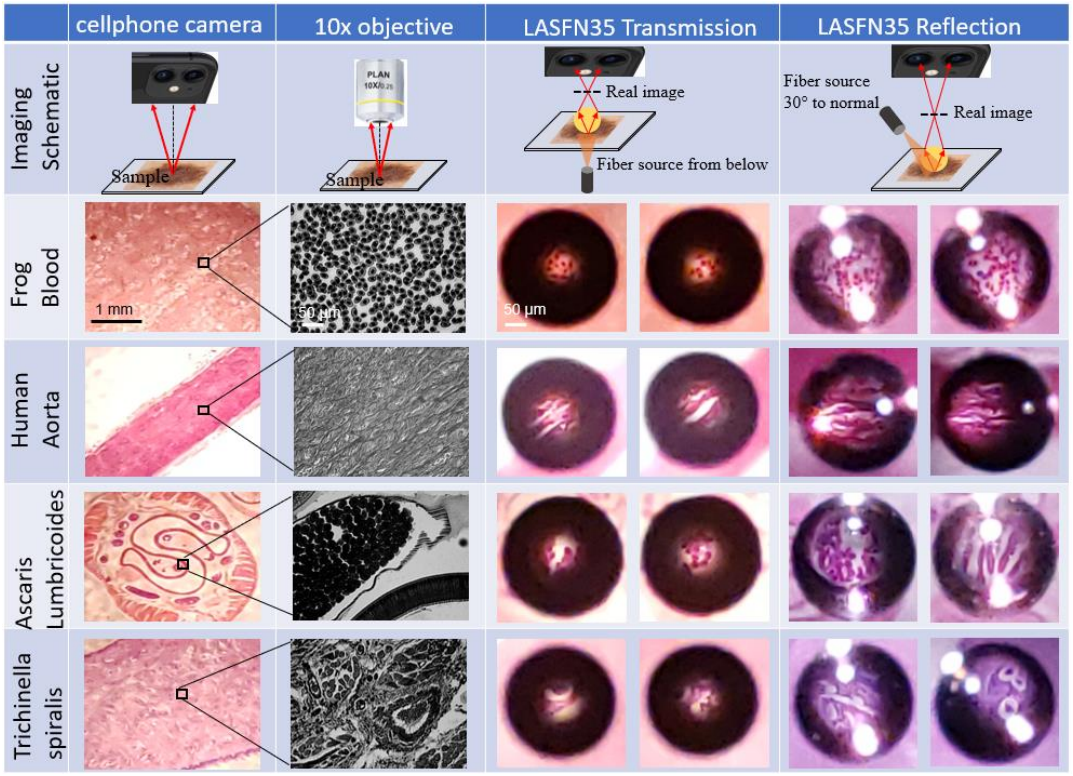

Figure 4.21: Images of four biomedical samples by 10x standard microscope objective (first column), by ordinary cellphone camera (second column), and by cellphone camer through D = 2.0mm LASFN35 ball lens placed at three different locations on the sample in transmission illuminating mode (third and forth column) and in reflection illumintating mode (fifth and sixth column). The scale bars are the same for each column.

4.6 Conclusions

The resolution of a cellphone camera objective is limited by the finite pixel size, and an additional magnification is required for improving the resolution. In previous works [276,277], only a limited magnification was provided by two lens systems separated from objects by millimeter-scale distances. In this work, we developed an alternative approach to high-resolution cellphone microscope based on placing ball lens in a close contact position with object. Cell-scale structures can be resolved in

histological samples by cellphone camera, and in principle it allows diagnosis of the skin diseases *in vivo*. Preliminary results were shown in Refs. [235-237].

We studied how magnification of such systems depend on various parameters based on paraxial approximation of geometrical optics. Our analysis showed that maximizing the magnification requires use of the ball lenses with index of refraction sufficiently close to two in situations when the ball lens is placed in contact with the objects. We were lucky to identify the ball lenses (LASFN35) with the index of refraction sufficiently close to two in the visible region of spectrum and with sufficiently high quality of the sidewall surface. In our work, we realized for the first time the fine tuning of the index of refraction in the proximity of index 2 for imaging applications. It was achieved by using dispersive properties of the glass material via changing the color of illumination. The main trends and dependencies on the external parameters are found to be in a qualitative agreement with the experiment. At the same time, we demonstrated that the experimental magnification values are approximately 3 times smaller than that predicted by the geometrical optics. We qualitatively explained this difference by a significant role of spherical aberrations introduced by the contact ball lenses. We showed that the maximal magnification values achievable in our experiments are sufficiently high (up to 50×) to dramatically increase the resolution of the cellphone imaging.

Using nanoplasmonic structures with the maximal possible optical contrast properties, we demonstrated wavelength-scale resolution of the cellphone imaging through the ball lenses with the refractive index close to two placed in contact with the objects. The resolution quantification is performed by using a comparison with calculated images based on a Houston resolution criterion. The wavelength-scale resolution

observed in our work far exceeds any results obtained using cellphone imaging previously. It creates a basis for further resolution improvement and for developing applications of this technology in biomedical imaging, especially, for *in-vivo* diagnostics of skin diseases such as melanoma.

The applications of the proposed technology for developing practical in-situ melanoma diagnostics directly in the doctor's office without a need to make histological samples might be possible, but it requires meeting two challenges.

First is related to a practical quality of imaging available in living biomedical samples without staining. Certainly, the level of the optical contrasts is expected to be significantly lower compared to stained samples and, especially, to nanoplasmonic samples studied in our work. As a consequence, the quality and resolution of the optical images can be somewhat reduced compared to the results presented in this work. On the other hand, the presence of the top cover layer in histological samples used in our work was clearly a suboptimal factor in our studies because it additionally reduced the magnification values. The leaving skin can be inspected under a direct contact with the ball lens with the index of refraction close to two that should significantly increase the magnification. These studies go beyond the scope of the present Ph.D. theses work, but we plan to perform such studies in our future work.

The second challenge is related to the limited FoV offered by the imaging through individual ball lenses. It should be noted that there is a fundamental tradeoff between the magnification and FoV inevitable in the optical microscopy systems. FoV around 25 μm for 2 mm ball lenses achieved in our work can be insufficient for developing practical applications. The situation can be improved by translating the ball lens using an

automated setup which would allow taking many overlapping images and using a software which would allow stitching individual images to extend FoV. An alternative approach to this problem can be based on making “superresolution coverslips” containing a large number of ball lenses used as a superlens array. This approach is described in more detailed way in the next Chapter.

CHAPTER 5: MANUFACTURING AND APPLICATIONS OF ARRAYS OF MICROSPHERES

5.1 Introduction

As introduced in Chapter 4, super-resolution imaging through contact microspheres emerged several years ago as an unprecedentedly simple method of label-free microscopy by white light with a 2-3 times higher resolution compared to standard microscopy [38,39,42]. Although the method has been successfully demonstrated for examining the inner structures of cells and label-free imaging of virus and proteins, its applications in biomedical microscopy are severely restricted due to the fact that imaging trough individual microspheres has a FoV limited by approximately a quarter of the diameter of the sphere as we discussed at the end of chapter 4. Due to spherical aberrations, only the central part of the virtual or real image produced by the individual microsphere appears to be of sufficiently high quality. Actually, only this central part near the point where the sphere touches the object is visible since the area outside this central circle appears too dark and out of focus. The size of this effective central area is inversely proportional to the magnification through the microspheres and therefore, there is always a tradeoff between the magnification and FoV of imaging through the microsphere.

In order to scan larger area of the samples, people suggested translating microspheres by the tip of atomic force microscope (AFM) [205] or by optical tweezers [206]. Assembling a monolayer of microsphere array to provide simultaneous imaging of a wide area of object through different microsphere is a novel approach to solve the

problem of limited FoV. Assembling monolayer of microspheres can be achieved by 3-D printing the array by laser scanning on photoresist [207,208], self-assembling of small microspheres in suspensions by the force provided by evaporating of liquid [209-214] and manipulating microspheres by optical tweezers [215]. The advantages and disadvantages of each method considering the application of imaging have been discussed in Chapter 1.

In this dissertation, we plan to continue exploring a new fabrication concept aimed at obtaining highly ordered arrays of microspheres by air suction though microhole arrays recently proposed by Professor Astratov's mesophotonics laboratory at UNC-Charlotte [13,71, 223, 234]. The basic principle of fabrication is based on using a forced assembly of microspheres instead of relying on self-assembly or template-controlled assembly of microspheres. Methods of self-assembly inevitably result in a certain concentration of local defects, interstitial microspheres, clusters or domains with different crystallographic orientation and all other types of defects. Although the concentration of defects can be somewhat reduced in structures obtained by the template-directed, electric field-directed or other types of directed self-assembly, the presence of disorder is inevitable in such structures and the concentration of defects is sufficiently high reaching several percent. In contrast, suction assembly proposed and realized for the first time for the obtaining massive scale arrays of microspheres in the Astratov's lab at UNC-Charlotte microspheres allows obtaining almost "perfect" arrays with concentration of defects with can be reduced below 10^{-4} level or even lower.

The basic principle of this assembly which separates it from any other known methods is the fact that position of each microsphere is determined by very strong local forces originating due to air flux through a pre-fabricated microhole array. The principle

of such “suction action” is well known and widely used for holding individual items by vacuum tweezers or suction grippers. However, to the best of our knowledge, it has never been applied for making large-scale arrays of microspheres. This idea has been realized for the first time in the Astratov’s lab at UNC-Charlotte [13,71, 223, 234].

A perfectly ordered microhole array on the opening of a vacuum chuck is shown in Fig. 5.1(a). The microhole array has the diameter of holes slightly smaller than the diameter of the microspheres so that the microspheres cannot be transmitted through the holes, and a pitch arranged as the way we designed for the microsphere array. A vacuum is applied and there is a force of air suction through the microholes. If we put the vacuum chuck with microhole array close to the randomly distributed microspheres, the air flux will elevate individual microspheres from the substrate and position them inside the microholes in such a way that each microsphere occupies one microhole. Therefore, a perfectly ordered microspheres array sitting on microhole array can be obtained.

During the air suction, the dominant force is determined by the flux of air, however there are other forces which in principle can also play some part in such process. These include coulomb interaction between charged microspheres and Van der Waals forces between microspheres. General picture of such assembly is rather complicated, but it can result in some of the microspheres residing on top of the microspheres sitting in microholes. It can also be viewed as formation of the second (or even the third) layer of microspheres. Those additional layers can be removed by applying air flux in a horizontal direction to blow them off while the air suction on vertical direction is still applied to hold the first layer of microspheres shown in Fig. 5.1(b). After removing the multiple layers of

microspheres, the monolayer of perfectly ordered microsphere array is obtained on top the microhole array shown in Fig. 5.1(c).

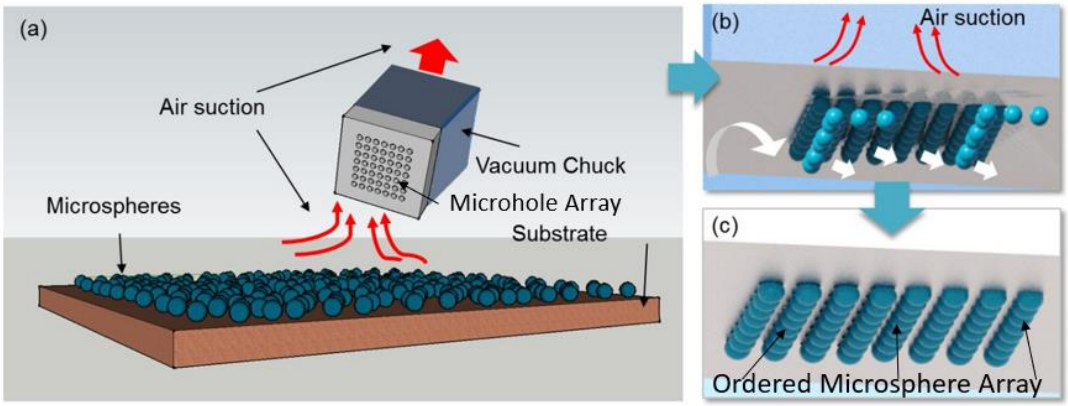

Figure 5.1: (a) Applying suction through a micro-hole array as a force to assemble the microspheres in the holes. (b) Blowing away interstitial spheres by an additional flux of air parallel to the substrate, and (c) Perfectly ordered single monolayer of spheres sitting in microholes. [13]

In this chapter, we study the suction assembly at a completely different level compared to previous studies [13,71, 223, 234]. Previously, the array of 45 μm microholes was obtained by etching through a Si wafer lapped down to 170 μm [13]. It was a good way to demonstrate the concept, but the fabrication method was found to be impractical because the wafer was mechanically weakened by the presence of microhole array, and it was too fragile. In fact, the fabricated structure was quickly cracked. In our work, we decided to switch to microhole arrays obtained by better established technologies in materials with more mechanically stable properties such as metals. We ordered microholes arrays with different diameters and pitch sizes and microspheres made by different materials with different diameters from commercial production companies, assemble them into microsphere arrays using the air suction approach introduced above, and preserve them permanently by embedding them into plastic coverslips depending on future applications.

The process of embedding microsphere in plastic coverslips was developed previously in the Astratov's laboratory for randomly assembled microspheres [40], however it was not applied to ordered arrays. It required developing a special procedure of transferring ordered arrays of microsphere obtained by the suction assembly into a thermal press. We prove that such arrays of microsphere superlenses can extent FoV of imaging due to observation through multiple microspheres. We also show that such microsphere array made by high index (n ~ 1.9) materials can be used as retroreflectors.

5.2 Assembling monolayer of microsphere by air suction

To assemble microsphere arrays by using air suction, the first task is to obtain microhole arrays with different diameters and pitch sizes. We proposed to assemble 2-D hexagonal arrays of microspheres shown in Fig. 5.2 to achieve compact arrangement of microspheres with smaller gaps. The two major parameters which determine the design of microhole array is the diameter of the holes (D) and the center-to-center distance between two neighboring holes (P). The diameter D is smaller than the microspheres to prevent passing through the holes, and the pitch P is slightly larger than the diameter of the microspheres to provide compact arrangement with the minimal gaps.

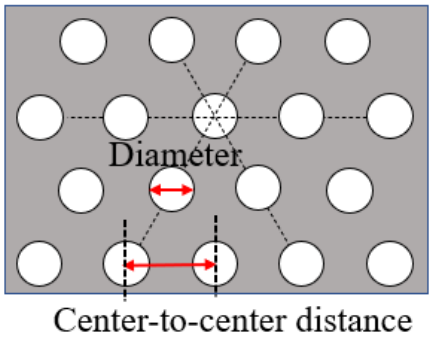

Figure 5.2: Design of 2-D hexagonal arrays microholes for assembling microsphere arrays.

Table 5.1 List of microhole arrays with different dimensions obtained from Micron Laser Technology, Potomic Photonics Inc, and Mechanical Department at UNC Charlotte.

Laser burning at Micron Laser Technology		
Diameter (μm) (*D*)	Center-to-Center distance (μm) (*P*)	Thickness of sheet (μm) (*t*)
30	70	100
50	100	178
250	350	125
300	600	178
600	900	200
900	1200	178
Laser burning at Potomic Photonics Inc		
Diameter (μm) (*D*)	Center-to-Center distance (μm) (*P*)	Thickness of sheet (μm) (*t*)
25	75	100
Mechanical Drilling at UNC Charlotte		
Diameter (μm) (*D*)	Center-to-Center distance (μm) (*P*)	Thickness of sheet (μm) (*t*)
900	1200	250
900	1200	400

We purchased the microhole arrays with different dimensions from commercial production companies. There are two major fabrication techniques of microhole arrays: laser burning and micromechanical drillings. The microhole arrays obtained by laser burning technique were ordered from Potomac Photonics Inc. and Micron Laser Technology. From the former company, we obtained microhole arrays fabricated on thin Aluminum sheet with diameter of holes varying from 30μm to 900μm. From the later company, we obtained microhole array with diameter of 25μm. In order to test micromechanical drilling method, we ordered microhole arrays fabricated in brass

platforms using high-precision automated drilling machines at the Center for Precision Metrology affiliated with Mechanical Engineering Department at UNC Charlotte. These structures were designed to accommodate ball lenses with 1 mm diameter, and we ordered several arrays with the 900 μm diameters of microholes. The detailed parameters of microhole arrays ordered from different manufacturers are listed in Table 5.1.

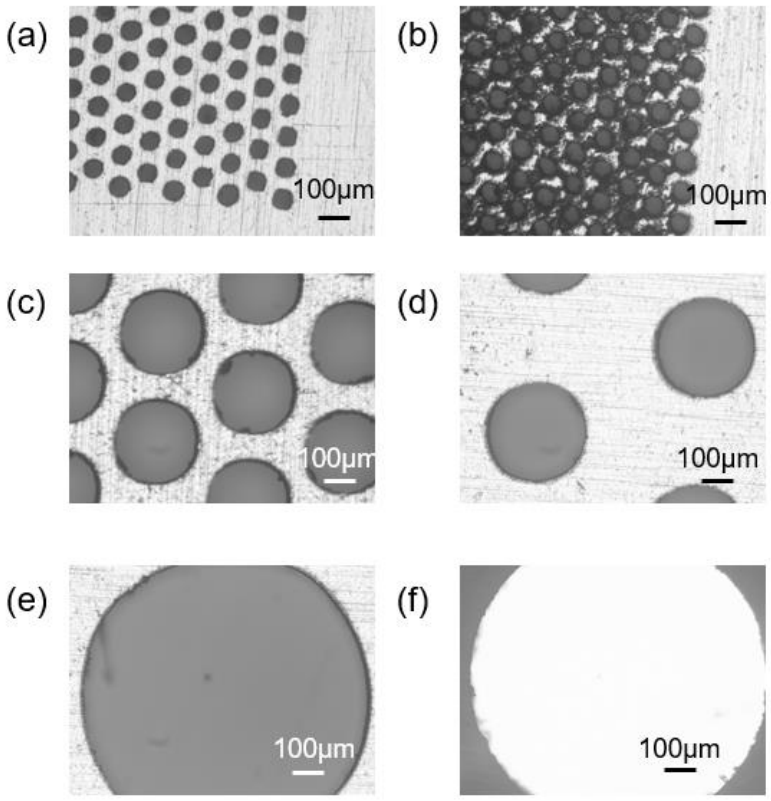

Figure 5.3: (a) and (b) Back-side and front-side of laser burning microhole array with D = 50μm, respectively. (c), (d) and (e) Back-side of laser burning microhole array with D = 250μm, 300μm, and 900μm, respectively. (f) Machinal drilling microhole array with D = 900μm.

The images of the microhole arrays obtained by a conventional upright optical Mitutoyo 378-730 microscope with 5× objective is shown in Fig. 5.3. Laser burning techniques use the high heat of laser to burn microholes through metal sheet, which causes damages to the front-side of microhole arrays where the laser first reaches the metal sheet

and only leave a clean and smooth surface with accurate dimensions of microholes on the backside of arrays with small diameters of the holes shown in Fig. 5.3(a) and 5.3(b). For larger diameters of $D = 250\mu m$, $300\mu m$, and $900\mu m$ in Fig. 5.3(c)-5.3(e), the front and back sides of the arrays are both clean and smooth with good accuracy of the dimensions. Fig. 5.3(f) shows that the smoothness and accuracy of mechanical drilling techniques is also good enough. The images of the microhole arrays fabricated by two different methods are shown in Fig. 5.4.

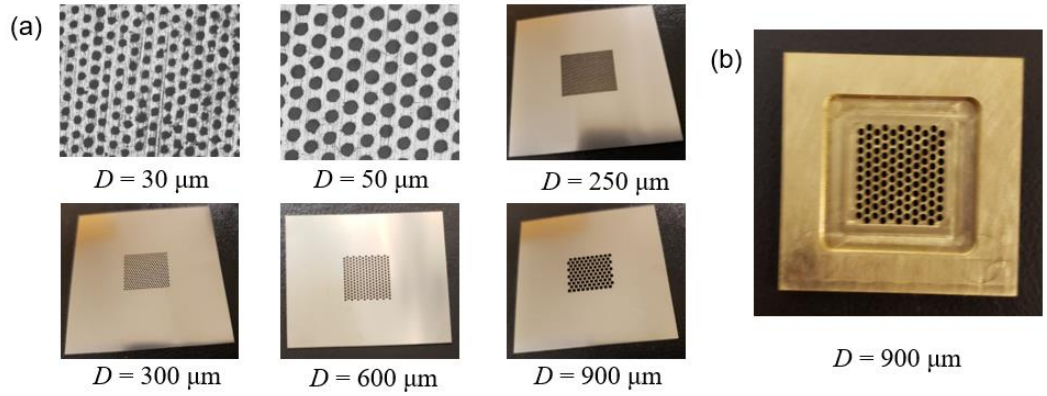

Figure 5.4: (a) Images of microhole arrays with different dimensions by laser burning. (b) Image of microhole array by mechanical drilling.

After obtaining the microhole arrays, we purchased microspheres with different refractive index and range of diameters to fit microhole arrays with different dimensions from Mo-Sci Corporation, Cosepheric LLC, and Swiss Jewel companies. The Mo-Sci Corporation and Cosepheric LLC sale microspheres with larger range of diameters with relatively low uniformity with the typical size variations about 10-15%. These companies are interested in selling microspheres for applications requiring large quantities. In contrast, The Swiss Jewel Company produce ball lenses individually for applications requiring smaller quantities, but with higher uniformity and quality of the surface. These ball lenses

have millimeter-scale diameters, and they are individually polished providing the best surface quality among all other manufacturers. We are interested in microsphere made by different materials since they are supposed to provide different magnification of the object, which was introduced in Chapter 4, and we are interested in the properties of microsphere array with high refractive index of n ~1.9 as retroreflectors. We purchased soda lime microspheres with low index of 1.46 and microspheres with high index from 1.77 to 2.02, and the list of the microspheres used in our studies as well as the list of the corresponding microhole arrays are shown in Table 5.2.

Table 5.2: List of purchased microspheres with materials, refractive index, manufacturer, and the corresponding dimensions of microhole arrays to fabricate monolayer of them. (BTG is the abbreviation of Barium Titanate Glass)

Material	Refractive index	Manufacturer	Diameter (μm)	Diameter of corresponding microholes (μm)
Soda lime	1.46	MO-SCI	90 ± 10%	50
Soda lime	1.46	MO-SCI	300 – 350	250
Soda lime	1.46	MO-SCI	500 – 600	300
Soda lime	1.46	Cospheric	800 ± 2%	600
Soda lime	1.46	Cospheric	1010 ± 2%	900
BTG	2.1	MO-SCI	63 ± 7%	30
BTG	1.9	MO-SCI	75 - 90	50
BTG	1.9	Cospheric	300 - 350	250
BTG	1.9	Cospheric	500 - 600	300
BTG	1.9	Cospheric	710 - 850	600
Sapphire	1.77	Swiss Jewel	1000 ± 0.25%	900
LASFN9	1.85	Swiss Jewel	1000 ± 0.25%	900
LASFN35	2.02	Swiss Jewel	1000 ± 0.25%	900

With the microspheres and microhole arrays ready, we assembled the microsphere arrays by using air suction through microhole arrays. Fig. 5.5 shows the experimental setup for assembling monolayer of microspheres. They were distributed randomly in a dish, and the microhole array was placed on top of the opening of the vacuum chuck. The whole

setup of vacuum chuck and microhole array was moved close to the dish with microspheres, and they were elevated from the dish by the air flux and positioned in the microholes as illustrated in Fig. 5.5(b)., After completing the assembly of microspheres in the microhole array, an air flux is applied in horizontal direction from the left to blow away the additional microsphere layers while the vacuum below is still turned on to hold the first layer of microspheres. By controlling the intensity of air blowing, the additional layers were successfully removed, leaving a single layer of microspheres sitting in the pre-fabricated microholes.

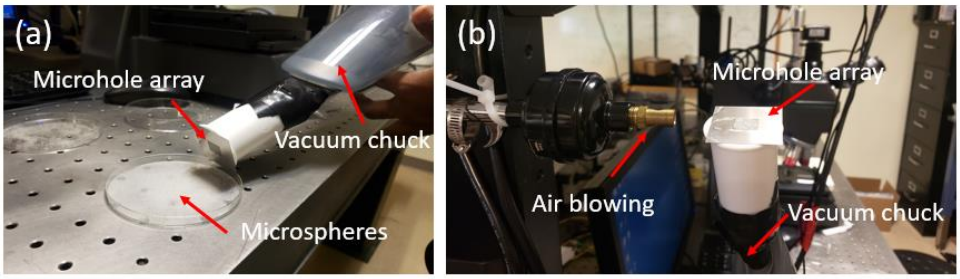

Figure 5.5: (a) Assembling microspheres on top pf microhole arrays by air suction from vacuum. (b) Removing additional multi-layers of microspheres by air blowing in horizontal direction.

Fig. 5.6 shows the assembled monolayer of microspheres positioned in microhole arrays with different geometrical parameters. We found that the quality of ordering (concentration of defects) generally depends on the average diameters and on the size uniformity of microspheres. Perfect assembly results were obtained for 1 mm individually polished microspheres with very small size dispersion (a few percent size uniformity). They are represented by the sapphire, LASFN9 glass, or LASFN35 glass ball lenses, as illustrated in the top left image in Fig. 5.6. The other three images of microsphere arrays with smaller diameters made by soda lime glass or BTG appear less uniform due to the size nonuniformity (~10-15% size dispersion) and some problems with quality of individual

spheres (some of them are chirped or damaged). Regardless of the quality of microspheres, it is shown that such fabrication method of assembling monolayer of microspheres by air suction through microhole arrays is an efficient and simple method for diameters of microspheres larger than 200μm. For smaller microspheres with a diameter less than 100μm, we found a tendency for microspheres to densely populate the holes in the central section of the microhole array whereas leaving unfilled some holes closer to the edge of the microhole array. The general explanation of some difficulties with assembly smaller microspheres are related to the fact that the gravity and air suction forces are rather macroscopic in nature and tend to dominate the behavior of larger ball lenses. Whereas for smaller microspheres the other factors such as electrostatic forces due to charging effects and Van der Waals forces play increasingly important role. The latter forces, however, tend to stimulate aggregation of microparticles that is a negative factor for achieving best results by the suction assembly. In addition, it is much more difficult to remove the additional layers by air blowing for microsphere array with smaller diameters. In most of the cases, we found that the proposed method is suitable for assembling microsphere arrays with diameters larger than 200 μm.

One of the applications for such microsphere arrays is to create a superlens array with enlarged FoV due to imaging through multiple microspheres. Such imaging requires contact of multiple microspheres to the object at the same time. For larger microspheres with a diameter of 1000 μm sitting in the microhole array, the bottom of the microspheres should extend out of the metallic microhole array to make a contact with the object below. It can be realized by reducing the thickness of the metallic microhole array. If such "protruding" of microspheres through the microholes is not possible that can be the case

for smaller microspheres, the only way of making superlens array would be related to transferring the microspheres sitting in the holes on a different substrate. In this case, we have to transfer the microsphere array from the microhole array to some substrate that can permanently hold the microspheres and expose some fraction of the microspheres ("tips of the ball lenses") to the air and would make possible the physical contact of these "tip" with the object. In our work, it was achieved by embedding of microspherical arrays into the transparent plastic coverslips [13].

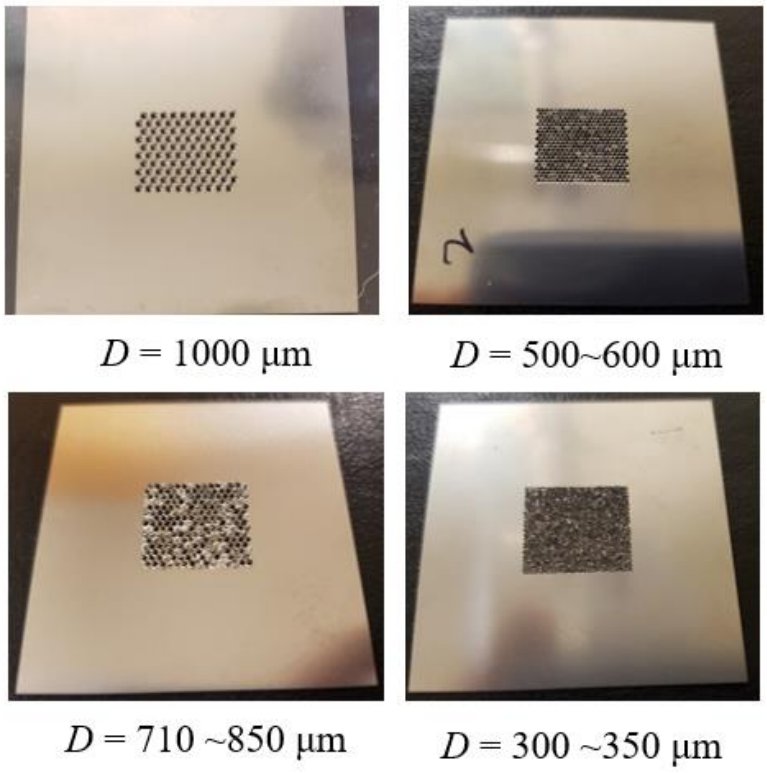

Figure 5.6: Assembled monolayer of microspheres on microhole arrays with different dimensions, *D* refers to the diameter of the microspheres.

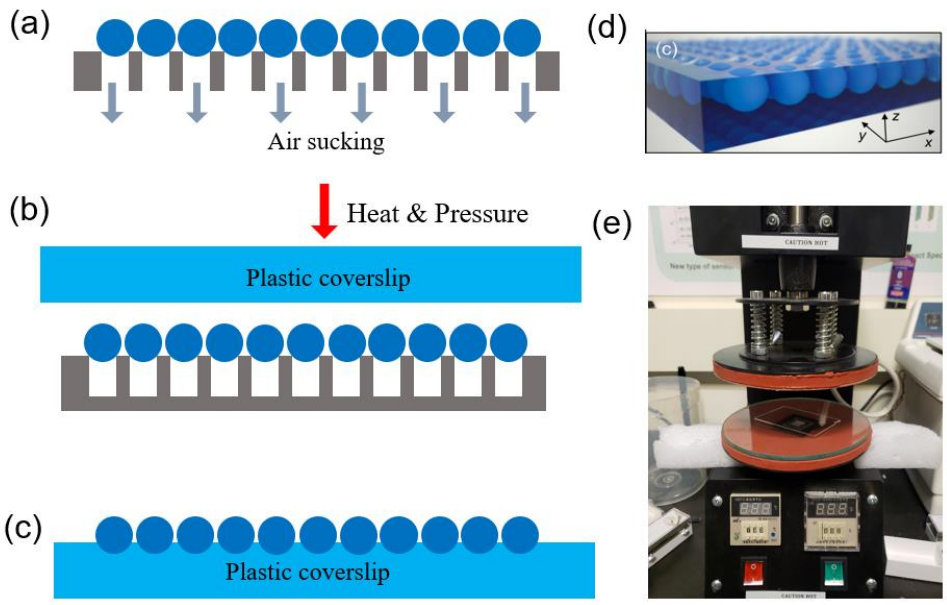

Figure 5.7: (a)-(c) Procedure of embedding the microsphere array into plastic coverslip by applying heat and pressure. (d) Illustration of perfectly ordered microsphere array embedded in coverslip with same extension height. (e) The hot plate which can provide heat and pressure.

Fig. 5.7 shows the procedure of embedding the microsphere array into plastic coverslip by applying heat and pressure. We obtained microsphere arrays sitting in the microholes with each microhole filled with just a single microsphere, see Fig. 5(a). After that, microspheres were partly embedded in the pre-heated plastic coverslip with a softening temperature around 165° - 180°C, as illustrated in Fig. 5.7(b). This step was important because it allowed us to obtain a transferrable structure which can be turned upside down and placed inside the thermal press, as illustrated in Figs. 5.7(b-e). Thus, embedding microspheres was a two-step process. First, the microspheres were “glued” to the pre-heated coverslip as shown in Fig. 5.7(b) and after that the whole structure was loaded in the thermal press to increase the depth of embedding. We obtained two coverslips with different thicknesses: 240 μm thickness Rinzl plastic coverslips form Electron

Microscopy Sciences for embedding microspheres with diameter of 300~350 μm, and 500 μm Rinzl plastic coverslips form Fisher Scientific for embedding microsphere with diameter of 500~600 μm. The heating was performed to 160°C for 5 mins in the case of 240μm thickness coverslips and for 10mins in the case of 500μm thickness coverslips. The mechanical pressure was applied by the springs of the thermal press at a fixed level which was quite modest, but it was not quantified. After cooling for 10mins to solidify the coverslip, an ordered microsphere array embedded in coverslip was obtained. The microspheres in thus obtained samples were slightly extending from the plastic slabs. The amount of extension was dependent on the temperature and duration of the embedding process. It was rather difficult to control, but in most cases, it was about several tenths microns that allowed to achieve a contact condition with the samples under study.

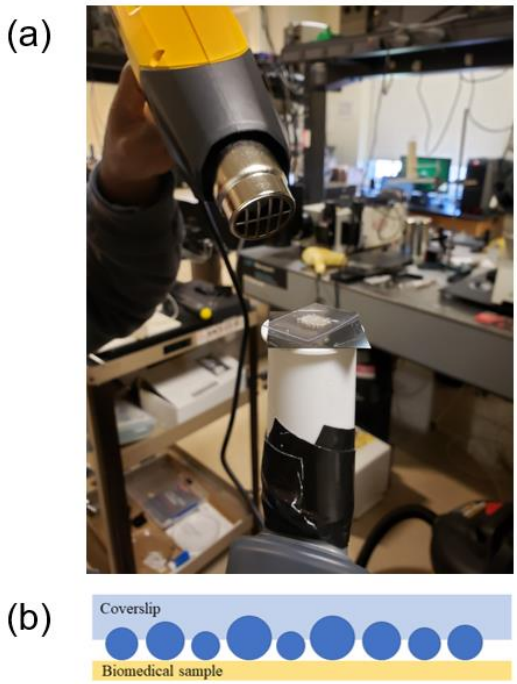

Figure 5.8: (a) Using hot gun to adhere coverslip to microspheres to avoid losing microspheres by static electricity. (b) Microspheres with variable sizes embedded in coverslip with different depth and have same extension to be in contact with the object at same time.

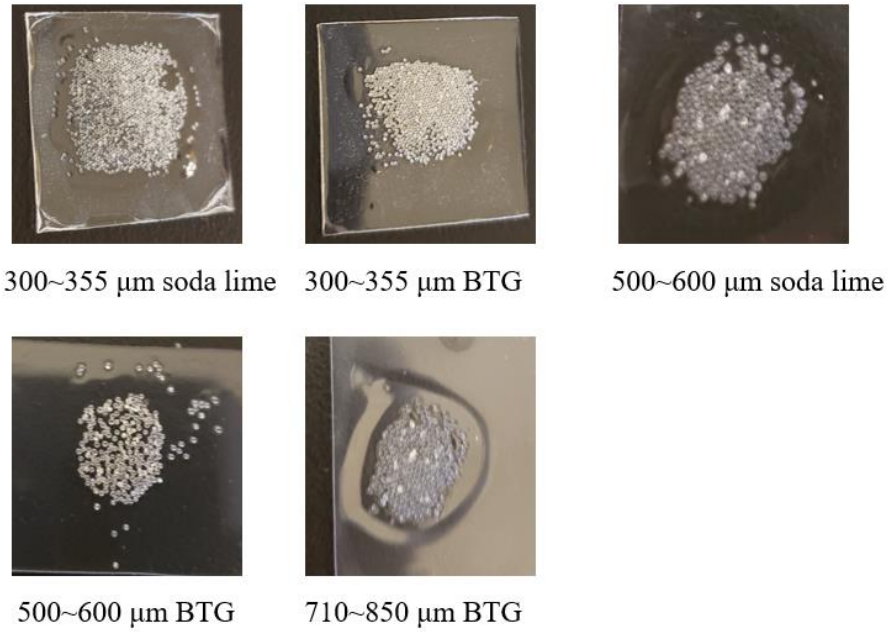

Figure 5.9: Embedded microsphere arrays with different diameter and refractive index.

During this embedding process, some problems were identified. Since there is a strong static electricity between plastic coverslip and microspheres, if we place the coverslip on the microsphere array directly, the microspheres will be attracted and move randomly instead of being kept in the positions by the microholes. So, as described earlier, in real fabrication, we had to apply a two-step embedding procedure. Let us describe this procedure in a more detailed way here. We first had to place the coverslip on top of the microspheres with the air suction on so that the microspheres are held by the air suction. After that we used a hot gun to heat the coverslip up to its softening temperature, so that the microspheres adhere to its surface as shown in Fig. 5.8(a). Only after that we transferred the coverslip attached to the hot plate inside the thermal press to further embed the microspheres and flatten the coverslip. The microsphere arrays with different diameters of microspheres embedded in the coverslip with variable thicknesses, are illustrated in Fig.

5.9. These examples illustrate our initial results showing the presence of disorder. The quality of assembly was gradually improved by adjusting heating and mechanical pressure conditions.

The 300~355μm soda lime microsphere array with index of 1.46 and BTG microsphere with index of 1.9 were embedded in coverslip with thickness of 240 μm. The 500~600μm and 710~850μm microsphere array were embedded in coverslip with thickness of 500 μm. We had only a limited number (several hundreds) of ball lenses with 1000μm diameter formed by high quality LASNF35, LASFN9 glasses and sapphire. We decided not to embed them into coverslip to avoid losing them. Luckily, the microhole arrays for assembling such arrays were sufficiently thin, so that after positioning of ball lenses in microholes their tips extended outside the microholes from the opposite side of the arrays. This allowed us to use these superlens arrays directly without embedding them in the plastic coverslips.

5.3 Imaging through monolayer of microsphere array to enlarge the FoV

The first application we plan to illustrate is imaging through multiple microspheres to enlarge FoV compared to that in the case of using individual microspheres. As we know from Chapter 4, the imaging through a ball lens placed on top of the object is can be achieved as the virtual imaging or as real imaging depending on the parameters of the system. According to geometrical optics, when the refractive index contrast between the microsphere and environment is relatively low ($1.4 < n' < 1.8$), the ball lens forms the virtual image at the plane located below the object. On the other hand, if the index contrast is relatively large, the ball lens forms an inverted real image above the object. The threshold

index contrast where the imaging modality is switching from virtual to real is determined by the refractive index contrast of microsphere and environment, the diameter of the microsphere, and the gap between the microsphere and object. To observe the real or virtual image through ball lens, we have to move the microscope objective up or down to capture the images.

We use a biomedical sample of Frog Blood (Carolina Biological Supply Company) as the object and inspect it under the Mitutoyo 378-730 microscope with 5× NA = 0.14 objective shown in the right corner of Fig. 5.10. After that we place the microsphere arrays with different materials and diameters in contact with the object and focused microscope objective on the real or virtual image (depending on which one was observable) through the microsphere array. We were able to see images of the object at different positions through different microspheres at the same time since the eyepiece of microscope has a wide FoV. Unfortunately, the camera connected to the microscope has a limited FoV and we have to translate the object horizontally to take pictures of images at different positions. Fig. 5.10 shows the magnified images through microsphere array made by soda lime glass (n = 1.46), sapphire (n = 1.77), LASFN9 (n = 1.85), BTG (n = 1.9), and LASFN35 (n = 2.02) with diameter between 300μm to 355μm, 500μm to 600μm, 710μm to 850μm, and 1000μm. We see similar images through microspheres when the object is translated horizontally, and the objective is kept at the same vertical position. That means we successfully embedded the microspheres into coverslip with a very similar amount extension of microspheres from the coverslips shown in Fig. 5.8(b) and found the images through different microspheres at same height. We noted that the images through some microspheres are not very clear, this is because the microspheres we ordered from

Cospheric and Mo-Sci companies had a wide range of diameters and sometimes defects. As an example, we found that some of them are not transparent and some of them are chirped. We also noted that the images through LASFN35, LASNF9 and sapphire which we ordered from Swiss Jewel Company with perfect optical properties are all great at different positions.

It is found that the total magnification of the optical microscope system consists of the ordinary magnification provided by the microscope multiplied by the additional magnification introduced by the contact ball lens. The magnification improvement due to microspheres is noticeable in Fig. 5.10, but its value is limited due to a thin cover layer with the thickness around 200 μm introduced to protect the histological sample. As discussed in Chapter 4, such cover layer reduces the magnification values according to the geometrical optics and prevents collection of the object's optical near field by the microspherical superlens. This means that the resolution improvement is also limited in this case. Some partial improvement is still possible due to potentially larger collection cone offered by the ball lens. However, in any case, the superresolution imaging is not expected in this case.

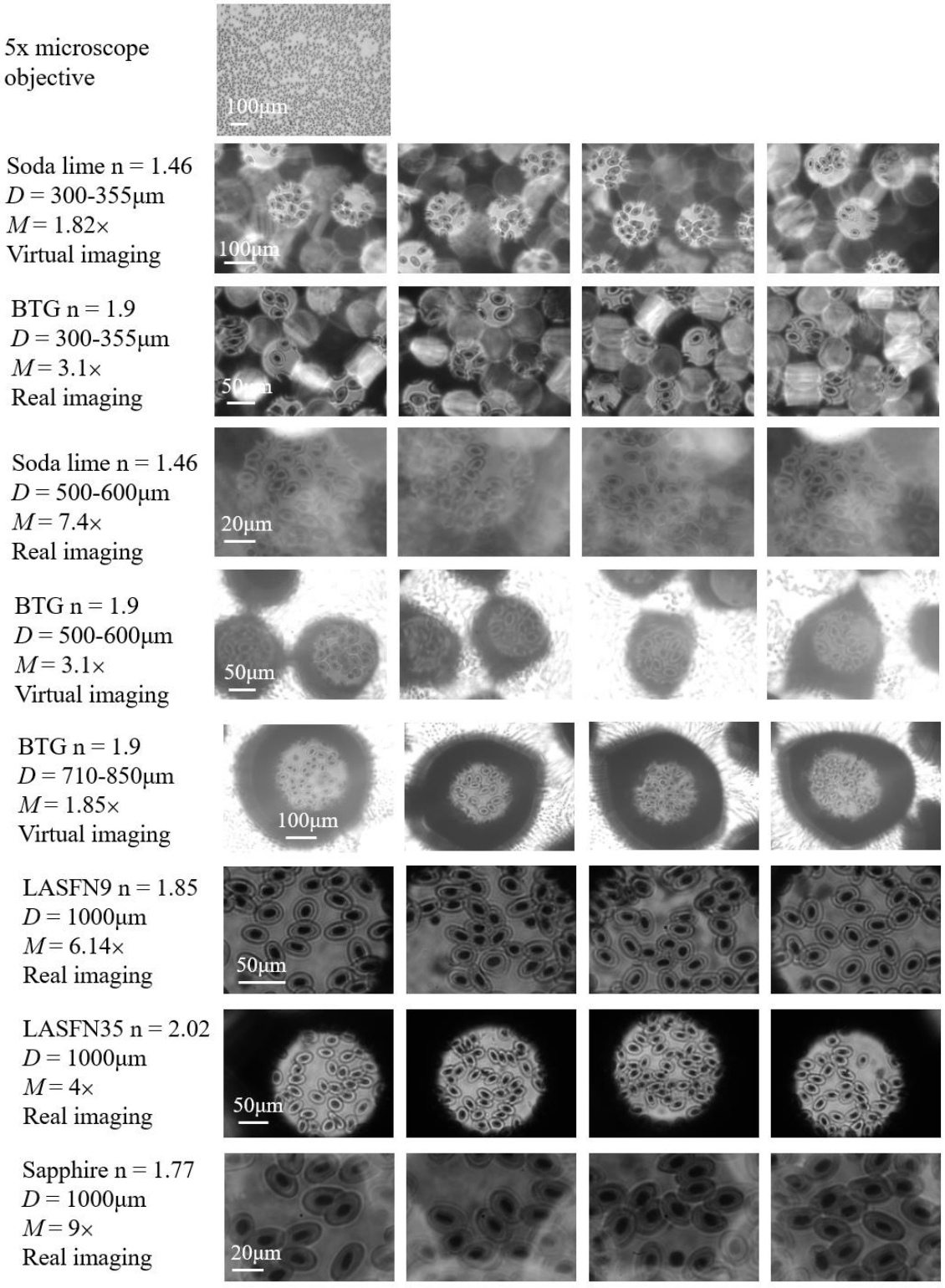

Figure 5. 10: Images of frog blood through embedded microsphere array by different materials and diameters. The measured additional magnifications are labeled.

5.4 High-index microsphere arrays as retroreflectors

The second application we plan to illustrate is building spherical lens retroreflectors [216,217]. An incident light is focused by a spherical lens, and the focusing position is dependent on the refractive index of spherical lens. Lower index of spherical lens tends to focus the light behind the back surface of the sphere. When the index is increasing, the focusing position is moving towards the back surface. For spherical lens which can focus the incident plane wave precisely on the back surface, the reflected light repeats the path of the incident electromagnetic waves in the reverse direction which is equivalent to changing the propagation direction or to time reversal in the Maxwell equations, thus showing retroreflecting behavior.

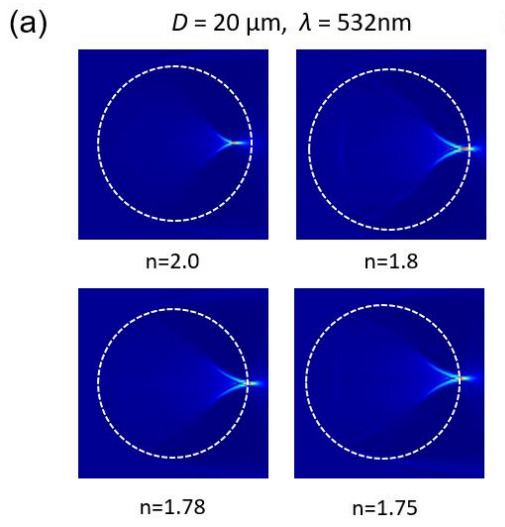

(b)

Diameter (um)	Best index to focus on the back surface
5	1.7
10	1.72
20	1.75
40	1.78
60	1.8
80	1.82

Figure 5.11: (a) Numerical modeling of focusing position of plane wave at λ = 532nm by spherical lens with a diameter of 20µm with a varying refracitve index. (b) The best refracitve index for spherical lenses with different diameteres to focus plane wave excatly on the back surface of the lens.

Fig. 5.11(a) shows how the focusing position of incident plane wave changes with the refractive index of spherical lens. It is seen that there is an optimal refractive index for spherical lens to focus the light exactly on the back surface of the lens, and for larger diameter of the spherical lens, the optimal refractive index is exceeding 1.8 as shown in Fig. 5. 11(b). Here, we are interested in building as optimal retroreflectors as possible by using the microsphere array with the best quality of the surface available to us in this project such as sapphire (n = 1.77), LASFN9 (n = 1.85), and LASFN35 (n = 2.02) ball lenses with the millimeter-scale dimensions.

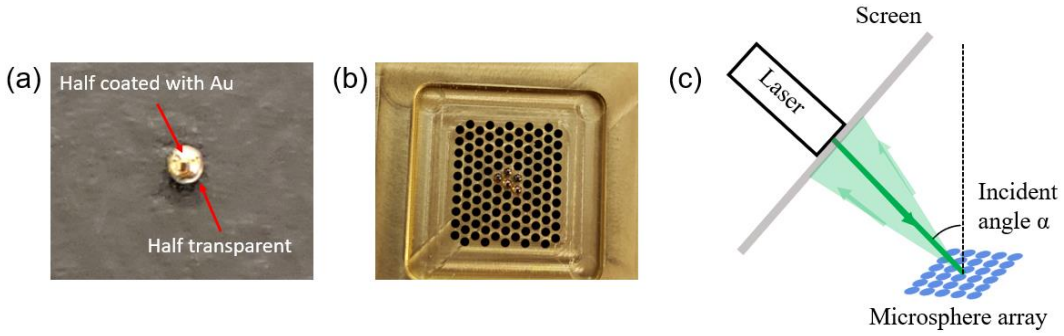

Figure 5.12: (a) and (b) Illustration of single ball lens and array of ball lenses half coated with 100nm Au layer, respectively. (c) Schematic of the setup of retroreflectors.

The retroreflection properties of high index ball lenses can be enhanced by depositing a metallic mirror on the bottom half of the spherical lens [217]. To this end, we placed the ball lenses with varying materials inside microholes and coated the top half of them with a layer of Au with ~100nm thickness in the platter which is thick enough to operate as a mirror. Fig. 5.12(a) and 5.12(b) illustrated the half-coated ball lenses. After that, we flipped the ball lenses upside down to make the incident light pass through the transparent half of the ball lens and to be strongly retroreflected when it reaches the bottom half of the ball lens covered with Au. Fig. 5.12(c) shows the schematic of the setup for

observing retroreflection affect. Three lasers with wavelengths of λ = 420 nm, 532 nm, and 632 nm were used to provide collimated incident beam. The incident angle was tilted to be α = 10°. Half-coated ball lens arrays made by sapphire, LASFN9 glass, and LASFN35 glass was placed in a laser beam and the retroreflecting patterns can be captured by the screen with a hole attached to the lasers.

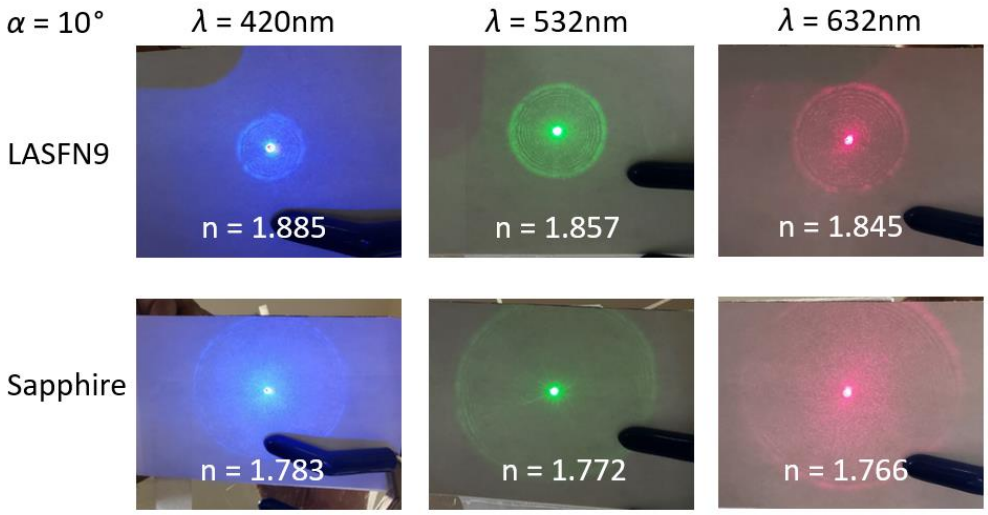

Figure 5. 13: Retroreflecting patterns for LASFN9 and sapphire half-coated ball lens arrays for incident lasers with different wavelength at 10° incident angle. The corresponding refractive index at different wavelengths due to dispersion are labeled on the images.

Fig. 5.13 shows the retroreflected beams produced by the arrays of LASFN9 and sapphire half-coated ball lenses for three different incident wavelengths. The images were captured by the cellphone camera. The retroreflecting properties of LASFN35 array did not display any beams structured around the incident beam. For this reason, this case represents rather scattering of incident beam in a broad range of angles and it is not illustrated in Fig. 5.13. Both LASFN9 and sapphire ball lens arrays showed concentric pattern in a narrow cone centered with the incident laser beam. The intensity and angular width of the retroreflected beam were found to depend on the wavelength of the incident

light. The incident light is represented by a collimated laser beam with very narrow divergence, but the retroreflected beam has a clearly measurable divergence angle. The narrower such cone is, the better the retroreflective property it has. To measure the divergence of the retroreflective cone, we define a half angle of the directionality diagram of the retroreflected beam which can be measured for the experimental geometry illustrated in Fig. 5.12(c). Ideally, measurements of the directionality diagram should be performed by the power meter, and we plan such measurements in our future work. To simplify this characterization, we used the property that the cone of retroreflected beam is in practice terminated rather sharply as it can be seen from inspecting Fig. 5.13. So, we simply measured the angle of such cone based of the sharp circular boundary of the retroreflected beam clearly visible in Fig. 5.13. These results are summarized in Fig. 5.14 which shows that the dispersion properties of the ball lenses play a significant role in the directionality of the retroreflected beam. As we discussed in Chapter 4, the refractive index increases for shorter wavelengths. In both cases of arrays formed by LASFN9 and sapphire spheres use of laser illumination with shorter wavelength causes the “shrinkage” of the directionality of the retroreflected light. This shows that both cases are generally suboptimal and the average index in both cases is smaller than the “optimal” index at any wavelength used in our experiments. The results indicate that the optimal index for the millimeter-scale ball lenses should be slightly higher, probably in the vicinity of n~1.9, however more detailed study with microspheres made from different materials and with different wavelengths are required to realize more optimal situations. Our results show that the retroreflectors can be built with strongly dispersive properties, so that the optimal performance can be reached only in a narrow range of wavelengths. On the other hand, if a more broadband operation

is required, we can remember the typical shape of the spectral dispersion curves for different glass materials. Away from the absorption bands, the dispersion curves flatten which means that retroreflectors with more broadband operation can be designed by selecting microspheres with more optimal index of refraction.

An interesting property of such images is that they form a series of concentric rings reminiscent of Newton rings. This means that some degree of coherency is preserved in the retroreflected beam. In principle, it can be important for such applications where the retroreflecting mirrors are used in systems with the optical feedback properties such as laser resonators.

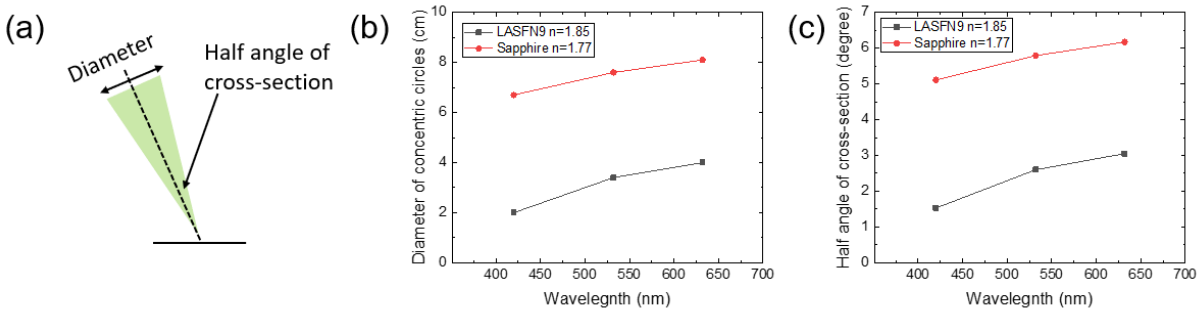

Figure 5. 14 (a) Illustration of the half angle of the cross-section triangle of the retroreflection cone. (b) and (c) The diameter of the concentric circles and the corresponding half angle of the cross-section area for retroreflectors by sapphire and LASFN9 ball lens arrays at different incident wavelengths.

5.5 Conclusions

The approach to building different photonic microstructures based on using suction assembly is extremely attractive since it allows a full control over the symmetry and quality of microspherical arrays which is not available for other methods. In this Chapter we developed initial pioneering work performed in the Professor Astratov's lab to further

develop the main principles of such assembly and to demonstrated two areas of applications of the proposed structures.

First, we successfully assembled 2-D hexagonal arrays containing hundreds of microspheres with variable diameters and different material properties. We ordered microhole arrays with different diameters and pitches and assembled microspheres array by air suction with diameter of 300~355μm, 500~600μm, 710~850μm, and 1000μm made by different materials with refractive index of 1.46, 1.77, 1.85, 1.9, and 2.02. We showed the practical feasibility of metallic microhole arrays fabricated by different technologies such as laser burning and micromachining. Then we used the suction assembly to test how this technology scales with the variation of the sphere diameters. In a preliminary way, we showed that it allows creating perfectly ordered structures for spheres with diameters larger than 200 μm. Our results don't mean that this technology does not work for smaller microspheres. They simply mean that assembly of sufficiently large ball lenses by this technology is practically effortless and can be performed in extremely straightforward way. Use of smaller microspheres might still be possible, but it will require more studies. One factor involved is related to the size disorder and more generally to the uniformity and quality of microspheres. Another factor involved is related to removing charging effects and to using stronger fluxes providing stronger forces for suction assembly.

We successfully embedded the microsphere arrays into plastic coverslips for further applications such as biomedical imaging. We embedded the microsphere arrays with different sizes and refractive index into Rinzl plastic coverslip with thickness of 240μm and 500μm by applying heating and pressure by hot plate and achieved almost complete embedding with only a small section ("tip") of the microspheres slightly extending from

the coverslips. We found that this is a rather convenient situation for the practical use of such coverlips in biomedical applications because it allows a parallel imaging through multiple microspheres that effectively extends FoV in comparison with the imaging through individual ball lenses. To illustrate potential advantages of this technology, we performed imaging of frog blood samples through embedded microsphere arrays with different parameters. We realized an imaging with wide FoV with such samples. The situation was suboptimal in terms of achieving the maximal magnification values and resolution advantages, but it still showed the potential advantages of the proposed technology.

Another application of the suction assembly of microspherical arrays is proposed based on developing retroreflectors with the novel functionality and properties. It is generally known that themicrospheres with high refractive index exceeding 1.8 can be used as spherical lens retroreflectors which are sometimes called “cat eye” retroreflectors. The advantage of such retroreflectors is related to their very broad range of angles. We showed that by using extremely high-quality microspheres with well controlled properties such as precise control of index of refraction due to dispersive effects, the angular directionality of such retroreflectors can be optimized. We successfully coated the bottom half of ball lens arrays with ~100nm thick layer of Au made by high index materials as sapphire (n = 1.77), LASFN9 (n = 1.85), and LASFN35 (n = 2.02). We collected the retroreflective pattern of them at three different incident wavelengths of λ = 420nm, 532nm, and 632nm, and we found out higher index approaching n ~ 1.9 tends to provide a smaller diameter of concentric circles which represents a narrower retroreflective cone with less divergence. It

allows to suggest that even ultimate, diffraction-limited angular level of retroreflected beams can be achieved in future work based on the methods developed in our work.

CHAPTER 6: CONCLUSIONS AND FUTURE DIRECTIONS

In chapter 2, we concentrated on solving the problem of large thermal noise level for uncooled FPAs operating in MWIR region. The thermal noise level can be reduced by decreasing the size of individual photodetector mesa of FPAs. This is a simple idea; however, it leads to a reduction in the photon collection and absorption efficiency of photodetectors [172]. Light concentrators integrated with FPAs which can collect light over a large area and concentrate and deliver it into photodetector mesas with small sizes is one of the promising solutions to such problem. Such structures allow to reduce the thermal current noise but preserve the level of the signal leading to higher signal-to-noise ratios and allowing to realize higher operation temperatures of the MWIR cameras. The easiest realization of this idea is known for decades, and it is represented by the commercial microlens arrays, however they have limited AoVs. More modern approaches use metalenses and/or metasurfaces [242], however all these structures have certain disadvantages and limited AoV is the most common limiting factor. We proposed Si microconical array as light concentrators considering the fact that Si is the major material for microelectronics and a well-established anisotropic wet etching of Si allows an inexpensive and fast production method for large-scale Si microcone arrays. We proposed three designs of Si microconical light concentrators operating in MWIR range (λ = 3μm ~ 5μm) with different orientation (regular and inverted) integrated with different types of photodetectors dependent on the materials and illumination directions. Using 3-D FDTD simulations, we observed a significant enhancement of power (up to 20 times) on detector

integrated with microcone compared to the same detector without microcone. We also observed a unique property of 3-D resonators formed by microcones. Namely, it is well known that the spectral position of the resonant modes in resonators with planar geometry such as a Fabry-Perot one experience a blue shift with the angle of incidence. It is also well known that the resonant peaks usually don't coincide at oblique incidence at TE and TM polarizations. We showed that 3-D microconical resonators are very different in this regard and that they can support resonant modes with omnidirectional properties in both polarizations which means that they have nearly the same spectral position in a very broad range of angles of incidence. We confirmed that such Si microconical arrays as light concentrators are capable of enhancing the photoresponse of small photodetectors and the unique properties of omnidirectional resonance can be potentially applied to multispectral imaging with a narrow ~100nm bands.

Future directions that can be investigated:

(1) Designs can be optimized for increasing the power enhancement factors using some degrees of freedom which were not studied in our work. One of the examples is represented by the size and geometry of the microcones and micropyramids.

(2) Developing fabrication techniques of Si microconical arrays with varying dimensions and different integration with FPAs such as monolithic integration with Schottky-barrier detectors.

(3) Optical measurements of the performance of fabricated Si microcone array integrated with FPAs such as PEFs and AoVs to compare with theoretical modeling.

In Chapter 3, we designed a similar microconical array as light concentrators heterogeneously integrated with FPAs operating in MWIR range by using low-index materials (n = 1.6) such as photoresist and plastics. These designs are oriented towards more conventional and inexpensive fabrication technologies such as 3-D printing in micron scales by focused laser beam on photoresist and/or injection molding of plastics. On the other hand, microcones with arbitrary angles can be produced by these methods that opens a new degree of freedom in the design of such structures. It is interesting, but perhaps not surprising, that small-angle microcones behave similar to the adiabatically tapered fibers providing very large non-resonant 3-D power enhancement factors up to ~100 times for microcones with optimized geometrical parameters. A real physical implementation of such microcone array was achieved at AFRL by laser scanning of photoresist directly on top of the front-illuminated Ni/Si Schottky barrier photodetector FPA. The testing of the fabricated structure was performed in SWIR range where a 3-fold enhancement of photocurrent due to integration with microcones was detected. Our calculations predict that the results obtained in SWIR regime should be applicable to MWIR regime.

Future research directions include:

(1) Integration with FPAs with much higher QE such as III-V semiconductors or QDIPs and testing the photoresponse such structures in the MWIR regime.

(2) Improvement of the quality of fabrication. This technology requires a high optical quality of fabricated microcones combined with the micron-scale alignment of microcones with the corresponding photodetectors. It also requires a lossless optical integration of individual microcones with the photodetectors.

In our work, we just demonstrated the concept idea, but more work is required to realize practical devices by Nanoscibe or injection molding technologies.

(3) Exploring other materials with mature manufacturing techniques to build light concentrators in different shapes instead of microcones. In mesoscale limit, many structures have light-concentrating capability and form tightly focused photonic nanojet beams that can be used for device applications.

In Chapter 4, we developed a novel label-free cellphone microscopy assisted by contact ball lens with high refractive index of n = 2.02 to achieve submicron resolution approaching diffraction limit. Conventional cellphone imaging is limited by the pixilation effects rather than by the fundamental diffraction limit. It was a long-standing idea in the imaging community that the resolution of standard cellphone camera can be greatly improved by simple microoptical solutions providing some image magnification. In our work, we show that the previous solutions were largely suboptimal because they did not reach maximal magnification values. Our approach to this problem is based on a simple geometrical optics analysis which showed that the maximal magnification values are available for ball lenses with index sufficiently close to two and placed in a contact with the object. Using the ball lens made by special LASFN35 glass with the refractive index n = 2.049 at λ = 480nm, we experimentally realized significant magnification values up to 50×. It required a fine tuning of refractive index of the ball lens in the vicinity of n ~2 which was performed based on the spectral dispersive properties of the glass material. Very large magnification values realized in our work allowed for the first time to move away from the standard resolution limitations for the cellphone imaging determined by the pixilation of the imagines and to reach the fundamental resolution limits determined by the

diffraction of light. The methodology of resolution quantification was based on a rigorous procedure based on using “perfect” drawn objects, their convolution with 2-D PSF with different widths, comparison with the experimental images, and finding the resolution as the optimal width of PSF according to the Houston resolution criterion. Using the dispersion properties of the ball lens, a resolution ~600nm was quantified, which is three times better than previously published results devoted to improving resolution of cellphone microscopy. A limited FoV less than 20μm is also observed due to the natural tradeoff between magnification and FoV. Such label-free cellphone microscopy can be a perfect replacement of bulky and expensive microscopes to build compact, portable and inexpensive imaging system for diagnostics of diseases such as melanoma *in vivo* without invasive biopsy.

Future directions that can be investigated:

(1) Developing prototype of such design of cellphone microscopy to diagnose melanoma on the skin of patients directly in the doctors’ offices without performing biopsy.

(2) Developing a microprobe attached to the ball lens to provide a raster scanning of the large areas of the patient skin and stitching the individual images to provide fast scanning over large area of the tissue to enlarge the limited FoV through single ball lens.

(3) In the cases of histological samples with coverslip layers, develop optimized designs of ball lenses providing maximal magnification effects for different gaps separating the ball lens from the tissues. Based on the results of our work,

such optimization can be achieved for indices smaller than two that in principle would allow to use ball lenses made from conventional glass materials.

(4) Besides applications in cellphone microscopy, the real imaging thorough high-index ball lenses can be used in standard microscopes (with the highest quality objectives) to study the possibility to exceed the solid-immersion lens resolution limit. Nanoplasmonic arrays with the optical near-field "hot spots" can provide ways of structured illumination of nanoscale objects which would allow to exceed the resolution limits of conventional microscopy.

In Chapter 5, we developed novel methods of making large-scale arrays of highly ordered microspheres based on their parallel suction assembly in microhole arrays. We successfully assembled hundreds of microspheres in 2-D hexagonal arrays with variable geometrical parameters. We studied the specific features of such assembly as a function of sphere diameters. It is shown that perfectly ordered single monolayers of microspheres can be assembled by this technology for sufficiently large ball lenses. However, our studies do not exclude the future use of this technology for assembling much smaller microspheres with diameters about several tenths of microns. However, developing these technologies would require solving some problems such as removing charging and particle aggregation effects, making higher quality microhole arrays, obtaining microspheres with more uniform size distribution and higher quality of the surface. The fabricated microspherical arrays were embedded into plastic coverslip by applying heating and pressure. It is demonstrated that uniform embedding can be achieved with only a little fraction of the microspheres ("tips of microspheres") slightly extending from the coverslip which is rather convenient for using such superlens arrays for biomedical imaging applications. It is

demonstrated that such slabs with embedded high-index microspheres are convenient for increasing FoV in histological studies compared to imaging through a single ball lens.

Another application of these technologies is related to developing retroreflectors with extremely narrow angular directional properties. The monolayers of microsphere arrays with high index ~1.77 - 2.02 were half coated with ~100nm thick Au layer to enhance their retroreflection properties. The retroreflective patterns of concentric circles were obtained for sapphire (n = 1.77) and LASFN9 glass (n = 1.85) for incident wavelengths of λ = 420nm, 532nm, and 632nm, and a retroreflection with narrower divergence was observed for higher refractive index with shorter incident wavelengths.

Future directions that can be investigated:

(1) Adjusting the embedding depth into the coverslip by varying the heating temperature, strength of pressure, and time for different applications.

(2) Testing these coverslips with histological biomedical samples to determine the possibility of their practical applications in hospitals' histological facilities and doctors' offices.

(3) Making next step towards further optimization of the retroreflecting structures. Our result show that higher index of refraction in the vicinity of ~1.9 is required in the case of millimeter-scale ball lenses. They also show that in the case of smaller microspheres, a smaller index of refraction would provide an optimal performance. However, behavior of retroreflectors formed by smaller microspheres can be also influence by the diffraction effects. All these properties require further studies.

REFERENCE

[1] M. I. Stockman, “Nanoplasmonics: past, present, and glimpse into future” Opt. Express 19, 22029-22106 (2011)

[2] J. B. Pendry, “Negative refraction makes a perfect lens”, Phys. Rev. Lett. 85,3966 (2000)

[3] V. G. Veselago, “Formulating Fermat's principle for light traveling in negative refraction materials”, Phys. Usp. 45, 1097–1099 (2002)

[4] A. Boardman, “Pioneers in metamaterials: John Pendry and Victor Veselag”, Journal of Optics 13, 020401 (2010)

[5] A. A. Yanik, M. Huang, O. Kamohara, A. Artar, T. W. Geisbert, J. H. Connor, and H. Altug, “An optofluidic nanoplasmonic biosensor for direct detection of live viruses from biological media”, Nano letters, 10(12), 4962–4969 (2010)

[6] K. W. Allen, N. Farahi, Y. Li, N. I. Limberopoulos, D. E. Walker Jr., A. M. Urbas, and V. N. Astratov, “Overcoming the diffraction limit of imaging nanoplasmonic arrays by microspheres and microfibers”, Opt. Express 23, 24484-24496 (2015)

[7] V. N. Astratov, N. I. Limberopoulos, and A. Urbas, “Super-resolution microscopy methods and systems enhanced by dielectric microspheres and metallic nanostructures”, US patent 9835870 (2017)

[8] V. N. Astratov, A. V. Maslov, A. Brettin, K. F. Blanchette, Y. E. Nesmelov, N. I. Limberopoulos, D. E. Walker Jr., and A. M. Urbas, “Contact microspherical nanoscopy: from fundamentals to biomedical applications”, Proc. of SPIE Vol. 10077, 100770S (2017)

[9] T. Chen, S. Li, H. Sun, “Metamaterials application in sensing”, Sensors (Basel) 12(3), 2742-2765 (2012)

[10] N. Fang and X. Zhang, “Imaging properties of a metamaterial superlens”, Appl. Phys. Lett. 82, 161 (2003)

[11] Z. Chen, A. Taflove, and V. Backman, “Photonic nanojet enhancement of backscattering of light by nanoparticles: a potential novel visible-light ultramicroscopy technique”, Opt. Express 12, 1214-1220 (2004)

[12] Y. E. Geints, A. A. Zemlyanov, and E. K. Panina, “Photonic jets from resonantly excited transparent dielectric microspheres”, J. Opt. Soc. Am. B 29, 758-762 (2012)

[13] F. Abolmaali, A. Brettin, N. I. Limberopoulos, A. M. Urbas, and V. N. Astratov, “Use of photonic jets produced by dielectric microspheres for increasing sensitivity and angle-of-view of MWIR detectors”, Proc. of SPIE, 7 pp. Phot. West, San Francisco, Jan. 28-Feb 2 (2017)

[14] K. W. Allen, J. M. Duran, G. Ariyawansa, N. I. Limberopoulos, A. M. Urbas, and V. N. Astratov, “Photonic jets for strained-layer superlattice infrared photodetector

Enhancement", IEEE Proc. of National Aerospace and Electronics Conference, Dayton, Ohio, June 25-27, p.32-33 (2014)

[15] T. C. Hutchens, A. Darafsheh, A. Fardad, A. N. Antoszyk, H. S. Ying, V. N. Astratov, and N. M. Fried, "Detachable microsphere scalpel Tips for potential use in ophthalmic surgery with the Erbium:YAG laser", J. Biomed. Opt. 19, 018003 (2014)

[16] T. C. Hutchens, A. Darafsheh, A. Fardad, A. N. Antoszyk, H. S. Ying, V. N. Astratov, and N. M. Fried, "Characterization of novel microsphere chain fiber optic tips for potential use in ophthalmic laser surgery", J. Biomed. Opt. 17, 068004 (2012)

[17] A. Darafsheh, A. Fardad, N. M. Fried, A. N. Antoszyk, H. S. Ying, and V. N. Astratov, "Contact focusing multimodal microprobes for ultraprecise laser tissue surgery", Opt. Express 19, 3440-3448 (2011)

[18] V. N. Astratov, A. Darafsheh, M. D. Kerr, K. W. Allen, N. M. Fried, A. N. Antoszyk, and H. S. Ying, "Photonic nanojets for laser surgery", SPIE Newsroom, March 12 (2010)

[19] K. W. Allen, A. F. Kosolapov, A. N. Kolyadin, A. D. Pryamikov, N. Mojaverian, N. I. Limberopoulos, and V. N. Astratov, "Photonic jets produced by microspheres integrated with hollow-core fibers for ultraprecise laser surgery", IEEE Proc. of Int. Conf. on Transparent Opt. Networks – ICTON'13, Special Section on Photonic Atoms and Molecules, Cartagena, Spain, June 23-27, 4pp., paper Tu.P.39. (2013)

[20] K. W. Allen, "Waveguide, photodetector, and imaging applications of microspherical photonics", UNC Charlotte Electronic Theses and Dissertations (2014)

[21] A. Darafsheh, T. C. Hutchens, A. Fardad, A. N. Antoszyk, H. S. Ying, N. M. Fried, and V. N. Astratov, "Contact focusing multimodal probes for potential use in ophthalmic surgery with the Erbium:YAG Laser", Proc. of SPIE 2013, paper 8567-80, 10 pp. Phot. West, San Francisco, Feb. 3-7 (2013)

[22] A. Darafsheh, A. Fardad, N. M. Fried, A. N. Antoszyk, H. S. Ying, and V. N. Astratov, "Ultra-precise focusing multimodal microprobes for contact laser tissue surgery", OSA/CLEO, Baltimore, May 1-6, AME3, 2pp. (2011)

[23] W. Wu, A. Katsnelson, O. G. Memis, and H. Mohseni, "A deep sub-wavelength process for the formation of highly uniform arrays of nanoholes and nanopillars", Nanotechnology, *18*(48), 485302 (2007)

[24] I. Mahariq, V. N Astratov, H. Kurt, "Persistence of photonic nanojet formation under the deformation of circular boundary", J. Opt. Soc. Am. B 33, 535-542 (2016)

[25] S. Yang and V. N. Astratov, "Photonic nanojet-induced modes in chains of size-disordered microspheres with an attenuation of only 0.08 dB per sphere", Appl. Phys. Lett. 92, 261111 (2008)

[26] A. M. Kapitonov and V. N. Astratov, "Observation of nanojet-induced modes with small propagation losses in chains of coupled spherical cavities", Opt. Lett. 32, 409-411 (2007)

[27] A. Darafsheh, A. Lupu S. A. Burand, K. W. Allen, T. C. Hutchens, N. M. Fried, and V. N. Astratov, "Photonic nanojet-induced modes: fundamentals and applications", in Proc. of SPIE 2012, Integrated Optics: Devices, Materials, and Technologies XVI, edited by J. E. Broquin, G. N. Conti, Proc. of SPIE, vol. 8264, 8 pp., Phot. West, Jan. 22-27, paper 82640X (2012)

[28] K. W. Allen, A. Darafsheh, and V. N. Astratov, "Photonic nanojet-induced modes: from physics to applications", IEEE Proc. of Int. Conf. on Transparent Opt. Networks – ICTON'11, Special Section on Photonic Atoms and Molecules, Stockholm, Sweden, Tu.C4.2, 4pp. (2011)

[29] A. Darafsheh, "Photonic nanojets and their applications", J. Phys. Photonics 3, 022001 (2021)

[30] A. Darafsheh, N. I. Limberopoulos, A. Lupu, and V. N. Astratov, "Filtering of radially polarized beams by microsphere-chain waveguides", Proc. of SPIE 2013, paper 8627-13, 7 pp. Phot. West, San Francisco, Feb. 3-7 (2013)

[31] A. Darafsheh and V. N. Astratov, "Radial polarization of periodically focused modes in chains of dielectric spheres", IEEE Proc. of Int. Conf. on Transparent Opt. Networks – ICTON'12, Special Section on Photonic Atoms and Molecules, Coventry, UK, July 2-5, 4pp. (2012)

[32] K. W. Allen, A. Darafsheh, and V. N. Astratov, '"Beam tapering effect' in microsphere chains: from geometrical to physical optics", in Laser Resonators, Microresonators, and Beam Control XIV, edited by A. V. Kudryashov, A. H. Paxton, V. S. Ilchenko, L. Aschke, K. Washio, Proc. of SPIE, vol. 8236, 8pp., Phot. West, Jan 22-27 (2012), paper 823622.

[33] T. C. Hutchens, A. Darafsheh, H. S. Ying, V. N. Astratov, and N. M. Fried, "Microsphere chain fiber tips for multimode filtering of Erbium:YAG laser beam during contact tissue ablation", in Optical Fibers and Sensors for Medical Diagnostics and Treatment Applications XII, edited by I. Gannot, Proc. of SPIE, vol. 8218, 8 pp., Phot. West, Jan. 22-27, paper 821803. (2012)

[34] A. Darafsheh and V. N. Astratov, "Chains of variable size spheres for focusing of multimodal beams in photonics applications", IEEE Proc. of Int. Conf. on Transparent Opt. Networks – ICTON'11, Special Section on Photonic Atoms and Molecules, Stockholm, Sweden, We.P.2, 4pp. (2011)

[35] A. Darafsheh, K. W. Allen, A. Fardad, N. M. Fried, A. N. Antoszyk, H. S. Ying, and V. N. Astratov, "Focusing capability of integrated chains of microspheres in the limit of geometrical optics", in Laser Resonators and Beam Control XIII, edited by A. V. Kudryashov, A. H. Paxton, V. S. Ilchenko, L. Aschke, Proc. of SPIE, vol. 7913, 7pp., paper 79131A. (2011)

[36] A. V. Maslov and V. N. Astratov, “Resolution and reciprocity in microspherical nanoscopy: point-spread function versus photonic nanojets”, Phys. Rev. Applied 11, 064004 (2019)

[37] J. Y. Lee, B. H. Hong, W. Y. Kim, S. K. Min, Y. Kim, M. V. Jouravlev, R. Bose, K. S. Kim, I. Hwang, L. J. Kaufman, C. W. Wong, P. Kim, and K. S. Kim, “Nearfield focusing and magnification through self-assembled nanoscale spherical lenses”, Nature, 460, 498–501 (2009)

[38] Z. Wang, W. Guo, L. Li, B. Luk'yanchuk, A. Khan, Z. Liu, Z. Chen, and M. Hong, “Optical virtual imaging at 50 nm lateral resolution with a white-light nanoscope”, Nature Communications, 2, 218 (2011)

[39] A. Darafsheh, G. F. Walsh, L. Dal Negro, and V. N. Astratov, “Optical super-resolution by high-index liquid-immersed microspheres”, Appl. Phys. Lett. 101, 141128 (2012)

[40] A. Brettin, F. Abolmaali, K. F. Blanchette, C. L. McGinnis, Y. E. Nesmelov, N. I. Limberopoulos, D. E. Walker, Jr., I. Anisimov, A. M. Urbas, L. Poffo, A. V. Maslov, and V. N. Astratov, “Enhancement of resolution in microspherical nanoscopy by coupling of fluorescent objects to plasmonic metasurfaces”, Appl. Phys. Lett. 114, 131101 (2019)

[41] A. Brettin, “Microspherical photonics for enhancing resolution of optical microscopy and sensitivity of focal plane arrays”, UNC Charlotte Electronic Theses and Dissertations (2018)

[42] A. Darafsheh, N. I. Limberopoulos, J. S. Derov, D. E. Walker, Jr., and V. N. Astratov, “Advantages of microsphere-assisted super-resolution imaging technique over solid immersion lens and confocal microscopies”, Appl. Phys. Lett. 104, 061117 (2014)

[43] F. Abolmaali, L. Poffo, A. Brettin, D. E. Walker, N. I. Limberopoulos, I. Anisimov, A. M. Urbas, A. V. Maslov, and V. N. Astratov, “Observation of the resonantly enhanced resolution of imaging of fluorescent nanospheres due to their coupling to the metallic nanoplasmonic arrays”, IEEE Proc. of National Aerospace and Electronics Conference, Dayton, Ohio, July 23-26, 4 pp. (2018)

[44] A. Brettin, C. L. McGinnis, F. Abolmaali, N. I. Limberopoulos, D. Walker, A. M. Urbas, L. Poffo, A. V. Maslov, and V. N. Astratov, “Super-resolution imaging of fluorescent nanospheres by using high-index microspheres embedded in slabs with illumination provided by plasmonic array”, IEEE Proc. of National Aerospace and Electonics Conference, Dayton, Ohio, July 23-26, 3 pp. (2018)

[45] A. Brettin, C. L. McGinnis, K. F. Blanchette, Y. E. Nesmelov, N. I. Limberopoulos, D. E. Walker Jr., A. M. Urbas, and V. N. Astratov, “Quantification of resolution in microspherical nanoscopy with biological objects”, IEEE Proc. of National Aerospace and Electonics Conference, Dayton, Ohio, June 27-30, 4 pp. (2017)

[46] J. Solomon, T. Pruthi, A. Brettin, V. Astratov, Y. Nesmelov, “Surface plasmon resonance reflects diameter of actin structures decorated with gold nanorods”, Bulletin of the American Physical Society 62, 2pp. (2017)

[47] A. Brettin, K. F. Blanchette, Y. Nesmelov, N. I. Limberopoulos, A. M. Urbas, and V. N. Astratov, "Microsphere nanoscopy for imaging of actin proteins", IEEE Proc. of National Aerospace and Electonics Conference, Dayton, Ohio, July 25-29, 3 pp. (2016)

[48] A. Brettin, F. Abolmaali, N. I. Limberopoulos, D. E. Walker Jr., A. M. Urbas, and V. N. Astratov, "Imaging of two-dimensional nanoplasmonic structures by nanoscopy with contact microlenses and various microscope objectives", IEEE Proc. of National Aerospace and Electonics Conference, Dayton, Ohio, July 25-29, 4 pp. (2016)

[49] A. Brettin, F. Abolmaali, N. I. Limberopoulos, D. E. Walker Jr., A. M. Urbas, and V. N. Astratov, "Superresolution imaging with contact microspheres: importance of numerical aperture", IEEE Proc. of Int. Conf. on Transparent Opt. Networks – ICTON'16, Special Section on Photonic Atoms and Molecules, Trento, Italy, July 10-14, 4pp., We.P.14. (2016)

[50] V. N. Astratov, A. V. Maslov, K. W. Allen, N. Farahi, Y. Li, A. Brettin, N. I. Limberopoulos, D. E. Walker Jr., A. M. Urbas, V. Liberman, and M. Rothschild, "Fundamental limits of super-resolution microscopy by dielectric microspheres and microfibers", Proc. of SPIE, Vol. 9721, 97210K, 7 pp. (2016)

[51] K. W. Allen, N. Farahi, Y. Li, N. I. Limberopoulos, D. E. Walker Jr., A. M. Urbas, V. Liberman, and V. N. Astratov, "Super-resolution by microspheres and fibers – myth or reality?", IEEE Proc. of Int. Conf. on Transparent Opt. Networks – ICTON'15, Special Section on Photonic Atoms and Molecules, Budapest, Hungary, July 5-9, 4pp., paper We.C6.1. (2015)

[52] K. W. Allen, V. Liberman, M. Rothschild, N. I. Limberopoulos, D. E. Walker Jr., A. M. Urbas, and V. N. Astratov, "Deep-UV microsphere-assisted ultramicroscopy", IEEE Proc. of Int. Conf. on Transparent Opt. Networks – ICTON'15, Special Section on Photonic Atoms and Molecules, Budapest, Hungary, July 5-9, 4pp., paper We.P.26. (2015)

[53] K. W. Allen, N. Farahi, Y. Li, N. I. Limberopoulos, D. E. Walker Jr., and V. N. Astratov, "Super-resolution imaging by arrays of high-index spheres embedded in transparent matrices", IEEE Proc. of National Aerospace and Electonics Conference, Dayton, Ohio, June 25-27, p.52-54. (2014)

[54] A. Darafsheh, Y. Li, and V. N. Astratov, "Super-resolution microscopy by dielectric microcylinders", IEEE Proc. of Int. Conf. on Transparent Opt. Networks – ICTON'13, Special Section on Photonic Atoms and Molecules, Cartagena, Spain, June 23-27, 3pp., paper Tu.P.38. (2013)

[55] A. Darafsheh, N. I. Limberopoulos, J. S. Derov, D. E. Walker Jr., and V. N. Astratov, "Comparison between Microsphere-Assisted and Confocal Microscopies", IEEE Proc. of Int. Conf. on Transparent Opt. Networks – ICTON'13, Special Section on Photonic Atoms and Molecules, Cartagena, Spain, June 23-27, 4pp., Tu.P.40. (2013)

[56] A. Darafsheh, N. I. Limberopoulos, J. S. Derov, D. E. Walker Jr., M. Durska, D. N. Krizhanovskii, D. M. Whittaker, and V. N. Astratov, "Optical microscopy with Super-resolution by liquid-immersed high-index microspheres", Proc. of SPIE 2013, paper 8594-11, 7 pp. Phot. West, San Francisco, Feb. 3-7 (2013)

[57] A. Darafsheh, M. A. Fiddy, and V. N. Astratov, "Super-resolution imaging by high-index microspheres immersed in a liquid", IEEE Proc. of Int. Conf. on Transparent Opt. Networks – ICTON'12, Special Section on Photonic Atoms and Molecules, Coventry, UK, July 2-5, 3pp. (2012)

[58] V. N. Astratov and A. Darafsheh, "Methods and systems for super-resolution optical imaging using high-index of refraction microspheres and microcylinders", US patent 10386620, 08/20/2019

[59] "Collective Phenomena in Photonic, Plasmonic and Hybrid Structures", edited by S. V. Boriskina, M. Povinelli, V. N. Astratov, A.V. Zayats, and V. A. Podolskiy, Opt. Express 19, 22024-22028 (2011)

[60] **"**Label-Free Super-Resolution Microscopy, Springer Series in Biological and Medical Physics, Biomedical Engineering", edited by V. N. Astratov, Springer, Switzerland (2019)

[61] A. V. Maslov and V. N. Astratov, "Theoretical foundations of superresolution in microspherical nanoscopy", in: Label-Free Super-Resolution Microscopy, Springer Series in Biological and Medical Physics, Biomedical Engineering, edited by V. N. Astratov (Springer, Switzerland), Chap. 16, pp. 407-441. (2019)

[62] A. V. Maslov and V. N. Astratov, "Optical Nanoscopy with Contact Mie-Particles: Resolution Analysis", Appl. Phys. Lett. 110, 261107 (2017)

[63] K. W. Allen, Y. Li, and V. N. Astratov, "Reply to "Comment on 'Super-resolution microscopy by movable thin-films with embedded microspheres: resolution analysis' [Ann. Phys. (Berlin) 527, 513 (2015)]"", Ann. Phys. (Berlin) 528, 901-904 (2016)

[64] A. V. Maslov and V. N. Astratov, "Imaging of sub-wavelength structures radiating coherently near microspheres", Appl. Phys. Lett. 108, 051104 (2016)

[65] K. W. Allen, N. Farahi, Y. Li, N. I. Limberopoulos, D.E. Walker Jr., A.M. Urbas, V. Liberman, and V. N. Astratov, "Super-resolution microscopy by movable thin-films with embedded microspheres: resolution analysis", Ann. Phys. (Berlin) 527, 513–522 (2015)

[66] V. N. Astratov, F. Abolmaali, A. Brettin, G. W. Bidney, B. Jin, N. I Limberopoulos, D. E. Walker, H. Li, A. V Maslov, "Resolution enhancement in microspherical nanoscopy by coupling of emission to plasmonics metasurfaces", 21st International Conference on Transparent Optical Networks (ICTON), pp. 1-4 (2019)

[67] V. N. Astratov, A. Brettin, F. Abolmaali, L. Poffo, and A. V. Maslov, "Plasmonics and superresolution in microspherical nanoscopy", IEEE Proc. of Int. Conf. on Transparent Opt. Networks – ICTON'18, 2nd Workshop on Label-Free Super-resolution and Sensing, Bucharest, Romania, July 1-5, 4pp., We. B6.3. (2018)

[68] V. N. Astratov, A. Brettin, F. Abolmaali, C. L. McGinnis, K. F. Blanchette, Y. E. Nesmelov, A. V. Maslov, N. I. Limberopoulos, D. E. Walker Jr., and A. M. Urbas, "Spotlight on microspherical nanoscopy: experimental quantification of super-resolution", IEEE Proc. of Int. Conf. on Transparent Opt. Networks – ICTON'17, 1st Workshop on Label-Free Super-Resolution and Sensing, Girona, Spain, July 2-6, 4pp., We. D6.1. (2017)

[69] A. V. Maslov and V. N. Astratov, "Theoretical resolution of contact microspherical nanoscopy", IEEE Proc. of Int. Conf. on Transparent Opt. Networks – ICTON'17, 1st Workshop on Label-Free Super-Resolution and Sensing, Girona, Spain, July 2-6, 4pp., We. D6.2. (2017)

[70] V. N. Astratov, F. Abolmaali, A. Brettin, K. W. Allen, A. V. Maslov, N. I. Limberopoulos, D. E. Walker Jr., and A. M. Urbas, "Label-free nanoscopy with contact microlenses: super-resolution mechanisms and limitations", IEEE Proc. of Int. Conf. on Transparent Opt. Networks – ICTON'16, Special Section on Photonic Atoms and Molecules, Trento, Italy, July 10-14, 4pp., We.A6.1. (2016)

[71] V. N. Astratov, "Arrays of superlenses for super-resolution optical imaging with wide field-of-view", US patent 20210208414A1 (2021)

[72] V. N. Astratov, K. W. Allen, N. Farahi, Y. Li, N. I. Limberopoulos, D. E. Walker Jr., A. M. Urbas, V. Liberman and M. Rothschild, "Optical nanoscopy with contact microlenses overcomes the diffraction limit", SPIE Newsroom, February 11 (2016)

[73] A. Darafsheh, "Optical super-resolution and periodical focusing effects by dielectric miscrospheres", UNC Charlotte Electronic Theses and Dissertations (2014)

[74] G. C. Righini, Y. Dumeige, P. F´eron, M. Ferrari, G. Nunzi Conti, D. Ristic and S. Soria, "Whispering gallery mode microresonators: fundamentals and applications", Riv. Nuovo Cimento 34 435–88 (2011)

[75] A. Chiasera, Y. Dumeige, P. F´eron, M. Ferrari, Y. Jestin, G. Nunzi Conti, S. Pelli, S. Soria and G. C. Righini, "Spherical whispering-gallery-mode microresonators", Laser Photon. Rev. 4 457–82 (2010)

[76] A. N. Oraevsky, "Whispering-gallery waves Quantum Electron", 32 377–400 (2002)

[77] J. Ward and O. Benson, "WGM microresonators: sensing, lasing and fundamental optics with microspheres", Laser Photon. Rev. 5 553–70 (2011)

[78] Y. Li, F. Abolmaali, K. W. Allen, N. I. Limberopoulos, A. Urbas, Y. Rakovich, A. V. Maslov, and V. N. Astratov, "Whispering gallery mode hybridization in photonics molecules", Laser & Photonics Reviews 11, 1600278 (2017)

[79] J. C. Knight, G. Cheung, F. Jacques and T. A. Birks, "Phase-matched excitation of whispering-gallery-mode resonances by a fiber taper", Opt. Lett. 22 1129–31 (1997)

[80] V. N. Astratov, "Fundamentals and applications of microsphere resonator circuits", in Photonic Microresonator Research and Applications, I. Chremmos, edited by O. Schwelb and N. Uzunoglu, Springer Series in Optical Sciences, Vol. 156, pp. 423-457, ISBN: 978-1-4419-1743-0 (2010)

[81] O. Svitelskiy, Y. Li, A. Darafsheh, M. Sumetsky, D. Carnegie, E. Rafailov, and V. N. Astratov, "Fiber coupling to $BaTiO_3$ glass microspheres in an aqueous environment", Opt. Lett. 36, 2862-2865 (2011)

[82] B. D. Jones, M. Oxborrow, V. N. Astratov, M. Hopkinson, A. Tahraoui, M. S. Skolnick, and A. M. Fox, "Splitting and lasing of whispering gallery modes in quantum dot micropillars", Opt. Express 18, 22578-22592 (2010)

[83] S. Yang and V. N. Astratov, "Spectroscopy of coherently coupled whispering-gallery modes in size-matched bispheres assembled on a substrate", Opt. Lett. 34, 2057-2059 (2009)

[84] V. N. Astratov, S. Yang, S. Lam, B. D. Jones, D. Sanvitto, D. M. Whittaker, A. M. Fox, and M. S. Skolnick, A. Tahraoui, P. W. Fry, and M. Hopkinson, "Whispering gallery resonances in semiconductor micropillars", Appl. Phys. Lett. 91, 071115 (2007)

[85] S. P. Ashili, V. N. Astratov, and E. C. H. Sykes, "The effects of inter-cavity Separation on optical coupling in dielectric bispheres", Optics Express 14, 9460-9466 (2006)

[86] A. V. Kanaev, V. N. Astratov, and W. Cai, "Optical coupling at a distance between detuned spherical cavities", Appl. Phys. Lett. 88, 111111 (2006)

[87] S. Deng, W. Cai, and V. N. Astratov, "Numerical study of light propagation via whispering gallery modes in microcylinder coupled resonator optical waveguides", Optics Express 12, 6468-6480 (2004)

[88] F. Abolmaali, Y. Li, K. W. Allen, N. I. Limberopoulos, A. M. Urbas, Y. Rakovich, A. V. Maslov, and V. N. Astratov, "Photonic molecules and sensors based on coupling between whispering gallery modes in microspheres", IEEE Proc. of National Aerospace and Electonics Conference, Dayton, Ohio, June 27-30, 4 pp. (2017)

[89] F. Abolmaali, Y. Li, K.W. Allen, N. I. Limberopoulos, A. M. Urbas, Y. Rakovich, A. V. Maslov, and V. N. Astratov, "Spectral signatures of photonic molecules with hybridized whispering gallery modes", IEEE Proc. of Int. Conf. on Transparent Opt. Networks – ICTON'17, Special Section on Photonic Atoms and Molecules, Girona, Spain, July 2-6, 4pp., We.P.28. (2016)

[90] F. Abolmaali, N. I. Limberopoulos, A. M. Urbas, and V. N. Astratov, "Resonance-based optical routing and nonreciprocity in photonic molecules with coupled whispering gallery modes", IEEE Proc. of National Aerospace and Electronics Conference, Dayton, Ohio, July 25-29, 4 pp. (2016)

[91] A. V. Maslov, M. I. Bakunov, and V. N. Astratov, "Dynamics of dielectric microparticles in optical fields: taking advantage of intrinsic particle resonances and hybrid particle-waveguide resonances", IEEE Proc. of Int. Conf. on Transparent Opt. Networks – ICTON'15, Special Section on Photonic Atoms and Molecules, Budapest, Hungary, 4pp., paper We.C6.4. July 5-9 (2015)

[92] F. Abolmaali, N. I. Limberopoulos, A. M. Urbas, and V. N. Astratov, "Observation of the influence of the gain on parity-time-symmetric properties of photonic molecules with coupled whispering gallery modes", IEEE Proc. of National Aerospace and Electonics Conference, Dayton, Ohio, June 16-19 (2015)

[93] F. Abolmaali, N. I. Limberopoulos, A. M. Urbas, A. V. Maslov, and V. N. Astratov, "Resonant routing of optical pulses in coupled-cavity ctructures", Proc. of SPIE 2017, 7 pp. Phot. West, San Francisco, Jan. 28-Feb 2 (2017)

[94] B. D. Jones, M. Oxborrow, V. N. Astratov, M. Hopkinson, A. Tahraoui, M. S. Skolnick, and A. M. Fox, "Splitting and lasing of whispering gallery modes in quantum dot micropillars", OSA/CLEO, Baltimore, May 1-6, paper QWH7, 2pp. (2011)

[95] S. Yang and V. N. Astratov, "Spectroscopy of coherently coupled whispering gallery modes in supermonodispersive bispheres", IEEE Proc. of Int. Conf. on Transparent Opt. Networks – ICTON'09, Special Section on Microresonators and Photonic Molecules: Trapping, Harnessing and Releasing Light, Island of Säo Miguel, Azores, Portugal, June 28-July 2, We. A4.5, 4pp. (2009)

[96] S. Yang and V. N. Astratov, "Spectroscopy of photonic molecular states in supermonodispersive bispheres", Proc. of SPIE, Vol. 7194, paper 719411-1, Photonics West 2009, San Jose, January 24-29, 9pp. (2009)

[97] B. D. Jones, V. N. Astratov, R. Oulton, S. Lam, D. Sanvitto, D. M. Whittaker, A. M. Fox, M. S. Skolnick, P. W. Fry and M. Hopkinson, "Whispering gallery modes in quantum dot micropillar cavities", Proc. of CLEO/QELS, CTuW7, San Jose, CA, 2pp., May 4 (2008)

[98] B. D. Jones, V. N. Astratov, R. Oulton, S. Lam, D. Sanvitto, D. M. Whittaker, A. M. Fox, P.W. Fry, M Hopkinson, and M. S. Skolnick, "Whispering gallery modes in quantum dot micropillar cavities", Proc. of ICPS-29, Tu-PC3-132, Rio de Janeiro - Brazil, World Scientific, 2pp. (2009)

[99] K. W. Allen, A. Darafsheh, F. Abolmaali, N. Mojaverian, N. I. Limberopoulos, A. Lupu, and V. N. Astratov, "Microsphere-chain waveguides: focusing and transport properties", Appl. Phys. Lett. 105, 021112 (2014)

[100] A. Darafsheh, N. Mojaverian, N. I. Limberopoulos, K. W. Allen, A. Lupu, and V. N. Astratov, "Formation of polarized beams in chains of dielectric spheres and cylinders", Opt. Lett. 38, 4208-4211 (2013)

[101] A. Darafsheh and V. N. Astratov, "Periodically focused modes in chains of dielectric spheres", Appl. Phys. Lett. 100, 061123 (2012)

[102] V. N. Astratov, J. P. Franchak, and S. P. Ashili, "Optical coupling and transport phenomena in chains of spherical dielectric microresonators with size disorder", Appl. Phys. Lett. v. 85, 5508-5510 (2004)

[103] X. Jiang, A. J. Qavi, S. H. Huang, and L. Yang, "Whispering-gallery sensors", Matter, 3(2), 371–392 (2020)

[104] N. Toropov, G. Cabello, M. P. Serrano, Rithvik R. Gutha, Matías Rafti, and Frank Vollmer, "Review of biosensing with whispering-gallery mode lasers", Light Sci Appl 10**,** 42 (2021)

[105] O. V. Svitelskiy, Y. Li, M. Sumetsky, D. Carnegie, E. Rafailov, and V. N. Astratov, "A microfluidic platform integrated with tapered optical fiber for studying resonant properties of compact high index microspheres", IEEE Proc. of Int. Conf. on Transparent Opt. Networks – ICTON'11, Special Section on Photonic Atoms and Molecules, Stockholm, Sweden, We.P.1, 4pp. (2011)

[106] K. R. Hiremath and V. N. Astratov, "Perturbations of whispering gallery modes by nanoparticles embedded in microcavities", Opt. Express 16, 5421-5426 (2008) Selected for the Virtual Journal for Biomedical Optics 3, Issue 3 (2008)

[107] V. N. Astratov and S. P. Ashili, "Percolation of light through whispering gallery modes in 3D lattices of coupled microspheres", Focus Issue on Physics and Applications of Microresonators, Opt. Express 15, 17351-17361 (2007)

[108] B. Jin, A. M. Korolev, and V. N. Astratov, "Theoretical analysis of the referencing scheme in WGM Sensors", 10.1109/ICTON51198.2020.9203009 (2020)

[109] H. Li, B. Shi, B. Jin, and V. N. Astratov, "Multiple-channel self-referencing in microfluidic chip-scale label-free whispering gallery mode biochemical sensor platform", 10.1109/ICTON51198.2020.9203353 (2020)

[110] H. Li, B.a Jin, and V. N. Astratov, "Self-referencing in microfluidic with whispering-gallery mode sensors for label-free detection of biomolecules", 10.1109/NAECON46414.2019.9057986 (2019)

[111] F. Abolmaali, Y. Li, A. Lupu, M. Tchernycheva, A. V. Maslov, N. I. Limberopoulos, A. M. Urbas, and V. N. Astratov, "Identification of whispering gallery modes in a fiber based sensor platform", IEEE Proc. of National Aerospace and Electronics Conference, Dayton, Ohio, June 27-30, 4 pp. (2017)

[112] Y. Li, F. Abolmaali, N. I. Limberopoulos, A. M. Urbas, and V. N. Astratov, "Coupling properties and sensing applications of photonic molecules", IEEE Proc. of National Aerospace and Electronics Conference, Dayton, Ohio, June 16-19 (2015)

[113] Y. Li, A. V. Maslov, and V. N. Astratov, "Spectral finger-prints of photonics molecules", IEEE Proc. of Int. Conf. on Transparent Opt. Networks – ICTON'14, Special Section on Photonic Atoms and Molecules, Graz, Austria, July 6-10, 4pp., paper Tu. B6.6. (2014)

[114] O. Svitelskiy, D. Sun, A. Darafsheh, M. Sumetsky, A. Lupu, M. Tchernycheva, and V. N. Astratov, "Characterization of high index microsphere resonators in fiber-integrated microfluidic platforms", in Laser Resonators and Beam Control XIII, edited by A. V. Kudryashov, A. H. Paxton, V.S. Ilchenko, L. Aschke, Proc. of SPIE, vol. 7913, 7pp., paper 791314 (2011)

[115] K. R. Hiremath and V. N. Astratov, "Splitting of whispering gallery modes by nanoparticles embedded in high Q microcavities", IEEE Proc. of Int. Conf. on Transparent Opt. Networks – ICTON'09, Special Section on Microresonators and Photonic Molecules: Trapping, Harnessing and Releasing Light, Island of Säo Miguel, Azores, Portugal, June 28-July 2, Tu.P.12**,** 4pp. (2009)

[116] Introduction to Focus Issue of Optics Express, "Physics and applications of microresonators", Edited by V. N. Astratov, Opt. Express 15, 17171 (2007). Selected for the Virtual Journal for Biomedical Optics 3, Issue 1 (2008)

[117] D. Grier, "A revolution in optical manipulation", Nature 424, 810–816 (2003)

[118] Y. Yang, Y. Ren, M. Chen, Y. Arita, and C. R. Guzmán, "Optical trapping with structured light: a review", Adv. Photonics, 3(3), 034001 (2021)

[119] V. N. Astratov, Y. Li, O. V. Svitelskiy, A. V. Maslov and M. I. Bakunov, D. Carnegie and E. Rafailov, "Microspherical photonics: ultra-high resonant propulsion forces", Opt. Photonics News 24, 40 (2013), special issue 12: Optics in 2013

[120] Y. Li, A. V. Maslov, N. I. Limberopoulos, A. M. Urbas, and V. N. Astratov, "Spectrally resolved resonant propulsion of dielectric microspheres", Laser & Photonics Rev. 9, 263–273 (2015)

[121] A. V. Maslov and V. N. Astratov, "Microspherical photonics: sorting resonant photonics atoms by using light", Appl. Phys. Lett. 105, 121113 (2014)

[122] A. V. Maslov, V. N. Astratov, and M. I. Bakunov, "Resonant propulsion of a microparticle by a surface wave", Phys.Rev. A 87, 053848 (2013)

[123] Y. Li, O. V. Svitelskiy, A. V. Maslov, D. Carnegie, E. Rafailov, and V. N. Astratov, "Giant resonant light forces in microspherical photonics", Light: Science and Applications (Nature Publishing Group) 2, e64 (2013)

[124] L. Poffo, F. Abolmaali, A. Brettin, B. Jin, J. Page, N. I. Limberopoulos, I. Anisimov, I. Vitebskiy, A. M. Urbas, A. V. Maslov, and V. N. Astratov, "The art of the impossible: sorting dielectric microspheres by using light", IEEE Proc. of National Aerospace and Electronics Conference, Dayton, Ohio, July 23-26, 4 pp. (2018)

[125] A. V. Maslov, M. I. Bakunov, Y. Li, and V. N. Astratov, "Resonant optical forces associated with the excitation of whispering gallery modes in microparticles", IEEE Proc. of Int. Conf. on Transparent Opt. Networks – ICTON'14, Special Section on Photonic Atoms and Molecules, Graz, Austria, July 6-10, 4pp., paper Mo. D6.1. (2014)

[126] Y. Li, A. V. Maslov, N. I. Limberopoulos, and V. N. Astratov, "Demonstration of whispering-gallery-mode resonant enhancement of optical forces", IEEE Proc. of National Aerospace and Electonics Conference, Dayton, Ohio, June 25-27, p.57-59. (2014)

[127] Y. Li, A. V. Maslov, and V. N. Astratov, “Spectral control and temporal properties of resonant optical propulsion”, Proc. of SPIE 2014, vol. 8960, paper 89600C, 7 pp. Phot. West, San Francisco, Feb. 1-6 (2014)

[128] A. V. Maslov, M. I. Bakunov, Y. Li, and V. N. Astratov, “Resonant optical forces associated with whispering gallery modes in microparticles”, Photonics Conference (IPC), 2014 IEEE, San Diego, CA, USA, Oct. 12-16, pp. 122-123. (2014)

[129] Y. Li, A. V. Maslov, A. Jofre, and V. N. Astratov, **“**Tuning the optical forces on- and off-resonance in microspherical photonics”, IEEE Proc. of Int. Conf. on Transparent Opt. Networks – ICTON’13, Special Section on Photonic Atoms and Molecules, Cartagena, Spain, June 23-27, 4pp., paper Mo. B6.4. (2013)

[130] Y. Li, A. V. Maslov, O. Svitelskiy, D. Carnegie, E. Rafailov, and V. N. Astratov, “Giant resonant light forces in microspherical photonics”, OSA/CLEO, San Jose, June 9-14, paper CW3F.6, 2pp. (2013)

[131] Y. Li, O. V. Svitelskiy, A. V. Maslov, D. Carnegie, E. Rafailov, and V. N. Astratov, “Resonant optical propelling of microspheres – a path to selection of almost identical photonics atoms”, IEEE Proc. of Int. Conf. on Transparent Opt. Networks – ICTON’12, Special Section on Photonic Atoms and Molecules, Coventry, UK, July 2-5, 4pp. (2012)

[132] Y. Li, O. Svitelskiy, D. Carnegie, E. Rafailov, and V. N. Astratov, “Evanescent light fields coupling effects and optical propelling of microspheres in water immersed fiber couplers”, in Laser Resonators, Microresonators, and Beam Control XIV, edited by A. V. Kudryashov, A. H. Paxton, V. S. Ilchenko, L. Aschke, K. Washio, Proc. of SPIE, vol. 8236, 8pp., Phot. West, Jan 22-27, paper 82361P. (2012)

[133] Y. Li, O. Svitelskiy, D. Carnegie, E. Rafailov, and V. N. Astratov, “Optical sorting of size matched microspheres based on resonant radiative pressure effects”, in Proc. of the MRS Workshop Series – Directed Self-Assembly of Materials, Sept 28 − Oct 1, Gaylord Opryland Hotel, Nashville, TN, p. 3. (2011)

[134] V. N. Astratov, “Methods and devices for optical sorting of microspheres based on their resonant optical properties”, US patent 9242248 (2016)

[135] V. N. Astratov, A. Darafsheh, M. D. Kerr, K. W. Allen, and N. M. Fried, “Focusing microprobes based on integrated chains of microspheres”, Proc. of Progress in Electromagnetics Research Symposium, Cambridge, U.S.A., July 5-8, 419-423 (2010)

[136] A. Darafsheh, O. V. Svitelskiy, and V. N. Astratov, “Light focusing microprobes for biomedical and photonics applications based on integrated microsphere arrays”, IEEE Proc. of Int. Conf. on Transparent Opt. Networks – ICTON’10, Special Section on Microresonators and Photonic Molecules: Trapping, Harnessing and Releasing Light, Munich, Germany, June 27-July 1, Tu.C4.3, 4pp. (2010)

[137] A. Darafsheh, M. D. Kerr, K. W. Allen, and V. N. Astratov, “Integrated microsphere arrays as compact focusing tool for biomedical and photonics applications”, Proc. of CLEO/QELS, San Jose, CA, JWA63, 2pp., May 16-21 (2010)

[138] A. Darafsheh, M. D. Kerr, K. W. Allen, N. M. Fried, A. N. Antoszyk, H. S. Ying, and V. N. Astratov, “Integrated microsphere arrays: light focusing and propagation effects”, in Optoelectronic Integrated Circuits XII, edited by L. A. Eldada, E. Lee, Proc. of SPIE, vol. 7605, 9pp., paper 76050R (2010)

[139] V. N. Astratov, “Fundamentals and applications of microsphere resonator circuits”, IEEE Proc. of Int. Conf. on Transparent Opt. Networks – ICTON’09, Special Section on Microresonators and Photonic Molecules: Trapping, Harnessing and Releasing Light, Island of Säo Miguel, Azores, Portugal, June 28-July 2, Tu.C4.2**,** 4pp. (2009)

[140] V. N. Astratov, “Contact focusing hollow-core fiber microprobes”, US patent 9411103 (2016)

[141] V. N. Astratov, “Focusing multimodal optical microprobe devices and methods”, US patent 8554031. Also published as EP2443494A1, US20120091369, WO2011005397A1 (2013)

[142] W. Smith, “Effect of light on selenium during the passage of an electric current”, Nature 7, 303 (1873)

[143] A. Rogalski, “Progress in focal plane array technologies”, Progress in Quantum Electronics, 36, 342–473 (2012)

[144] Committee on Developments in Detector Technologies; National Research Council, /http://www.nap.edu/catalog/12896.htmlS. (2020)

[145] H. J. Haugan, S. Elhamri, F. Szmulowicz, B. M. Ullrich, G. J. Brown and W. C. Mitchel. “Study of residual background carriers in midinfrared InAs⁄GaSb superlattices for uncooled detector operation”, Applied Physics Letters 92: 071102. (2008)

[146] X. Sun, J. B. Abshire, J. D. Beck, P. Mitra, K. Reiff, and G. Yang, “HgCdTe avalanche photodiode detectors for airborne and spaceborne lidar at infrared wavelengths”, Opt. Express 25, 16589-16602 (2017)

[147] G. A. S. Halasz, R. Tsu, L. Esaki, “A new semiconductor superlattice”, Applied Physics Letters 30, 651–653. (1977)

[148] Razeghi, A. Haddadi, A. M. Hoang, E. K. Huang, G. Chen, S. Bogdanov, S. R. Darvish, F. Callewaert, R. McClintock, “Advances in antimonide-based Type-II superlattices for infrared detection and imaging at center for quantum devices”, Infrared Physics & Technology 59, 41–52 (2013)

[149] M. Razeghi, “Focal plane arrays in type-II superlattices”, US Patent 6864552, (2005)

[150] H. Mohseni, V. I. Litvinov, M. Razeghi, “Interface-induced suppression of the Auger recombination in Type-II InAs/GaSb superlattices”, Physical Review B: Condensed Matter and Materials Physics 58, 15378–15380. (1998)

[151] B. M. Nguyen, M. Razeghi, V. Nathan, G. J. Brown, “Type-II M structure photodiodes: an alternative material design for mid-wave to long wavelength infrared regimes”, in Quantum Sensing and Nanophotonic Devices IV, San Jose, CA, USA, pp. 64790S-10. (2007)

[152] A. Dehzangi, R. McClintock, D. Wu, A. Haddadi, R. Chevallier, and M.Razeghi, “Extended short wavelength infrared heterojunction phototransistors based on type II superlattices”, Appl. Phys. Lett. 114, 191109 (2019)

[153] H. Schneider and H. C. Liu, “Quantum well infrared photodetectors”, Springer, Berlin (2007)

[154] S. Unapala, S. Bandara, J. Liu, J. Mumolo, Sir Rafol, D. Ting, A. Soibel, C. Hill, “Quantum well infrared photodetector technology and applications”, IEEE Journal of Selected Topics in Quantum Electronics 20 (6): 154. (2014)

[155] J. C. Campbell and A. Madhukar, “Quantum-dot infrared photodetectors”, in Proceedings of the IEEE, vol. 95, no. 9, pp. 1815-1827 (2007)

[156] E. Costard, A. Nedelcu, J. P. Truffer, O. Huet, L. Dua, J. A. Robo, X. Marcadet, N. Brière de l’Isle, H. Facoetti, P. Bois, “QWIP status at THALES”, Infrared Physics & Technology 52, 353–360 (2009)

[157] X. Rong, X. Q. Wang, G. Chen, X. T. Zheng, P. Wang, F. J. Xu, Z. X. Qin, N. Tang, Y. H. Chen, L. W. Sang, M. Sumiya, W. K. Gel, and B. Shen, “Mid-infrared photoconductive response in AlGaN/GaN Step quantum wells”, Scientific Reports 5(1):14386 (2015)

[158] V. Ryzhii, “The theory of quantum-dot infrared phototransistors”, Semicond. Sci. Technol., vol. 11, no. 5, pp. 759–765 (1996)

[159] J. Phillips, “Evaluation of the fundamental properties of quantum dot infrared detectors”, J. Appl. Phys., vol. 91, no. 7, pp. 4590–4594, Apr. 2002

[160] D. Pan, E. Towe, and S. Kennerly, “Normal-incidence intersubband (In, Ga) As/GaAs quantum dot infrared photodetectors”, Appl. Phys. Lett., vol. 73, pp. 1937–1939 (1998)

[161] A. Weber, O. Gauthier-Lafaye, F. H. Julien, J. Brault, M. Gendry, Y. De´sieres, and T. Benyattou, “Strong normal-incidence infrared absorption in self-organized InAs/InAlAs quantum dots grown on InP(001)”, Appl. Phys. Lett., vol. 74, pp. 413–415 (1999)

[162] L. Chu, A. Zrenner, G. Bo¨hm, and G. Abstreiter, “Normal-incident intersubband photocurrent spectroscopy on InAs/GaAs quantum dots”, Appl. Phys. Lett., vol. 75, pp. 3599–3601 (1999)

[163] J. Urayama, T. B. Norris, J. Singh, and P. Bhattacharya, “Temperature dependent carrier dynamics in InGaAs self-assembled quantum dots”, Phys. Rev. Lett., vol. 86, p. 4930 (2001)

[164] Heterogeneous Integration Roadmap 2019 Edition CHAPTER 1 OVERVIEW. https://eps.ieee.org/technology/heterogeneous-integration-roadmap.html

[165] W. Schockley and H. J. Queisser, “Detailed balance limit of efficiency of pn junction solar cells”, J. Appl. Phys. 32, 510–519 (1961)

[166] M. Garín, R. Fenollosa, R. Alcubilla, L. Shi, L. F. Marsal, and F. Meseguer, “All-silicon spherical-Mie-resonator photodiode with spectral response in the infrared region”, Nat Commun 5, 3440 (2014)

[167] F. D. Shepherd and A. C. Yang, “Silicon schottky retinas for infrared imaging”, Technical Digest of IEDM, 310–313 (1973)

[168] M. Kimata and N. Tsubouchi, “Schottky barrier photoemissive detectors”, in: A. Rogalski (Ed.), Infrared Photon Detectors, SPIE Optical Engineering Press, Bellingham, pp. 299–349 (1995)

[169] M. Kimata, N. Yutani, N. Tsubouchi, and T. Seto, “High-performance 1040 x 1040-element PtSi Schottky-barrier image sensor”, Proc. SPIE 1762, Infrared Technology XVIII, (1993)

[170] M. Kimata, M. Ueno, H. Yagi, T. Shiraishi, M. Kawai, K. Endo, Y. Kosasayama, T. Sone, T. Ozeki, and N. Tsubouchi, “PtSi schottky-barrier infrared focal plane arrays”, Opto-Electron. Rev. 6, 1–10 (1998)

[171] M. Kimata, “Silicon infrared focal plane arrays”, in: M. Henini, M. Razeghi (Eds.), Handbook of Infrared Detection Technologies, Elsevier, Oxford, pp. 353–392 (2002)

[172] R. C. Jones, “Phenomenological description of the response and detecting ability of radiation detectors”, in Proceedings of the IRE, vol. 47, no. 9, pp. 1495-1502 (1959)

[173] R.Winston, J. Minano, P. Benitez, with contributions by N. Shatz and J. C. Bortz, “Nonimaging optics”, Academic Press, OE 1 (2004)

[174] J. C. Miñano, P. Benítez, P. Zamora, M. Buljan, R. Mohedano, and A. Santamaría, “Free-form integrator array optics”, in Nonimaging Optics and Efficient Illumination Systems II, OE 2, Proc. SPIE 5942, 59420C (2005)

[175] S. L. Pyshkin, J. M. Ballato (Eds.), “Optoelectronics - advanced materials and devices”, London, United Kingdom, IntechOpen (2013)

[176] P. Pal, and K. Sato, “A comprehensive review on convex and concave corners in silicon bulk micromachining based on anisotropic wet chemical etching”, Micro and Nano Syst Lett 3, 6 (2015)

[177] D. B. Lee, “Anisotropic etching of silicon”, J. Appl. Phys. 40:4569–4575 (1969)

[178] O. Tabata, R. Asahi, H. Funabashi, K. Shimaoka, S. Sugiyama, “Anisotropic etching of silicon in TMAH solutions”, Sens Actuators A 34(1):51 –57 (1992)

[179] A. Sharma, D. Gupta, M. Chawla, R. Kumari, N. Shekhawat, A. Sharma, and S. Aggarwal, “Refractive index and dielectric measurements of B^+ implanted PET I the mid-infrared region”, AIP Conference Proceedings 2093, 020014 (2019)

[180] D. M. Bryce, “Plastic injection molding: manufacturing process fundamentals”, Society of Manufacturing Engineers (1996)

[181] E. Abbe, “Beiträge zur theorie des mikroskops und der mikroskopischen wahrnehmung”, Archiv für Mikroskopische Anatomie, 9(1), 413-418 (1873)

[182] Lord Rayleigh, “Investigations in optics, with special reference to the spectroscope”, Philosophical Magazine, 8(49), 261-274 (1879)

[183] C. M. Sparrow, “On spectroscopic resolving power”, Astrophysical Journal, 44(2), 76-86 (1916)

[184] W. V. Houston, “A compound interferometer for fine structure work”, Physical Review, 29(3), 478-484 (1927)

[185] C. J. R. Sheppard, “Resolution and super-resolution”, Microsc Res Tech. 80: 590– 598 (2017)

[186] A. Lipson, S. G. Lipson, and H. Lipson, “Optical Physics, 4th Edition”, Cambridge University Press, Cambridge, UK (2010)

[187] H. Helmholtz, “On the Limits of the Optical Capacity of the Microscope”, The Monthly microscopical journal, 16(1), 15-39 (1876)

[188] A. J. den Dekker and A. van den Bos, “Resolution: a survey”, J. Opt. Soc. Am. A 14, 547-557 (1997)

[189] https://www.thorlabs.com/newgrouppage9.cfm?objectgroup_id=5824

[190] J.M. Laskar, P. S. Kumar, S. Herminghaus, K. E. Daniels, and M. Schröter, “High refractive index immersion liquid for superresolution 3D imaging using sapphire-based aplanatic numerical aperture increasing lens optics”, Appl. Opt. 55, 3165-3169 (2016)

[191] X. Hao, C. Kuang, Z. Gu, Y. Wang, S. Li, Y. Ku, Y. Li, J. Ge, and X. Liu, “From microscopy to nanoscopy *via* visible light”, Light: Science and Applications, 2, e108 (2013)

[192] E. A. Ash, and G. Nicholls, “Super-resolution aperture scanning microscope”, Nature, 237, 510–512 (1972)

[193] I. I. Smolyaninov, J. Elliott, A. Zayats, C. C. Davis, “Far-field optical microscopy with a nanometer-scale resolution based on the in-plane image magnification by surface plasmon polaritons”, Phys. Rev. Lett. 94, 057401 (2005)

[194] Z. Liu, S. Durant, H. Lee, Y. Pikus, N. Fang, Y. Xiong, C. Sun, and X. Zhang, "Far-field optical superlens", Nano Lett. 7, 403-407 (2007)

[195] Z. Jacob, L. V. Alekseyev, and E. Narimanov, "Optical hyperlens: far-field imaging beyond the diffraction limit", Opt. Express 14**,** 8247–8256 (2006)

[196] A. Salandrino and N. Engheta, "Far-field subdiffraction optical microscopy using metamaterial crystals: theory and simulations", Phys. Rev. B 74, 075103 (2006)

[197] G. Lerosey, J. de Rosny, A. Tourin, and M. Fink, "Focusing beyond the diffraction limit with far-field time reversal", Science 315, 1120-1122 (2007)

[198] F. Wei, D. Lu, H. Shen, J. L. Ponsetto, E. Huang, and Z. Liu, "Wide field superresolution surface imaging through plasmonic structured illumination microscopy", Nano Letters 14, 4634-4639 (2014)

[199] J. Haug, M. Malei, J. D. Shrout, E. Narimanov, P. W. Bohn, and A. J. Hoffman, "Confined hyperbolic metasurface modes for structured illumination microscopy", Opt.Express 29, 42331-42342 (2021)

[200] H. Yang, N. Moullan, J. Auwerx, and M. A. M. Gijs, "Super-Resolution Biological Microscopy Using Virtual Imaging by a Microsphere Nanoscope", Small, 10(9), 1712-1718 (2014)

[201] L. Li, W. Guo, Y. Yan, S. Lee, and T. Wang, "Label-free super-resolution imaging of adenoviruses by submerged microsphere optical nanoscopy", Light: Science and Applications, 2, e104 (2013)

[202] W. Goodman, "Introduction to Fourier Optics", 2ndEd., (The McGraw-Hill Companies, New York (1996)

[203] H. Yang, R. Trouillon, G. Huszka, and M. A. M. Gijs, "Super-resolution imaging of a dielectric microsphere is governed by the waist of its photonic nanojet", Nano Lett.16, 4862 (2016)

[204] Y. Yan, L. Li, C. Feng, W. Guo, S. Lee, and M. Hong, "Microsphere-coupled scanning laser confocal nanoscope for sub-diffraction-limited imaging at 25 nm lateral resolution in the visible spectrum", ACS Nano, 8, 2, 1809–1816 (2014)

[205] F. Bezryadina, L. Liu, H. Yu, Y. Wen, P. Yu, Z. Liu, Y. Wang, and W. J. Li, "Scanning superlens microscopy for non-invasive large field-of-view visible light nanoscale imaging", Nat. Commun. 7, 13748 (2016)

[206] A. Bezryadina, J. Li, J. Zhao, A. Kothambawala, J. Ponsetto, E. Huang, J. Wang, and Z. Liu, "Localized plasmonic structured illumination microscopy with an optically trapped microlens", Nanoscale 9, 14907 (2017)

[207] H. Nishiyama, J. Nishii, M. Mizoshiri, Y. Hirata, "Microlens arrays of high-refractive index glass fabricated by femtosecond laser lithography", Appl. Surf. Sci. 255 9750 –9753. (2009)

[208] S. Surdo, A. Diaspro, M. Duocastella, “Microlens fabrication by replica molding of frozen laser-printed droplets”, Appl. Surf. Sci. 418 554 –558 (2017)

[209] O. A. Castañeda-Uribe, H. A. Méndez-Pinzón, and J. C. Salcedo-Reyes, “Controlling the quality of SiO_2 colloidal crystals by temperature ramping on the vertical convective self-assembly method,” Opt. Mater. Express 11, 2686-2699 (2021)

[210] C. A. Fustin, G. Glasser, H. W. Spiess, and Ulrich Jonas, “Site-Selective Growth of Colloidal Crystals with Photonic Properties on Chemically Patterned Surfaces”, Adv. Mater. 15, 1025 (2003)

[211] S. Grego, T. W. Jarvis, B. R. Stoner, and J. S. Lewis, “Template-directed assembly on an ordered microsphere array”, Langmuir 21, 4971-4975 (2005)

[212] T. Zhang, P. Lia, H. Yua, F. Wang, X. Wang, T. Yang, W. Yang, W. J. Li, Y. Wang, L. Liu, “Fabrication of flexible microlens arrays for parallel super-resolution imaging”, Applied Surface Science 504, 144375 (2020)

[213] H. Ni, L. Ge, X. Liu, Y. Zhou, J. Chang, H. Ali, C. Pan, T. Wang, and M. Wang, “Large area highly ordered monolayer composite microsphere arrays – fabrication and tunable surface plasmon linewidth”, RSC Adv., 8, 39735 (2018)

[214] T. Ohzono, S. I. Matsushita and M. Shimomura, “Coupling of wrinkle patterns to microsphere-array lithographic patterns”, Soft Matter, 1 , 227–230 (2005)

[215] J. M. Tam, I. Biran and D. R. Walt, “An imaging fiber-based optical tweezer array for microparticle array assembly”, Appl. Phys. Lett. 84, 4289 (2004)

[216] L. Janik, M. Novak, A. Dobesch and L. Hudcova, “Retroreflective optical communication”, 2017 Conference on Microwave Techniques (COMITE), pp. 1-4 (2017)

[217] J. Lloyd, “A brief history of retroreflective sign face sheet materials” (2008)

[218] L. Autschbach, E. Brinksmeier, H. E. Gubela, T. Ahbe, “Manufacturing of three dimensional micro-optic functional surfaces”, HTM 1:33–9. (2005)

[219] J. Park, and J. Y. Park. “A bulk-micromachined corner cube retroreflector with piezoelectric micro-cantilevers”, Micro and Nano Systems Letters 1: 1-6. (2013)

[220] J. Huignard, “CHAPTER 1 Overview of Phase Conjugation”.

[221] B. Jin, G. W. Bidney, A. Brettin, N. I. Limberopoulos, J. M. Duran, G. Ariyawansa, I. Anisimov, A. M. Urbas, S. D. Gunapala, H. Li, and V. N. Astratov, “Microconical silicon mid-iR concentrators: spectral, angular and polarization response”, Opt. Express 28, 27615- 27627 (2020)

[222] B. Jin, A. Brettin, G. W. Bidney, N. I. Limberopoulos, J. M. Duran, G. Ariyawansa, I. Anisimov, A. M. Urbas, K. W. Allen, S. D. Gunapala, and V. N. Astratov, “Light-harvesting microconical arrays for enhancing infrared imaging devices: proposal and demonstration”, Appl. Phys. Lett. 119, 051104 (2021)

[223] F. Abolmaali, A. Brettin, A. Green, N. I. Limberopoulos, A. M. Urbas, and V. N. Astratov, "Photonic jets for highly efficient mid-IR focal plane arrays with large angle-of-view", Opt. Express 25, 31174-31175 (2017)

[224] K. W. Allen, F. Abolmaali, J. M. Duran, G. Ariyawansa, N. I. Limberopoulos, A. M. Urbas, and V. N. Astratov, "increasing sensitivity and angle-of-view of mid-wave infrared detectors by integration with dielectric microspheres", Appl. Phys. Lett. 108, 241108 (2016)

[225] F. Abolmaali, "Focusing, imaging and resonance properties of microphotonics structures and devices", UNC Charlotte Electronic Theses and Dissertations (2018)

[226] B. Jin, G. W. Bidney, and V. N. Astratov, "Design of silicon microcone concentrators for heterogeneous integration with MWIR FPAs", 10.1109/ICTON51198.2020.9203159 (2020)

[227] B. Jin, G. W. Bidney, and V. N. Astratov, "High-index microcones for focusing and concentrating light in MWIR focal plane arrays", 10.1109/NAECON46414.2019.9057919 (2019)

[228] B. Jin, A. Brettin, G. W. Bidney, J. M. Duran, G. Ariyawansa, I. Anisimov, N. I. Limberopoulos, A. M. Urbas, K. W. Allen, S. D. Gunapala, and V. N. Astratov, "Light-concentrating microcone array for improving performance of infrared imaging devices", NAECON 2021- IEEE National Aerospace and Electronics Conference, pp. 119-122 (2021)

[229] B. Jin, A. Brettin, G. W. Bidney, N. I. Limberopoulos, J. M. Duran, G. Ariyawansa, I. Anisimov, A. M. Urbas, K. W. Allen, S. D. Gunapala, and V. N. Astratov, "Light-harvesting microconical arrays integrated with photodetector FPAs for enhancing infrared imaging devices", Proc. SPIE 12004, Integrated Optics: Devices, Materials, and Technologies XXVI, 120040X (2022)

[230] A. Brettin, F. Abolmaali, N. I. Limberopoulos, A. Green, I. Anisimov, A. M. Urbas, and V. N. Astratov, "Towards fabrication of mid-IR FPAs with enhanced sensitivity and reduced dark current by using integration with microspherical arrays", IEEE Proc. of National Aerospace and Electronics Conference, Dayton, Ohio, July 23-26, 3 pp. (2018)

[231] F. Abolmaali, N. I. Limberopoulos, A. M. Urbas, and V. N. Astratov, "Design and optimization of focal plane arrays Integrated with dielectric microspheres", IEEE Proc. of National Aerospace and Electonics Conference, Dayton, Ohio, July 25-29, 4 pp. (2016)

[232] A. Brettin, N. I. Limberopoulos, I. Anisimov, A. M. Urbas, and V. N. Astratov, "Microconical arrays as novel light-concentrating structures for enhancing sensitivity, angle-of-view, and reducing Dark Current of mid-IR FPAs", IEEE Proc. of National Aerospace and Electonics Conference, Dayton, Ohio, July 23-26, pp. 496-498. (2018)

[233] V. N. Astratov, A. Brettin, N. I. Limberopoulos, and A. Urbas, "Photodetector focal plane array systems and methods based on microcomponents with arbitrary shapes", US patent 10585238 (2020)

[234] V. N. Astratov, K. W. Allen, N. I. Limberopoulos, A. Urbas, and J. M. Duran, "Photodetector focal plane array systems and methods", US patent 9362324 (2016)

[235] B. Jin, G. W. Bidney, I. Anisimov, N. I. Limberopoulos, A. V. Maslov, and V. N. Astratov, "High-resolution label-free cellphone microscopy using contact ball lenses", NAECON 2021 - IEEE National Aerospace and Electronics Conference, pp. 356-358 (2021)

[236] B. Jin, G. W. Bidney, I. Anisimov, N. I. Limberopoulos, A. V. Maslov, and V. N. Astratov, "Label-free cellphone microscopy with submicron resolution through high-index contact ball lens for *in Vivo* melanoma diagnostics and other applications", Proc. SPIE 11972, Label-free Imaging and Sensing (LBIS) 2022, 119720F (2022)

[237] G. W. Bidney, Aarron Brettin, Boya Jin, and Vasily N. Astratov, "Improving cellphone microscopy imaging with contact ball lenses", 10.1109/NAECON46414.2019.9058104 (2019)

[238] Q. Wei, H. Qi, W. Luo, D. Tseng, S. J. Ki, Z. Wan, Z. Gorocs, L. A. Bentolila, T. Wu, R. Sun, and A. Ozcan, "Fluorescent imaging of single nanoparticles and viruses on a smart phone", ACS Nano 7, 10, 9147–9155 (2013)

[239] P. B. Catrysse and T. Skauli, "Pixel scaling in infrared focal plane arrays", Appl. Opt. 52(7), C72–C77 (2013)

[240] C. L. Tan and H. Mohseni, "Emerging technologies for high performance infrared detectors", Nanophotonics 7 (1), 169-197 (2018)

[241] A. Soibel, S. A. Keo, A. Fisher, C. J. Hill, E. Luong, D. Z. Ting, S. D. Gunapala, D. Lubyshev, Y. Qiu, J. M. Fastenau, and A. W. K. Liu, "High operating temperature nBn detector with monolithically integrated microlens", Appl. Phys. Lett. 112, 041105 (2018)

[242] S. Zhang, A. Soibel, S. A. Keo, D. Wilson, S. B. Rafol, D. Z. Ting, A. She, S. D. Gunapala, and F. Capasso, "Solid-immersion metalenses for infrared focal plane arrays", Appl. Phys. Lett. 113, 111104 (2018)

[243] A. Kazemi, Q. Shu, V. Dahiya, Z. Taghipour, P. Paradis, C. Ball, T. J. Ronningen, S. Zollner, S. M. Young, J. Budhu, K. A. Grossklaus, T. E. Vandervelde, A. Grbic, and S. Krishna, "Subwavelength antimonide infrared detector coupled with dielectric resonator antenna", Proc. SPIE 11002, Infrared Technology and Applications XLV, 1100221 (7 May 2019)

[244] Y. Chen, W. A. Britton, and Luca Dal Negro, "Spatially-modulated axilenses for infrared multi-band imaging and spectroscopy", https://arxiv.org/abs/2001.03127 (2001)

[245] F. Li, J. Deng, J. Zhou, Z. Chu, Y. Yu, X. Dai, H. Guo, L. Chen, S. Guo, M. Lan, and X. Chen, "HgCdTe mid-Infrared photo response enhanced by monolithically integrated metalenses", Sci. Reports 10, 6372 (2020)

[246] B. Desiatov, I. Goykhman, N. Mazurski, J. Shappir, J. B. Khurgin, and U. Levy, "Plasmonic enhanced silicon pyramids for internal photoemission Schottky detectors in the near-infrared regime", Optica 2, 335-339 (2015)

[247] H. J. Syu, H. C. Chuang, M. J. Lin, C. C. Cheng, P. J. Huang, and C. F. Lin, "Ultra-broadband photoresponse of localized surface plasmon resonance from Si-based pyramid structures", Photonics Research 7, 1119-1126 (2019)

[248] I. V. Minin, O. V. Minin, and Y. E. Geints, "Localized EM and photonic jets from non-spherical and non-symmetrical dielectric mesoscale objects: Brief review", Ann. Phys. (Berlin) 527, No. 7–8, 491–497 (2015)

[249] A. Giugni, B. Torre, A. Toma, M. Francardi, M. Malerba, A. Alabastri, R. Proietti Zaccaria, M. I. Stockman, and E. Di Fabrizio, "Hot-electron nanoscopy using adiabatic compression of surface plasmons", Nature Nanotechnology 8, 845-852 (2013)

[250] V. N. Astratov, A. Brettin, N.I. Limberopoulos, and A. Urbas, "Photodetector focal plane array systems and methods based on microcomponents with arbitrary shapes", US patent 10585238 (2020)

[251] I. Zubel and I. Barycka, "Silicon anisotropic etching in alkaline solutions I. The geometric description of figures developed under etching Si (100) in various solutions", Sens. Actuators A Phys. 70, 250–259 (1998)

[252] H. Lu, H. Zhang, M. Jin, T. He, G. Zhou, and L. Shui, "Two-layer microstructures fabricated by one-step anisotropic wet etching of Si in KOH Solution", Micromachines 7, 19 (2016)

[253] G. W. Bidney, B. Jin, L. Deguzman, T. C. Hutchens, J. M. Duran, G. Ariyawansa, I. Anisimov, N. I. Limberopoulos, A. M. Urbas, K. W. Allen, S. D. Gunapala, and V. N. Astratov, "Anisotropic wet etching of Si as a fabrication tool enabling 3-D microphotonics structures and device", NAECON 2021 - IEEE National Aerospace and Electronics Conference, pp. 146-149 (2021)

[254] G. W. Bidney, B. Jin, L. Deguzman, J. M. Duran, G. Ariyawansa, I. Anisimov, N. I. Limberopoulos, A. M. Urbas, K. W. Allen, S. D. Gunapala, and V. N. Astratov, "Ni-Silicide schottky barrier micropyramidal photodetector array", NAECON 2021 - IEEE National Aerospace and Electronics Conference, pp. 116-118 (2021)

[255] G. W. Bidney, B. Jin, L. Deguzman, T. C. Hutchens, J. M. Duran, G. Ariyawansa, I. Anisimov, N. I. Limberopoulos, A. M. Urbas, K. W. Allen, S. D. Gunapala, and V. N. Astratov, "Fabrication of 3-D light concentrating microphotonic structures by anisotropic wet etching of silicon", Proc. SPIE 12012, Advanced Fabrication Technologies for Micro/Nano Optics and Photonics XV, 120120B (2022)

[256] X. Chen, R. S.Patel, J. A.Weibel, S. V.Garimella, “Coalescence-induced jumping of multiple condensate droplets on hierarchical superhydrophobic surfaces”, Scientific Reports 6, 18649 (2016).

[257] J. Duran, “Silicon-based infrared photodetectors for low-cost imaging applications”, Ph.D. thesis (University of Dayton, 2019)

[258] J. Duran and A. Sarangan, “Schottky-barrier photodiode internal quantum efficiency dependence on nickel silicide film thickness”, IEEE Photonics Journal 11,6800215 (2019)

[259] S. Rim, P. B. Catrysse, R. Dinyari, K. Huang, and P. Peumans, “The optical advantages of curved focal plane arrays”, Opt. Express 16, 4965-4971 (2008)

[260] Y. Zhai, Q. Han, J. Niu, J. Liu, and B. Yang, “Microfabrication of bioinspired curved artificial compound eyes: a review”, Microsystem Technologies 27:3241–3262 (2021)

[261] A. Andryieuski and A. V. Lavrinenko, “Nanocouplers for Infrared and Visible Light”, Advances in OptoElectronics, 839747 (2012)

[262] Y. Fu, T. Ye, W. Tang, and T. Chu, “Efficient adiabatic silicon-on-insulator waveguide taper”, Photon. Res. 2, A41-A44 (2014)

[263] A. Brettin, N. I. Limberopoulos, I. Anisimov, A. M. Urbas, and V. N. Astratov, “Microconical arrays as novel light-concentrating structures for enhancing sensitivity, angle-of-view, and reducing dark current of mid-IR FPAs”, IEEE Proc. of National Aerospace and Electronics Conference, Dayton, Ohio, July 23-26, pp. 496-498. (2018)

[264] D. B. Fullager, G. D. Boreman, and T. Hofmann, “Infrared dielectric response of nanoscribe IP-dip and IP-L monomers after polymerization from 250 cm^{-1} to 6000 cm^{-1}”, Opt. Mater. Express 7(3), 888-894 (2017)

[265] J. Li, J. Garfinkel, X. Zhang, D. Wu, Y. Zhang, K. de Haan, H. Wang, T. Liu, B. Bai, Y. Rivenson, G. Rubinstein, P. O. Scumpia, and A. Ozcan, “Biopsy-free in vivo virtual histology of skin using deep learning”, Light: Science & Applications 10, 233 (2021)

[266] D. Lange, C. W. Storment, C. A. Conley and G. T. A. Kovacs, “A microfluidic shadow imaging system for the study of the nematode Caenorhabditis elegans in space”, Sensors and Actuators B-chemical 107, 904-914 (2005)

[267] X. Heng, D. Erickson, L. R. Baugh, Z. Yaqoob, P. W. Sternberg, D. Psaltis, and C. Yang, “Optofluidic microscopy—a method for implementing a high resolution optical microscope on a chip”, Lab Chip 6, 1274–1276 (2006)

[268] J. Garcia-Sucerquia, W. Xu, S. K. Jericho, P. Klages, M. H. Jericho, and H. Jürgen Kreuzer, “Digital in-line holographic microscopy”, Appl. Opt. 45, 836-850 (2006)

[269] D. Tseng, O. Mudanyali, C. Oztoprak, S. O. Isikman, I. Sencan, O. Yaglidere, and A. Ozcan, "Lensfree microscopy on a cellphone", Lab on a chip 10, 1787–1792 (2010)

[270] D. N. Breslauer, R. N. Maamari, N. A. Switz, W. A. Lam, and D. A. Fletcher, "Mobile phone based clinical microscopy for global health applications", PloS ONE 4, e6320 (2009)

[271] H. Zhu, O. Yaglidere, T. Su, D. Tseng, and A. Ozcan, "Cost-effective and compact wide-field fluorescent imaging on a cell-phone", Lab Chip 11, 315-322 (2011)

[272] J. Smith, K. Chu, A. R. Espenson, M. Rahimzadeh, A. Gryshuk, M. Molinaro, D. M. Dwyre, S. Lane, D. Matthews, and S. Wachsmann-Hogiu, "Cell-phone-based platform for biomedical device development and education applications", PLoS ONE 6, e17150 (2011)

[273] N. A. Switz., M. V. D'Ambrosio, and D. A. Fletcher, "Low-cost mobile phone microscopy with a reversed mobile phone camera lens", PLoS ONE 9, e95330 (2014)

[274] E. McLeod, Q. Wei, and A. Ozcan, "Democratization of nanoscale imaging and sensing tools using photonics", Anal. Chem. 87, 6434-6445 (2015)

[275] https://kayakuam.com/wp-content/uploads/2019/09/PMMA_Data_Sheet.pdf MicroChem PMMA WP (2019)

[276] B.Acs, F. S. Ahmed, S. Gupta, P. F. Wong, R. D. Gartrell, J. S. Pradhan, E. M. Rizk, B. G. Rothberg, Y. M. Senger, and D. L. Rimm, "An open source automated tumor infiltrating lymphocyte algorithm for prognosis in melanoma", Nat Commun. 10, 5440 (2019)

[277] M. Antohe, R. I. Nedelcu, L. Nichita, C. G. Popp, M. Cioplea, A. Brinzea, A. Hodorogea, A. Calinescu, M. Balaban, D. A. Ion, C. Diaconu, C. Bleotu, D. Pirici, S. A. Zurac, and G. Turcu, "Tumor infiltrating lymphocytes: The regulator of melanoma evolution", Oncol Lett, 17(5), 4155-4161 (2019)

[278] F. Azimi, R. A. Scolyer, P. Rumcheva, M. Moncrieff, R. Murali, S. W. McCarthy, R. P. Saw, and J. F. Thompson, "Tumor-infiltrating lymphocyte grade is an independent predictor of sentinel lymph node status and survival in patients with cutaneous melanoma", J Clin Oncol, 30(21), 2678-83 (2012)

[279] M. C. Mihm Jr, and J. J. Mule, "Reflections on the histopathology of tumor-infiltrating lymphocytes in melanoma and the host immune response", Cancer Immunol Res, 3(8), 827-35 (2015)

[280] F. Maibach, H. Sadozai, S. M. S. Jafari, R. E. Hunger, and M. Schenk, "Tumor-infiltrating lymphocytes and their prognostic value in cutaneous melanoma", Front Immunol, 11, 2105 (2020)

[281] W. H. Clark Jr, D. E. Elder, D. Guerry 4th, L. E. Braitman, B. J. Trock, D. Schultz, M. Synnestvedt, and A. C. Halpern, "Model predicting survival in stage I melanoma based on tumor progression", J Natl Cancer Inst, 81(24), 1893-904 (1989)

APPENDIX A: PUBLICATIONS SO FAR

Journal papers:

[1] **Boya Jin**, Grant W. Bidney, and Vasily N. Astratov, "Microconical silicon mid-IR concentrators: spectral, angular and polarization response", Optics Express 28(19), 27615-27627 (2020)

[2] **Boya Jin**, Aaron Brettin, Grant W Bidney, Nicholaos I Limberopoulos, Joshua M Duran, Gamini Ariyawansa, Igor Anisimov, Augustine M Urbas, Kenneth W Allen, Sarath D Gunapala, Vasily N Astratov, "Light-harvesting microconical arrays for enhancing infrared imaging devices: Proposal and demonstration", Appl. Phys. Lett. 119, 051104 (2021)

[3] **Boya Jin**, Grant W. Bidney, Amstrong Jean, Igor Anisimov, Nicholaos I.Limberopoulos, Kenneth W. Allen, Alexey V. Maslov, and Vasily N. Astratov, "Cellphone Microscopy with Diffraction-Limited Resolution: Towards *in-vivo* and *in-situ* Biomedical Diagnostic Imaging", submitted to Laser & Photonics Reviews

[4] **Boya Jin**, Grant W. Bidney, Amstrong Jean, Igor Anisimov, Nicholaos I. Limberopoulos, Kenneth W. Allen, Alexey V. Maslov, and Vasily N. Astratov, "Label-free cellphone microscopy assisted by high-index contact ball lens for *in Vivo* melanoma diagnostics and precise method of resolution quantification", submitted to Optics Letters

Conference papers:

[1] **Boya Jin**, Grant W. Bidney, and Vasily N. Astratov, "Design of Silicon Microcone concentrators for Heterogeneous Integration with MWIR FPAs", 10.1109/ICTON51198.2020.9203159

[2] **Boya Jin**, Alex M. Korolev, and Vasily N. Astratov, "Theoretical Analysis of the Referencing Scheme in WGM Sensors", 10.1109/ICTON51198.2020.9203009

[3] **Boya Jin**, Grant W. Bidney, and Vasily N. Astratov, "High-index Microcones for focusing and concentrating light in MWIR focal plane arrays", 10.1109/NAECON46414.2019.9057919

[4] **Boya Jin**, Aaron Brettin, Grant W. Bidney, Joshua M. Duran, Gamini Ariyawansa, Igor Anisimov, Nicholaos I. Limberopoulos, Augustine M. Urbas, Kenneth W. Allen, Sarath D. Gunapala, and Vasily N. Astratov, "Light-concentrating microcone array for improving performance of infrared imaging devices", NAECON 2021- IEEE National Aerospace and Electronics Conference, pp. 119-122 (2021)

[5] **Boya Jin**, Grant W. Bidney, Igor Anisimov, Nicholaos I. Limberopoulos, A. V. Maslov, andV. N. Astratov, "High-resolution label-free cellphone microscopy using contact ball lenses", NAECON 2021 - IEEE National Aerospace and Electronics Conference, pp. 356-358 (2021)

[6] **Boya Jin**, Grant W. Bidney, Igor Anisimov, Nicholaos I. Limberopoulos, A. V. Maslov, and V. N. Astratov, "Label-free cellphone microsopy with submicron resolution through high-index contact ball lens for *in Vivo* melanoma diagnostics and other applications", Proc. SPIE 11972, Label-free Biomedical Imaging and Sensing (LBIS) 2022, 119720F (2 March 2022)

[7] **Boya Jin**, Aaron Brettin, Grant W. Bidney, Nicholaos I. Limberopoulos, Joshua M. Duran, Gamini Ariyawansa, Igor Anisimov, Augustine M. Urbas, Kenneth W. Allen, Sarath D. Gunapala, and Vasily N. Astratov, "Light-harvesting microconical arrays integrated with photodetector FPAs for enhancing infrared imaging devices", Proc. SPIE 12004, Integrated Optics: Devices, Materials, and Technologies XXVI, 120040X (5 March 2022)

[8] Hanyang Li, **Boya Jin**, and Vasily N. Astratov, "Self-referencing in microfluidic with whispering-gallery mode sensors for label-free detection of biomolecules", 10.1109/NAECON46414.2019.9057986

[9] G. W. Bidney, **Boya Jin**, L. Deguzman, T. C. Hutchens, J. M. Duran, G. Ariyawansa, I. Anisimov, N. I. Limberopoulos, A. M. Urbas, K. W. Allen, S. D. Gunapala, and V. N. Astratov, "Anisotropic Wet Etching of Si as a Fabrication Tool Enabling 3-D Microphotonics Structures and Device", NAECON 2021 - IEEE National Aerospace and Electronics Conference, pp. 146-149 (2021)

[10] G. W. Bidney, **Boya Jin**, L. Deguzman, J. M. Duran, G. Ariyawansa, I. Anisimov, N. I. Limberopoulos, A. M. Urbas, K. W. Allen, S.D. Gunapala, and V. N. Astratov, "Ni-Silicide Schottky Barrier Micropyramidal Photodetector Array", NAECON 2021 - IEEE National Aerospace and Electronics Conference, pp. 116-118 (2021)

[11] G. W. Bidney, **Boya Jin**, Lou Deguzman, Thomas C. Hutchens, Joshua M. Duran, Gamini Ariyawansa, Igor Anisimov, Nicholaos I. Limberopoulos, Augustine M. Urbas, Kenneth W. Allen, Sarath D. Gunapala, and Vasily N. Astratov, "Fabrication of 3-D Light Concentrating Microphotonic Structures by Anisotropic Wet Etching of Silicon", Proc. SPIE 12012, Advanced Fabrication Technologies for Micro/Nano Optics and Photonics XV, 120120B (5 March 2022)

[11] Hanyang Li, Bojian Shi, **Boya Jin**, and Vasily N. Astratov, "Multiple-Channel Self-Referencing in Microfluidic Chip-Scale Label-free Whispering Gallery Mode Biochemical Sensor Platform ", 10.1109/ICTON51198.2020.9203353

[12] G. W. Bidney, Aarron Brettin, **Boya Jin**, and Vasily N. Astratov, "Improving Cellphone Microscopy Imaging with Contact Ball Lenses", 10.1109/NAECON46414.2019.9058104

[13] Luiz Poffo, Farzaneh Abolmaali, Aaron Brettin, **Boya Jin**, James Page, Nicholaos I Limberopoulos, Igor Anisimov, Ilya Vitebskiy, Augustine M Urbas, Alexey V Maslov, and Vasily N Astratov, "The Art of the Impossible: Sorting Dielectric Microspheres by using Light," IEEE National Aerospace and Electronics Conference, pp. 499-502 (2018)

[14] Vasily N Astratov, Farzaneh Abolmaali, Aaron Brettin, Grant W. Bidney, **Boya Jin**, Nicholaos I Limberopoulos, Dennis E Walker, Hanyang Li, Alexey V Maslov, "Resolution Enhancement in Microspherical Nanoscopy by Coupling of Emission to Plasmonics Metasurfaces," 2019 21st International Conference on Transparent Optical Networks (ICTON), pp. 1-4 (2019)